

Multiscale structure and mechanics of collagen

Citation for published version (APA):

Amuasi, H. E. (2012). *Multiscale structure and mechanics of collagen*. [Phd Thesis 1 (Research TU/e / Graduation TU/e), Applied Physics and Science Education]. Technische Universiteit Eindhoven.
<https://doi.org/10.6100/IR732557>

DOI:

[10.6100/IR732557](https://doi.org/10.6100/IR732557)

Document status and date:

Published: 01/01/2012

Document Version:

Publisher's PDF, also known as Version of Record (includes final page, issue and volume numbers)

Please check the document version of this publication:

- A submitted manuscript is the version of the article upon submission and before peer-review. There can be important differences between the submitted version and the official published version of record. People interested in the research are advised to contact the author for the final version of the publication, or visit the DOI to the publisher's website.
- The final author version and the galley proof are versions of the publication after peer review.
- The final published version features the final layout of the paper including the volume, issue and page numbers.

[Link to publication](#)

General rights

Copyright and moral rights for the publications made accessible in the public portal are retained by the authors and/or other copyright owners and it is a condition of accessing publications that users recognise and abide by the legal requirements associated with these rights.

- Users may download and print one copy of any publication from the public portal for the purpose of private study or research.
- You may not further distribute the material or use it for any profit-making activity or commercial gain
- You may freely distribute the URL identifying the publication in the public portal.

If the publication is distributed under the terms of Article 25fa of the Dutch Copyright Act, indicated by the "Taverne" license above, please follow below link for the End User Agreement:

www.tue.nl/taverne

Take down policy

If you believe that this document breaches copyright please contact us at:

openaccess@tue.nl

providing details and we will investigate your claim.

Multiscale Structure and Mechanics of Collagen

P R O E F S C H R I F T

ter verkrijging van de graad van doctor aan de
Technische Universiteit Eindhoven, op gezag van de
rector magnificus, prof. dr. ir. C. J. van Duijn, voor een
commissie aangewezen door het College voor
Promoties in het openbaar te verdedigen
op dinsdag 1 mei 2012 om 16.00 uur

door

Henry Emmanuel Amuasi

geboren te Sekondi, Ghana

Dit proefschrift is goedgekeurd door de promotor:

prof. dr. M. A. J. Michels

Co-promotor:

dr. C. Storm

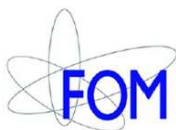
Overige leden:

prof. dr. G. Barkema (Univ. Utrecht/Univ. Leiden)

prof. dr. G. Koenderink (Univ. Amsterdam/AMOLF)

prof. dr. ir. P. van der Schoot (Univ. Utrecht/Tech. Univ. Eindhoven)

Book cover design: **Institute for Complex Molecular Systems (ICMS) Animation Studio**



This work is part of the Industrial Partnership Programme (IPP) Bio(-Related) Materials (BRM) of the Stichting voor Fundamenteel Onderzoek der Materie (FOM), which is supported financially by Nederlandse Organisatie voor Wetenschappelijk Onderzoek (NWO). The IPP BRM is cofinanced by the Top Institute Food and Nutrition and the Dutch Polymer Institute.

CONTENTS

1	Collagen is a Soft Material	1
1.1	Soft Condensed Matter Physics	2
1.2	Introduction to Collagen	2
1.3	Structure of Collagen	3
1.4	Central Question and Organization of this Thesis	7
2	Multiscale Modeling	9
2.1	Single Polymer Mechanics	10
2.2	Bulk Mechanical Properties	16
2.3	Continuum Elasticity Theory of Beams	22
2.4	Elements of Continuum Elasticity Theory	22
2.5	Elastic Beam Bending Theories	23
2.6	Extensible Timoshenko Beam Theory	24
2.7	Internal Forces and Moments	29
2.8	Mechanical Balance Equations	32
2.9	Constitutive Relations	33
2.10	Dimensionless Expressions of Field Equations	33
2.11	Outlook	35
3	Computational Methods	37
3.1	Why not Molecular Dynamics?	38
3.2	Limitations	40
3.3	A Brief on Markov Chain Theory	41
3.4	The Metropolis Algorithm	43
4	Markov Chain Monte Carlo for Polymeric Systems	47
4.1	The Issues of Kinematic Constraints and Network Connectivity	48
4.2	Crank-Shaft $\mathcal{C}(\theta_c)$	50
4.3	The Idea: Tractrix	51
4.4	The Discrete Tractrix Transformation of a Rigid Bond $[\chi(\delta)]$	53
4.5	TRACTRIX for Free Linear Chains $[\mathcal{T}_F(\delta_0)]$	55
4.6	TRACTRIX for Anchored Linear Chains $[\mathcal{T}_A(\Delta)]$	58
4.7	MCMC Simulation of Cross-linked Networks	59

4.8	Trapped Entanglements	62
4.9	Topological Constraints	62
4.10	Another Problem: Loop Counting	64
4.11	The Gauss Linking Number	65
4.12	Summary and Outlook	67
5	Validation of TRACTRIX	69
5.1	Freely-Jointed Chains	70
5.2	Worm-like Chains and Semi-flexible polymers	71
5.3	Bundles of Three Cross-linked Worm-like Chains	73
5.4	Summary and Outlook	74
6	A 3D Mechanical Model of a Fibril	77
6.1	Introduction	78
6.2	The Model	82
6.2.1	The Bending Energy	82
6.2.2	The Excluded Volume Interaction	84
6.2.3	The Attractive Interactions	86
6.2.4	The External Work	93
6.2.5	Cross-linking: The Connectivity Graph	94
6.2.6	Preparing the Fibril's Initial State	95
6.3	The Monte Carlo Move Set \mathcal{M}	99
6.3.1	Crank-Shaft $\mathcal{C}(\theta_c)$	101
6.3.2	TRACTRIX for Free Chains $\mathcal{T}_F(\delta)$	101
6.3.3	TRACTRIX for Anchored Chains $\mathcal{T}_A(\Delta)$	102
6.3.4	TRACTRIX for Fibrils $\mathcal{T}_{AB}(\mathcal{R})$	102
6.4	Results	105
6.5	Discussion	110
6.5.1	Fibrillar Young's Modulus	110
6.5.2	Writhing and Residual Entropic Effects	118
6.5.3	Possible Additional Contributions to Fibril Mechanics	119
6.5.4	Molecular Crimp and Length Storage	120
6.5.5	Appropriateness of Timoshenko Framework	122
6.6	Summary and Outlook	122
6.A	Jacobian Calculations	123
7	Conclusions and Outlook	127
7.1	Conclusions	128
7.2	Outlook	129
7.2.1	Limitations and Suggestions for TRACTRIX (Chapter 4)	129
7.2.2	Collagen Fibril (Chapter 6)	130
	Bibliography	133

CONTENTS**vii**

Summary	141
Publications	145
Curriculum vitae	147

CHAPTER 1

COLLAGEN IS A SOFT MATERIAL

Advances in modern physics over the last century have been marked by an increased theoretical understanding of the interactions of matter at extremely small (subatomic) and extremely large (cosmological) length scales. These breakthroughs have led to the development of the popular sciences, such as string theory, quantum physics, relativity and cosmology, in which there is now a flurry of intense research. Interactions in matter occurring in the ‘middle’ regime of length scales have received no less attention. These are the domain of soft condensed matter physics which has had a long and venerable history, and yet still abounds with a rich variety of many yet unsolved physical phenomena which seem to arise chiefly from complexity in these systems.

Using the principles of soft condensed matter physics, we have conducted research in the computational modeling of the most abundant naturally-occurring protein on earth, namely collagen, which is a typical example of a soft biological material. In this thesis, we aim to present the new computational methods that have been developed in my research to aid in achieving an understanding of the design principles for the mechanical behaviour of collagen. In this chapter we review the essential features of collagenous tissue that were used in this work, and present the outline for the rest of the thesis.

1.1 Soft Condensed Matter Physics

Complexity is a term generally used to describe a system composed of numerous interconnected parts that as a whole exhibit emergent properties not immediately obvious from the properties of its constituent parts. It is an apt description of the so called ‘soft materials’ that form a crucial part of our daily experience. These soft materials range from the food we eat, the clothes we wear, the cleansing agents we apply on our bodies, to the very living tissue that we are made of. Their physical properties, for instance their mechanical behaviour, depend to various degrees on the interactions and organization of their constituent macromolecules.

What remains perhaps an enduring mystery is that living organisms have long possessed an uncanny ability to harness this complexity for their daily survival (a process without which none of us would be alive), while the human race, as sentient observers, is only now just beginning to develop a complete theoretical understanding of how to manipulate these features to our advantage.

Condensed matter physics provides a framework for describing and determining what happens to large groups of particles when they interact via presumably well-known forces [1]. This framework embodies the principles that have guided me during this research. Matter occurring at extremely small length scales is typically mediated by a very high interaction energy per degree of freedom, measured in units greater than or equal to electron-volts ($1 \text{ eV} \sim 10^{-19} \text{ J}$), and is the domain of quantum mechanics and related theories. In soft condensed matter, quantum aspects are generally unimportant for phenomena occurring in the middle regime of length scales, which typically involve energies per degree of freedom in the thermal range, often quoted in units of $k_B T$, where k_B is Boltzmann’s constant and T is the absolute temperature. At room temperature, $T = 25^\circ\text{C}$ thus $k_B T = 4.1164 \times 10^{-21} \text{ J}$, whereas at physiological temperature in man, $T = 37^\circ\text{C}$ thus $k_B T = 4.2800 \times 10^{-21} \text{ J}$.

Collagen, which we will describe in more detail in the following section, is a common soft material occurring within the bodies of multicellular organisms (that is, *in vivo*) where physiological temperature is often more relevant. Still, many laboratory experiments can be performed on collagen outside the body (that is, *in vitro*). So like many other soft materials, the physics of collagen, particularly its mechanics, can be described using the principles of soft condensed matter physics.

1.2 Introduction to Collagen

Among all naturally-occurring proteins found in the body of any animal or human, collagen is the most plentiful, forming about 25% of the human proteome. Collagen is also a highly functional material exhibiting a wide range of

fascinating features that have been the subject of intense research for almost a century [2]. These features include, among other things, its self-assembly [3], structure [4], piezoelectric [5] and pyroelectric [6] properties, and effective mechanical properties [7, 8].

There are 28 different types of collagens numbered with roman numerals I - XXVIII (classified according to their chemical or genetic composition) which can be broadly categorized into the fibrillar and non-fibrillar collagens [9]. Collagen occurs in many different places throughout the body. The five most common types and where they may be found in the body are as follows:

- Type I collagen (fibrillar): skin, tendon, vascular ligature, organs, bone (main component of the organic part of bone).
- Type II collagen (fibrillar): cartilage (main component of cartilage).
- Type III collagen (fibrillar): reticulate (main component of reticular fibers), commonly found alongside Type I.
- Type IV collagen (non-fibrillar): forms bases of cell basement membrane.
- Type V collagen (fibrillar): cell surfaces, hair and placenta.

Over 90% of the collagen in the body, however, is Type I collagen. For this reason, in the present work we focus on the effective mechanical properties of Type I collagen fibrils and how these properties are related to its dimensions, underlying structure, and intermolecular interactions.

The relevance of such a study is attested to by its numerous potential applications including the medical diagnoses of diseases, such as Ehlers-Danlos syndrome and *osteogenesis imperfecta*¹. Collagen-related diseases most commonly arise from genetic defects or nutritional deficiencies that affect the biosynthesis, assembly, postranslational modification, secretion, or other processes involved in normal collagen production.

This study is also important in understanding the material design principles exhibited in nature so as to guide and inspire the design of new synthetic materials, including the so called 'biomimetic materials' in tissue engineering, with particular prescribed properties and functionality.

1.3 Structure of Collagen

Let us now review the structural features of collagenous tissue which provide cues for modeling collagen.

¹Ehlers-Danlos is a genetic disease affecting the skin, muscles, ligaments, blood vessels and visceral organs. It is due to a defect in the synthesis of Type I collagen. It is often characterized by a significant decrease in resistance to deformation of these organs. For instance, it can result in hyperelastic skin, that is, skin that can be stretched beyond what is considered normal. *Osteogenesis imperfecta* is a genetic bone disorder in which bones are deficient in Type I collagen, so that they become unusually brittle.

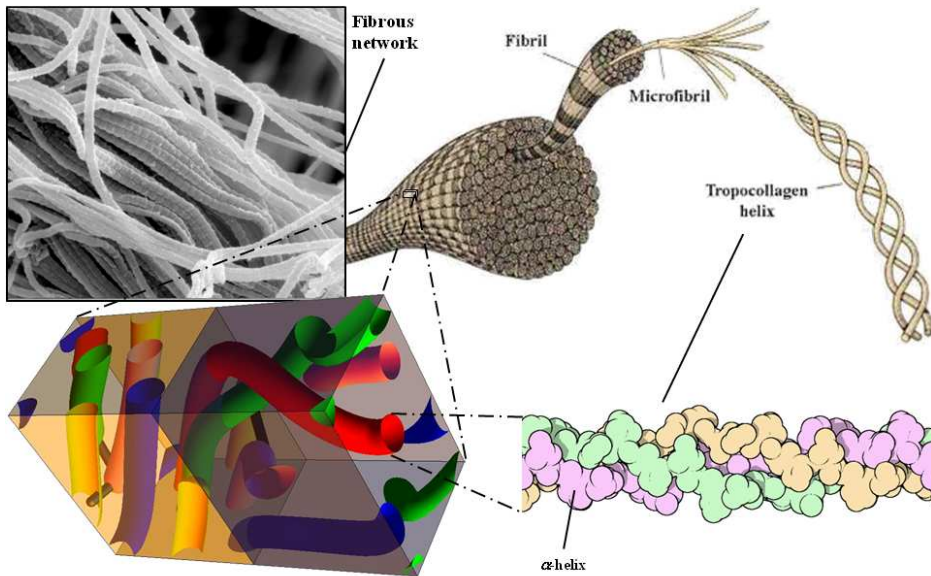


Figure 1.1: Illustrating the hierarchical organization of collagenous tissue. The photographic inset is an electron micrograph (source: FEITM image gallery) of fibrous collagen, about $2\ \mu\text{m} \times 2\ \mu\text{m}$, found in knee joint capsule tissue. Each fiber is an assembly of long fibrils mediated by special proteins known as glycosaminoglycans (not shown). Each fibril is thought to consist of thinner versions of fibrils called microfibrils. The enlarged cuboid is a representation of the proposed triclinic unit cell of a perfectly crystalline microfibril [4] (which has been 10-times compressed along the horizontal) containing specific sections of the tropocollagen molecule. Each tropocollagen molecule is a right-handed triple-helix of left-handed polypeptide strands called α -helices.

Collagen tissue structure is characterized by the highly hierarchical organization of its molecules (see Figure 1.1). This complex organization extends over many length-scales (from angstroms to millimeters), and involves numerous degrees of freedom, which is part of the reason why up till now they have proven to be so difficult to simulate, despite today's computational advances.

Beginning at the nanometer-scale, the molecule *tropocollagen*, made up of more than 50 000 atoms, about 1.5 nm in diameter, and 300 nm long, is the main building block, which in the connective tissue of our bodies, is usually produced by fibroblasts². More precisely, tropocollagen is built out of three parallel left-handed helical polypeptides, called alpha-helices. Each alpha-

²Strictly speaking fibroblasts produce and secrete procollagen, a precursor of tropocollagen. After secretion from a fibroblast certain post-translational processes occur that convert procollagen into tropocollagen. This production process is mimicked by the so-called *de novo* laboratory production of collagen from a medium of cultured fibroblasts obtained from normal human skin, and that can take place outside the body [10]

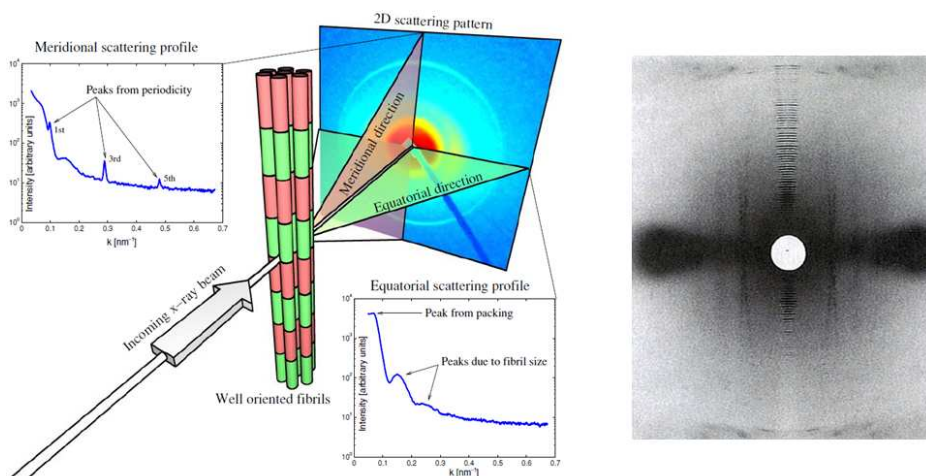


Figure 1.2: (Left) Illustration of meridional and equatorial scattering from collagen fibrils (Source: Ref. [14]). (Right) Typical X-ray diffraction pattern obtained from rat-tail tendon (collagen) with fibrils aligned along the vertical. (Source: [18]).

helix is a strand of more than 1 000 amino acid residues. These strands are intertwined to form a right-handed helical structure known as a triple-helix (see Figure 1.1).

The tight packing of the alpha-helices within the triple helix mandates that every third residue be glycine (Gly), resulting in a repeating Xaa-Yaa-Gly sequence, where Xaa and Yaa can be any amino acid. This repeat occurs in all types of collagen, although it is disrupted at certain locations within the triple-helical domain of nonfibrillar collagens [11]. The amino acids in the Xaa and Yaa positions of collagen are often Proline (Pro, 28%) and Hydroxyproline (Hyp, 38%), respectively. Pro-Hyp-Gly is the most common triplet (10.5%) in collagen [12].

Upon their secretion from fibroblasts, numerous tropocollagen molecules spontaneously self-assemble and become packed and later cross-linked in a roughly parallel but staggered formation, forming fine micrometer-long bundles called microfibrils. A lot of effort has been concentrated in elucidating the packing order of tropocollagen molecules within the microfibril [13, 14, 15, 4, 16, 17] chiefly by postulating models that simulate as closely as possible X-ray scattering from collagen fibrils (see, for instance, Figure 1.2). The most detailed proposed arrangement of tropocollagen molecules within a microfibril, that results in an X-ray diffraction pattern that most closely matches the experimental X-ray diffraction image obtained in the laboratory, has been proposed by Orgel et al. [4] using synchrotron radiation. This proposed ar-

rangement presents the microfibril as a liquid crystal³ with varying amounts of well-ordered crystallite domains, each being a weakly twisted quasi-hexagonal columnar array of tropocollagen molecules. The crystal structure of these domains can be generated by the periodic repetition of a triclinic unit cell containing specific sections of tropocollagen molecules (see Figure 1.1). Full consensus over this proposed crystalline model has not been reached [19]. Another model, obtained by second harmonic generation (SHG) microscopy, sees the microfibril as a quasi-crystalline array of tropocollagen molecules [20].

The dimensions of microfibrils depend on the location (within the body) of the tissue of which the microfibril is a part of [21]. Furthermore, *in vitro* experiments show that the size and strength of these microfibrils depend rather sensitively on ambient conditions [22] as specified by the wetness, pH, temperature, ionic strength, on the intactness of the tropocollagen molecules [23, 24], and on the mechanism and extent of cross-linking between tropocollagen molecules.

Cross-linking in collagen fibrils is a slow process that occurs after the self-assembly is complete. The cross-linking agents in collagen microfibrils are not external chemical entities but are relatively short non-helical polypeptide chain appendages, not containing the Xaa-Yaa-Gly sequence, called telopeptides that occur at both ends of (and are part of) every tropocollagen molecule, and that covalently bond (via Schiff base links⁴) to specific sites on the helical regions of neighboring tropocollagen molecules. The exact cross-linking sites on the helical regions of the tropocollagen molecule are not precisely known [25]. But a number of different sites have been implicated for cross-linking [4], and the mechanics of a microfibril will likely depend on which cross-linking mechanism is chosen. Cross-linking is catalytically controlled by means of a copper-containing enzyme known as *lysyl oxidase*.

Microfibrils go on to associate with one another, *in vivo*, to form thicker fibrils, which in turn associate with one another to form fibers, the main structural unit of fibrous tissue. In contrast, *in vitro*, reconstituted fibrils often associate with one another to form network gels⁵.

³We note here that the collagen fibril should not strictly be looked upon as a liquid crystal as it has not been observed to exhibit certain phase transitions, such as the smectic to nematic phase transition, characteristic of true liquid crystals. However, the term 'liquid crystal' merely hints at the orientational and positional order or disorder observed in the packing arrangement of tropocollagen molecules.

⁴Schiff base formation involves an allysine residue and uncharged lysine residue of another properly juxtaposed tropocollagen molecule.

⁵It is thought that the fibroblasts themselves aid in the formation of fibrils *in vivo*. It has also been observed that *in vivo* special cross-linking proteins known as glycosaminoglycans link the fibrils together to form fibers [26].

1.4 Central Question and Organization of this Thesis

So, collagen is a highly relevant, and intricately hierarchical biological material. The central question we address in this thesis is whether we may understand its mechanical response in a manner that respects and exploits its multiple length-scales. In order to achieve this, we first review the challenges in multiscale modeling of biological materials (Chapter 2), and summarize the essential concepts from statistical and continuum mechanics as required for an accurate description of the physics at the smallest and largest length-scales, that we will employ in this work. In Chapter 3, we review the available and existing computational methods and motivate our choice for Markov Chain Monte Carlo (MCMC) as our principal computational vehicle. In Chapter 4, we outline the computational and practical challenges associated with using MCMC in hierarchical architectures of cross-linked polymers, and present the TRACTRIX algorithm that we have developed to address them. Also in Chapter 4, we elaborate on the TRACTRIX method to adapt it to realistically complex settings, including the ability to deal with excluded volume and trapped entanglements (non-crossing) constraints. In Chapter 5, we apply TRACTRIX to several arrangements of chains to assess its accuracy. In Chapter 6, we use advanced TRACTRIX to simulate a mechanical experiment on a collagen fibril, representing the fibrillar structure by its native, experimentally determined 3-dimensional arrangement. We review this structure, its topology and the manner in which the fibril is stabilized to retain its native shape, and finally execute a tip-loaded cantilever experiment from which we extract the effective mechanical parameters to be used in an effective coarse-grained mechanical model of the collagen fibril. We compare these to values obtained in experiment and different simulational settings. Finally, in the discussion, we outline remaining modeling issues, present suggestions for further refinement and future directions.

CHAPTER 2

MULTISCALE MODELING

We outline the first stages in the multiscale modeling of biopolymer materials, starting with the statistical mechanics of single stiff chains. In the first coarse-graining step, we demonstrate how to integrate out the single polymer degrees of freedom in supramolecular assemblies of such semi-flexible polymers to arrive at an effective network mechanical model for the linear and nonlinear behavior of cross-linked assemblies of such polymers. We review the continuum mechanical description of bending beams, as this is the specific loading condition we shall be applying to the fibrils later in the thesis.

The contents of this chapter have been published in:
Multiscale Materials Modeling Conference Proceedings MMM2010, **637-646** (2010).

Intimately involved in the function of cells and tissues is the mechanics of their constituent and surrounding elements. For instance, inside animal cells, the *cytoskeleton* is a dynamic structure that maintains cell shape, protects the cell, and enables cellular motion. The principal components of the cytoskeleton are *intermediate filaments*, *microtubules* and *actin* filaments, each of which possess unique mechanical properties. The tissue that often surrounds animal cells is called the *connective tissue*, its defining component being the *extracellular matrix*, which among other functions provides structural support for the cell. The main ingredient of connective tissue is *collagen* and it is the most abundant protein in mammals forming about 25% of total protein content. Like many biological filaments, collagen structure is highly hierarchical - see Figure 1.1. One of the central goals in tissue and cell mechanics is to understand and explain the constitutive behavior of these hierarchical materials, at macroscopic scales, in terms of the underlying microstructural properties and architecture[4]. In biological materials, a jump across the scales often involves translating or re-interpreting results from statistical mechanics in terms of effective, continuum-mechanical quantities such as the shear modulus.

Our intention in this chapter is to provide a brief introduction to the subject and demonstrate in some detail how to actually compute mechanical properties in various situations.

2.1 Single Polymer Mechanics

Modeling the mechanical properties of hierarchical biological structures ranging from individual polymeric molecules such as tropocollagen to large-scale macroscopic tissues is currently an active area of research[27, 28]. The primary challenge is the very large number of degrees of freedom and the many different length scales inherent in their structure that need to be taken account of in order to perform a fully atomistic simulation of a sufficiently large sample of tissue. But even for the fastest computers today atomic-level simulations of such hierarchical polymeric systems is impossible, hence there is a need for *coarse-graining* approximations at multiple scales in which only coarse-scale features of the molecular conformations are tracked, while small-scale, fast dynamics are assumed to remain at local equilibrium, subject to the constraints imposed by the „slow“ variables being tracked[29]. The results gleaned at one scale may be fed as input into the next highest scale in the hierarchy, and so on until a complete analysis of the tissue sample at all its relevant multiple scales has been characterized, hence the term *multiscale*. In biophysics, the most commonly used coarse-grained models of polymer chains are the *freely-jointed chain* (FJC) and the *worm-like chain* (WLC)[30, 31, 32, 33]. The FJC may be described as a linear series of a large number N of connected rigid rods $\mathbf{t}_1, \mathbf{t}_2, \dots, \mathbf{t}_N$ of fixed length b interlinking the sequence of points $\mathbf{r}_0, \mathbf{r}_1, \dots, \mathbf{r}_N$, so

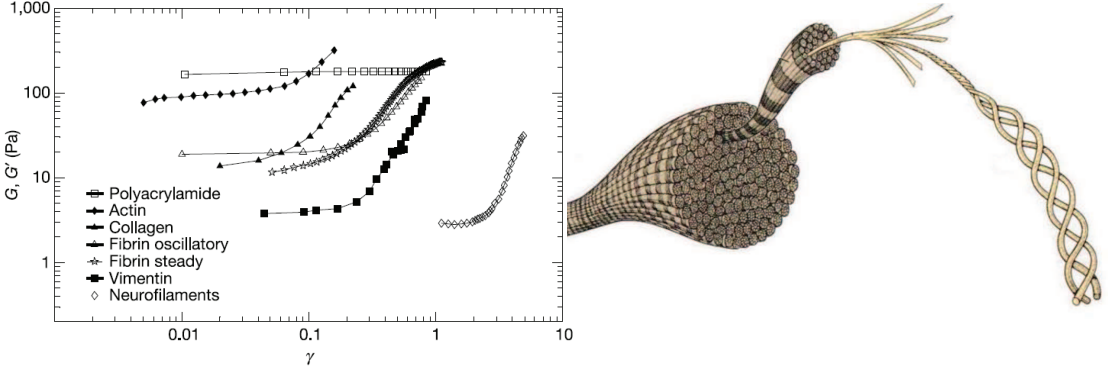


Figure 2.1: Dynamic shear storage moduli measured at different strain amplitudes for a series of cross-linked biopolymer networks. The real part, G' , of the storage modulus reduces to the shear modulus G at zero frequency. Data shown are G' (at 10 rad s^{-1}) values for F-actin, fibrin, collagen, vimentin and polyacrylamide, and shear modulus G for fibrin and neurofilaments, plotted as a function of the dimensionless strain γ (right hand side, from [34]). Mechanical properties arise from the structure and properties at molecular and supramolecular length scales. In the case of collagen (right hand side, from H.A. Campbell *Biology* (1995)), the fibrillar hierarchy is particularly spectacular.

that the i -th bond $\mathbf{t}_i = \mathbf{r}_i - \mathbf{r}_{i-1}$. Each rod is free to rotate in any direction with respect to its nearest neighbor(s). The FJC is often used to represent highly flexible polymers for there is no correlation in orientation between any of the rods. Though real polymers are not FJCs, an FJC will have the same equilibrium mean square end-to-end length $\langle R_0^2 \rangle$ and fully extended length ℓ_c as any real polymer if the freely jointed step length b and the number of steps N of the freely jointed chain are chosen appropriately.

Now imagine that the FJC is tethered to a fixed wall at one end while the other end is pulled so that the end-to-end vector of the polymer is always in a fixed orientation (This is a typical scenario in an optical bead pulling experimental setup in the laboratory). The puller will experience an average reaction that depends on the rate of change of the chain's free energy with end-to-end vector \mathbf{R} of the chain. As each of the FJC's rods are free to rotate thus costing no energy, the free energy $F(\mathbf{R})$ of the FJC is entirely entropic depending only on the number of conformations $\Omega(R)$ that possess an end-to-end distance R :

$$F(R) = -k_B T \log \Omega(\mathbf{R}) = -k_B T \log(P(\mathbf{R}; N, b)) + F_0, \quad (2.1)$$

where k_B is Boltzmann's constant and T is the absolute temperature. In the second equality we have used the fact that the number $\Omega(\mathbf{R})$ is directly proportional to the probability density $P(\mathbf{R}; N, b)$ of the chain having an end-to-end vector between \mathbf{R} and $\mathbf{R} + d\mathbf{R}$. In the limit of large N ($N \gtrsim 30$), it is well

approximated by a Gaussian distribution:

$$P(\mathbf{R}; N, b) = \left(\frac{3}{2\pi Nb^2} \right)^{3/2} \exp\left(\frac{-3R^2}{2Nb^2} \right), \quad (2.2)$$

where $R = |\mathbf{R}|$. For $Nb \gg R$ the force-extension relation is straight-forwardly obtained as

$$\langle f(R) \rangle = -\frac{\partial F(\mathbf{R})}{\partial R} = k_B T \frac{3R}{Nb^2}, \quad (2.3)$$

which corresponds to the expression for an *entropic spring* with spring constant $k_e = 3k_B T / (Nb^2)$.

Note that the above expression is valid for the *average* force $\langle f(R) \rangle$ applied by a puller in order to keep the FJC at a *fixed* end-to-end distance R from its other end, the so-called *Helmholtz ensemble*. Another ensemble, namely the *Gibbs ensemble*, instead fixes the external force \mathbf{f} (with magnitude f) and measures the average end-to-end distance $\langle R(\mathbf{f}) \rangle$. The Hamiltonian of the Gibbs

ensemble for the FJC is $\mathcal{H} = -\sum_{i=1}^N \mathbf{f} \cdot \mathbf{t}_i$, and it can be shown by computing the configurational partition function $\mathcal{Z}_f \equiv \sum_{\{\mathbf{t}_i\}} \exp(-\mathcal{H}/k_B T)$ that

$$\langle R(f) \rangle = k_B T \frac{\partial \log \mathcal{Z}_f}{\partial f} = Nb \mathcal{L}\left(\frac{fb}{k_B T} \right), \quad (2.4)$$

where $\mathcal{L}(x) \equiv \coth(x) - 1/x$ is the Langevin function. For small x , $\mathcal{L}(x) \approx x/3$ and thus for $fb \ll k_B T$ we obtain

$$f = k_B T \frac{3\langle R(f) \rangle}{Nb^2}, \quad (2.5)$$

which is equivalent to the relation obtained for the Helmholtz ensemble in Equation (2.3) for small extensions. From Equation (2.4) we deduce that for large applied forces, the FJC exhibits $R(f) \sim 1 - k_B T / (fb)$ asymptotic behaviour.

Even though the FJC force-extension relations are known to work well in the small force/extension regime of many real polymers, they do not correctly describe those of stiff polymers near full extension or with large applied forces ($fb \gg k_B T$). This discrepancy is demonstrated in the force-extension data plot (see Figure 2.2) of double stranded DNA. To explain the discrepancy, we first note that as the extensional force increases, it becomes more and more possible to straighten out the shorter wavelength fluctuations of the chain. However, the FJC does not describe chain fluctuations with wavelength shorter than b . Therefore when the extensional force reaches $f_c \sim k_B T / b$ it amounts to more extension in the chain than it would if there were still more fluctuations of wavelength b or shorter to cancel out.

Another polymer model, due to Kratky and Porod [30], which incorporates these short wavelength fluctuations is the worm-like chain (WLC). The WLC better describes the mechanics of stiff polymers. It is specified by a continuously differentiable space curve $\mathbf{r}(s)$ of length ℓ_c parametrized by the arc length parameter s . It is further endowed with a Hamiltonian that quantifies the cost of bending the curve:

$$\mathcal{H}[\mathbf{r}(s)] = \frac{\kappa}{2} \int_0^{\ell_c} ds \left(\frac{d^2 \mathbf{r}(s)}{ds^2} \right)^2, \quad (2.6)$$

where κ is the bending modulus. Hidden in this definition is the constraint of *local inextensibility*, that is, the local tangent magnitude $|\hat{\mathbf{t}}| = |d\mathbf{r}/ds|$ is unity. An important length-scale that arises from this model is the *persistence length* ℓ_p which is the characteristic length governing the decay of tangent-tangent correlations and provides a quantitative measure for a polymer's flexibility. The persistence length is defined through the relation

$$\langle \hat{\mathbf{t}}(s) \cdot \hat{\mathbf{t}}(s + \Delta s) \rangle \equiv \exp(-\Delta s / \ell_p) = \exp(-\Delta s k_B T / \kappa). \quad (2.7)$$

Thus for the WLC $\ell_p = \kappa / k_B T$. Though the specification of the WLC model appears to be simple, the constraint of local inextensibility leads to considerable mathematical difficulty when attempting to obtain a closed form expression for its force-extension curve without making further simplifying assumptions. One such assumption we will consider in the next subsection.

We can however, using Equation (2.7), obtain the average square end-to-end distance:

$$\langle R_0^2 \rangle = \left\langle \left(\int_0^{\ell_c} ds \hat{\mathbf{t}}(s) \right)^2 \right\rangle = \int_0^{\ell_c} ds \int_0^{\ell_c} ds' \langle \hat{\mathbf{t}}(s) \cdot \hat{\mathbf{t}}(s') \rangle = 2\ell_p^2 \left(\frac{\ell_c}{\ell_p} + e^{-\frac{\ell_c}{\ell_p}} - 1 \right). \quad (2.8)$$

It follows that for highly flexible WLCs where $\ell_c \gg \ell_p$ we have

$$\langle R_0^2 \rangle \approx 2\ell_p \ell_c. \quad (2.9)$$

Comparing the right-hand-side of the above expression with the FJC result: $\langle R_0^2 \rangle = Nb^2$, and furthermore recognizing that $\ell_c = Nb$ we may obtain the equivalent FJC of the flexible WLC by setting $b = 2\ell_p$. Using Equation (2.5) the small force-extension relation for the flexible WLC ($\ell_c \gg \ell_p$) thus becomes

$$f = k_B T \frac{3\langle R(f) \rangle}{2\ell_p \ell_c}. \quad (2.10)$$

A *semi-flexible chain model* (SF-WLC) is the worm-like chain model which has the further assumption that its persistence length ℓ_p is so large in comparison with its contour length ℓ_c to the extent that, even when it is not under tension,

the WLC's backbone thermal undulations allow only infinitesimal deviations from its fully extended state. In such a case, consider that the SF-WLC is tethered at the origin while the other end is being pulled along the z -axis. Any unit tangent vector $\hat{\mathbf{t}}(s)$ at any point along the backbone thus has a z -component t_z close to unity while its transverse component $\hat{\mathbf{t}}_{\perp}(s) = \{t_x(s), t_y(s)\}$ is infinitesimal. With such assumptions and under the subsection of a constant extensional force of magnitude f along the z -axis the Hamiltonian of the WLC becomes, to leading order in $\hat{\mathbf{t}}_{\perp}(s)$,

$$\mathcal{H}[\hat{\mathbf{t}}_{\perp}(s)] \approx \frac{\kappa}{2} \int_0^{\ell_c} ds \left[\left(\frac{d\hat{\mathbf{t}}_{\perp}(s)}{ds} \right)^2 - f \left(1 - \frac{1}{2} |\hat{\mathbf{t}}_{\perp}(s)|^2 \right) \right]. \quad (2.11)$$

As the inextensibility constraint is implicit in this formulation of the SF-WLC, it lends itself very well to Fourier analysis. We will not detail all of the steps here, but the end result is well known: the Equipartition Theorem yields the Fourier spectrum of transverse fluctuations as

$$\langle |\mathbf{t}_q|^2 \rangle = \frac{4k_B T}{\ell_c} \frac{1}{\kappa q^2 + f}, \quad (2.12)$$

where \mathbf{t}_q is defined by $t_x(s) + it_y(s) \equiv \sum_q \mathbf{t}_q \sin(qs)$, $q = \frac{n\pi}{\ell_c}$ ($n = 1, 2, 3, \dots$). Summing all the modes to reconstruct $\langle |\hat{\mathbf{t}}_{\perp}|^2 \rangle$, we find

$$\langle |\hat{\mathbf{t}}_{\perp}|^2 \rangle = \frac{2k_B T}{\ell_c} \sum_q \frac{1}{\kappa q^2 + f} = \frac{2\ell_c}{\ell_p} \sum_{n=1}^{\infty} \frac{1}{(\pi n)^2 + \varphi} = \left(\frac{\ell_c}{\ell_p} \right) \frac{1}{\varphi} [\sqrt{\varphi} \coth(\sqrt{\varphi}) - 1], \quad (2.13)$$

where $\varphi = f\ell_c^2/\kappa$. From this we infer the extension-force curve:

$$\langle \ell \rangle(\varphi) = \ell_c \left(1 - \frac{1}{2} \langle |\hat{\mathbf{t}}_{\perp}|^2 \rangle \right) = \ell_c - \left(\frac{\ell_c^2}{2\ell_p} \right) \frac{1}{\varphi} [\sqrt{\varphi} \coth(\sqrt{\varphi}) - 1]. \quad (2.14)$$

In the high force limit, $f \gg \kappa/\ell_c^2$, we obtain to leading order

$$\langle \ell \rangle(\varphi) \sim \ell_c \left(1 - \frac{1}{2} \sqrt{\frac{k_B T}{\ell_p f}} \right), \quad (2.15)$$

which turns out to be the correct behaviour for the high force limit of the extension-force curve also for *flexible* WLCs (see inset of Figure 2.2) since the only assumption we have made in this derivation is that transverse fluctuations are infinitesimal, a situation that also occurs with low ℓ_p WLCs subjected to high forces. An approximate interpolation formula that summarizes the low-force and high-force limits of the WLC force-extension curve and gives a maximum relative error of 10% in between these limits is

$$f(\ell) = \frac{k_B T}{\ell_p} \left[\frac{1}{4(1 - \ell/\ell_c)^2} - \frac{1}{4} + \frac{\ell}{\ell_c} \right]. \quad (2.16)$$

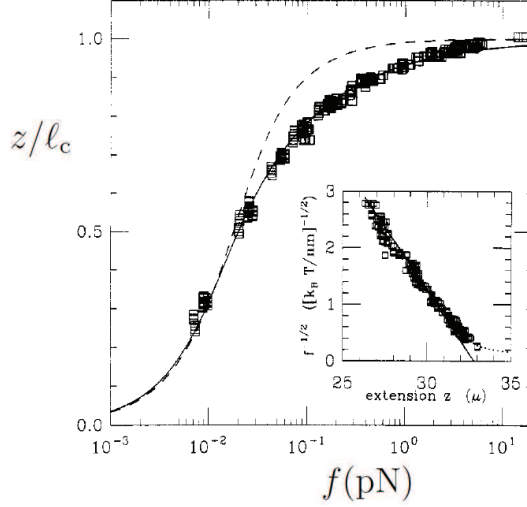


Figure 2.2: Fit of numerical exact solution of the WLC extension-force curve to experimental data of Smith et al. (97 004 bp DNA, 10 mM Na⁺). The best parameters for a global least-squares fit are $l_c = 32.8$ pm and $l_p = 53$ nm. The FJC result for $b = 2l_p \approx 100$ nm (dashed curve) approximates the data well in the linear low-force regime but scales incorrectly at large f and provides a qualitatively poorer fit. Inset: $f^{-1/2}$ vs z for the highest forces; the exact WLC result (solid line) is in this plot a straight line extrapolating to $l_c = 32.8$ pm from which the experimental points begin to diverge above $z = 31$ pm. [31]

From Equation (2.14) we can also compute the equilibrium length of the SF-WLC:

$$l_{\text{eq}} = \lim_{\varphi \rightarrow 0} \langle \ell \rangle(\varphi) = l_c \left(1 - \frac{l_c}{6l_p} \right), \quad (2.17)$$

and use this to extract the extension away from the equilibrium length at a given force. Scaling this extension by l_c^2/l_p in order to make everything dimensionless we obtain

$$\langle \delta \tilde{\ell} \rangle(\varphi) = \left(\frac{l_c^2}{l_p} \right)^{-1} (\langle \ell \rangle(\varphi) - l_{\text{eq}}) = \frac{\varphi - 3\sqrt{\varphi} \coth(\sqrt{\varphi}) + 3}{6\varphi}, \quad (2.18)$$

which is the extension-force relation for a SF-WLC in universal form. For small φ , that is, $f \ll \kappa/l_c^2$ we obtain

$$\langle \delta \tilde{\ell} \rangle(\varphi) = \frac{\varphi}{90}, \quad (2.19)$$

which implies an effective linear entropic spring with spring constant $k_{\text{SF}} = 90k_B T l_p^2 / l_c^4$.

Real polymers, and certainly all biologically relevant ones, are not perfectly inextensible. Rather, they have a fairly high but nonzero modulus for the extension of the backbone itself. As we have seen, the entropic elasticity in the WLC (see, for instance, Figure 2.2) displays a true divergence near full extension. At some point, therefore, no matter how energetically costly it might be, the enthalpic stretching of the backbone will take over. Without going into details, we quote here the result for the modified force-extension relation of a stretching and bending semi-flexible polymer [33]:

$$\langle \ell \rangle_K(f) = \left(1 + \frac{f}{K}\right) \langle \ell \rangle_{K=0} \left(f \left(1 + \frac{f}{K}\right)\right). \quad (2.20)$$

2.2 Bulk Mechanical Properties

Now that we have outlined how to extract the force-extension behavior for single, semi-flexible polymers, we are ready to assemble many such polymers into a network. The key question is, obviously, what this network will behave like when deformed. Clearly, the single-filament properties will feature crucially in this response.

In the Lagrangian formulation of continuum mechanics, the deformation of a material is fully characterized by the strain tensor

$$u_{ij}(\mathbf{x}) = \frac{1}{2} \left[\Lambda(\mathbf{x})^T \Lambda(\mathbf{x}) - \mathbb{1}_3 \right], \quad (2.21)$$

with $\Lambda(\mathbf{x})$ the Cauchy deformation tensor, and (\mathbf{x}) is a point within the elastic medium under consideration. In terms of this strain tensor, the harmonic elastic free energy is

$$\mathcal{F}_{\text{el}} = \frac{1}{2} \int d^3x C_{ijkl} u_{ij}(\mathbf{x}) u_{kl}(\mathbf{x}) = \frac{1}{2} \int d^3x \sigma_{ij}(\mathbf{x}) u_{ij}(\mathbf{x}) \equiv \int d^3x f_{\text{el}}, \quad (2.22)$$

where $\sigma_{ij}(\mathbf{x})$ is the Cauchy stress tensor, and f_{el} is the elastic free energy density, and the integral is taken over the volume of the material. The fourth-rank elastic constant tensor C_{ijkl} , in principle, possesses $3^4 = 81$ independent components. Symmetries reduce this number to 21, and the requirement that for an isotropic material, it should be invariant under arbitrary rotations and reflections leave only two components, so that

$$C_{ijkl} = \lambda \delta_{ij} \delta_{kl} + \mu (\delta_{ik} \delta_{jl} + \delta_{il} \delta_{jk}). \quad (2.23)$$

Inserting this form into the expression for the free energy, we recover the Lamé formula for the elastic energy density

$$f_{\text{el}} = \frac{1}{2} \lambda u_{kk}^2 + \mu u_{ij} u_{ij} \quad (2.24)$$

(here Einstein summation has been assumed). The coefficients λ and μ are related to the moduli of the material, which we recover upon splitting the strain tensor into traceless and diagonal parts:

$$f_{\text{el}} = \frac{1}{2} \left(\lambda + \frac{2\mu}{d} \right) u_{kk}^2 + \mu \left(u_{ij} - \frac{1}{d} \delta_{ij} u_{kk} \right)^2 \equiv \frac{1}{2} K u_{kk}^2 + \mu \left(u_{ij} - \frac{1}{d} \delta_{ij} u_{kk} \right)^2. \quad (2.25)$$

d is the dimension of space, K is the bulk modulus, and μ the shear modulus. In rheology, it is common practice to designate the shear modulus with G , and we shall follow this convention in the remainder. The constitutive equation, in terms of the material moduli, reads

$$\sigma_{ij} = K \delta_{ij} u_{kk} + 2G \left(u_{ij} - \frac{1}{d} \delta_{ij} u_{kk} \right). \quad (2.26)$$

Let us consider the example of an isotropic 3D material, loaded in simple shear, for which the (bulk) Cauchy deformation tensor the (bulk) strain tensor and the stress tensor, respectively, read

$$\Lambda_{\text{B}}(\gamma) = \begin{pmatrix} 1 & 0 & \gamma \\ 0 & 1 & 0 \\ 0 & 0 & 1 \end{pmatrix}; \quad \mathbf{u}_{\text{B}} = \frac{\gamma}{2} \begin{pmatrix} 0 & 0 & 1 \\ 0 & 0 & 0 \\ 1 & 0 & 0 \end{pmatrix}; \quad \sigma_{\text{B}} = G \gamma \begin{pmatrix} 0 & 0 & 1 \\ 0 & 0 & 0 \\ 1 & 0 & 0 \end{pmatrix}. \quad (2.27)$$

We see that the strain tensor \mathbf{u} has $u_{kk} = \text{Tr}(\mathbf{u}) = 0$ and $\sum_{ij} u_{ij}^2 = \frac{1}{2} \gamma^2$ and according to Equation (2.25), we may therefore write that $f_{\text{el}}(\gamma) = \frac{1}{2} G \gamma^2$. In (strain controlled) rheological experiments, the modulus in practice is extracted from the shear stress tensor component σ_{xz} (which, from Equation (2.27), is equal to $G\gamma$), and may be measured in two distinct and different ways: the so-called *secant* shear modulus is defined as the ratio of instantaneous shear stress to strain $G_S = \sigma_{xz}/\gamma$, while the *differential* or *tangential* modulus is defined as the instantaneous derivative $G_T = \partial \sigma_{xz} / \partial \gamma$, both moduli being constant for linear materials. For nonlinear materials, we generalize these definitions to arbitrary strains: $G_S(\gamma) = \sigma_{xz}(\gamma)/\gamma$ and $G_T(\gamma) = \partial \sigma_{xz}(\gamma) / \partial \gamma$.

The object of all multiscale theories which seek to connect the molecular and bulk length scales is to rederive the elastic free energy density in terms of molecular properties and architecture. Note that, for notational convenience, we will always consider simple shear deformations (Equation (2.27)) in what follows. Formally, $f(\gamma)$ is readily obtained from statistical mechanics. The free energy of a network composed of many chains may be written in terms of a spatial average of single molecule properties:

$$f_{\text{el}}(\gamma) = \frac{1}{V} \sum_{i=1}^N f_{1,i}(\mathbf{r}_i^0, \{\mathbf{r}_{ij}^\times\}, \mathbf{r}; \gamma) \xrightarrow{N \rightarrow \infty} \rho_N \langle f_1(\mathbf{r}^0, \{\mathbf{r}_j^\times\}, \mathbf{r}; \gamma) \rangle, \quad (2.28)$$

where V is the volume of the material under consideration, ρ_N is the number density of chains, and $f_1(\mathbf{r}^0, \{\mathbf{r}_j^\times\}, \mathbf{r}; \gamma)$ is the single-chain free energy as

a function of the chain's initial position \mathbf{r}^0 , the positions of any cross-linkers along its contour $\{\mathbf{r}_j^\times\}$, its original end-to-end vector \mathbf{r} and the applied shear strain γ . To keep things manageable in this chapter, we restrict ourselves to systems where this full function may be approximated by a free energy $f_1(\mathbf{r}; \gamma)$, a function of the initial end-to-end length and the strain only. This we may compute as the work done to stretch the single chain from a reference position \mathbf{x}_0 (generally, the equilibrium position although in the case of rubber elasticity it is not) to a deformed position $\mathbf{x}(\gamma)$:

$$f_1(\mathbf{x}(\gamma)) = \int_P d\mathbf{q} \cdot \langle \varphi_1 \rangle (\mathbf{q}), \quad (2.29)$$

with P any path from \mathbf{x}_0 to $\mathbf{x}(\gamma)$. $\langle \varphi_1 \rangle (\mathbf{q})$ is the single polymer force-extension curve from Section 2.1. You may note that this is, actually, the first example of a coarse graining step: we are replacing the full, fluctuating single-chain behavior by that of a (nonlinear) spring with a force-extension curve identical to that of the polymer. In doing so, we average over (or *integrate out*) the configurational degrees of freedom along the single chains to compute a bulk free energy density:

$$f_{\text{el}}(\gamma) = \rho_N \int_{\mathbb{R}^3} d\mathbf{r} \mathcal{P}_1(\mathbf{r}) f_1(\mathbf{R}(\mathbf{r}; \gamma)), \quad (2.30)$$

with $\mathcal{P}_1(\mathbf{r})$ being the end-to-end distance probability distribution of a single polymer. This expression for $f(\gamma)_{\text{el}}$ does not yet assume anything regarding the magnitude of the strain, the symmetries of the material, or the linearity of the filament force-extension behavior. What it does neglect, however, is persistence through cross-linkers. It is instructive to see how various limiting behaviors may be extracted from it. To this end, we extend the definition of the Cauchy deformation tensor to include spatial variations, writing $\mathbf{R}(\mathbf{r}; \gamma)_i = \Lambda_{ij}(\mathbf{r}; \gamma)r_j$. The new tensor $\Lambda(\mathbf{r}; \gamma)$ may be called the *local* Cauchy deformation tensor. We are now ready to discuss three key questions that determine how to actually compute the integral for a given system.

- Is the system **affine**? It is if $\Lambda(\mathbf{r}; \gamma) = \Lambda_B(\gamma)$: the *local* Cauchy deformation tensor is everywhere equal to the bulk deformation tensor. The deformation inside the material exactly tracks that of the boundary. If not, then it is **non-affine**.
- Is the system **mechanical**? It is if $f_1(\mathbf{R}(\mathbf{r}; \gamma)) = \varepsilon_1(\mathbf{R}(\mathbf{r}; \gamma))$, with ε_1 the energy density rather than the free energy density. If not, then it is **thermal** (and one needs to consider entropic effects).
- Is the system **isotropic**? It is if $\mathcal{P}_1(\mathbf{r}) = \mathcal{P}_1(|\mathbf{r}|)$. If not, then it is an **anisotropic/ordered system** and we need to consider more than two independent moduli.

Let us consider some examples. Historically, the most important example is the theory of rubber elasticity. Essentially, this is an **affine, thermal and isotropic** model for the elastic response of a system of identical Gaussian (ideal) chains. We evaluate the single-chain free energy, which for lack of internal energy is simply $-TS$, S being the entropy:

$$\langle f_1(\mathbf{r}; \gamma) \rangle_{\mathbf{r}} = -T \int_{\mathbb{R}^3} d\mathbf{r} \mathcal{P}_1(\mathbf{r}) \mathcal{S}_1(\Lambda_B(\gamma) \cdot \mathbf{r}). \quad (2.31)$$

Using the expressions for the probability distribution and the entropy of ideal chains, it is now completely straightforward to compute the free energy change incurred upon shearing from $\gamma = 0$ to a finite γ :

$$\Delta f_{\text{el}}(\gamma) = f_{\text{el}}(\gamma) - f_{\text{el}}(\gamma = 0) = \frac{1}{2}(\rho_N k_B T) \gamma^2, \quad (2.32)$$

from which we immediately read off that the shear modulus, in rubber elasticity, is

$$G = \rho_N k_B T = \left(\frac{\rho}{\lambda \ell_0} \right) k_B T \sim \frac{k_B T}{\ell_0^3}. \quad (2.33)$$

In this last step, we express the result in more accessible quantities - ρ the mass density, λ the linear mass density of the polymer and ℓ_0 the typical length between cross-linkers. They are related via $\rho_N = \frac{\rho}{\lambda \ell_0}$. This result shows the *soft* nature of biopolymer materials: The typical energy per typical volume (ℓ_0^3) is $k_B T$ - much smaller than the ~ 10 eV per (lattice constant)³ in crystalline materials. As a second example, let's consider now a network of ordinary, Hookean springs, each of which has length ℓ_0 . The energy for such a spring is simply $\varepsilon = \frac{1}{2}k(\ell - \ell_0)^2$, with k the spring constant. This system is an example of an **affine, mechanical and isotropic** model. Each of the identical springs has rest length ℓ_0 , and the initial orientations are uniformly distributed. Working out Equation (2.30) now yields

$$f_{\text{el}}(\gamma) = \frac{\rho_N}{4\pi \ell_0^2} \int_0^\infty r^2 dr \int_0^\pi \sin \theta d\theta \int_0^{2\pi} d\phi \left[\frac{1}{2}k(|\Lambda_B \cdot \mathbf{r}| - \ell_0)^2 \delta(r - \ell_0) \right]. \quad (2.34)$$

In general, this needs to be evaluated numerically but for small γ , we can compute the integral exactly:

$$f_{\text{el}}(\gamma) \approx \frac{1}{2} \left(\frac{1}{15} \rho_N k \ell_0^2 \right) \gamma^2. \quad (2.35)$$

From which we read off, again, the small-strain shear modulus

$$G_0 = \frac{1}{15} \rho_N k \ell_0^2 = \frac{1}{15} \left(\frac{\rho}{\lambda} \right) k \ell_0. \quad (2.36)$$

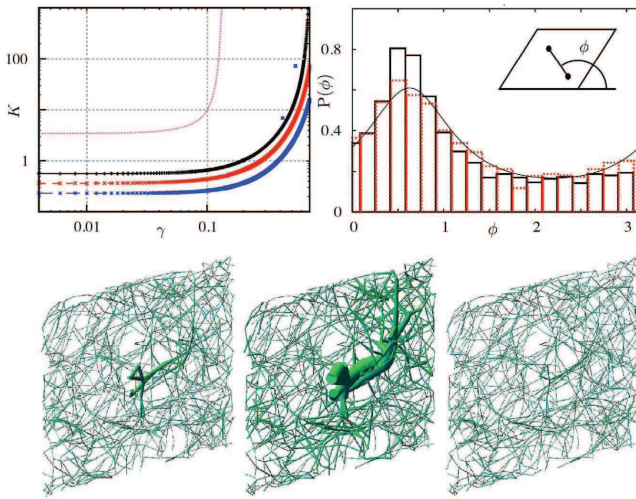


Figure 2.3: (Source: Ref. [35].) Non-affinity reveals itself in various forms. (*Upper left*) A plot of the shear modulus K against shear strain γ of a non-affine network model. The typical nonlinear stiffening response is both delayed and attenuated in non-affine materials. Note, too, that even the linear modulus (modulus at the lowest shear strains) is affected by the non-affinity. (*Upper right*) a histogram of the orientation (measured by ϕ in radians) of inter-cross-linking filaments at the shear strain described by the inset. Non affine deformations allow the material to order in response to strain. Locking in this order may be an important patterning mechanism. (*Lower panel*) Non-affinity occurs in burst-like events that closely resemble the coherently moving regions in glassy materials. Shown from left to right are images of the network at three consecutive shear angles. The thickness of the filaments indicates the magnitude of the local strain – clearly, the strain field is highly heterogeneous.

This result also allows us to connect to the affine, linear theory of semi-flexible filaments: as we have seen,

$$\ell_{\text{eq}} = \ell_c \left(1 - \frac{\ell_c}{6\ell_p} \right). \quad (2.37)$$

We identify this equilibrium length with the ℓ_0 of the Hookean springs. The spring constant must be interpreted as the initial slope of the semi-flexible force-extension curve Equation ((2.19)), from which we compute the appropriate linear spring constant. This immediately yields the correct result for the G_0 of a network of semi-flexible worm like chains

$$G_0 = 6 \left(\frac{\rho}{\lambda} \right) k_B T \left(\frac{\ell_p^2}{\ell_c^3} \right). \quad (2.38)$$

Although we compute here only the linear moduli, the integral is straightforwardly evaluated for arbitrary shear strains γ . In [34] it is demonstrated how the universality of the force-extension curve translates into universal nonlinear behavior of the modulus. Figure 2.3 (upper left panel) shows the predictions from this affine, thermal, isotropic theory of networks of semi-flexible filaments.

The extension of the modeling to anisotropic materials is straightforward. At the level of Equation (2.30), these simply amount to a non-radially symmetric initial distribution $\mathcal{P}_1(\mathbf{r})$. Some care must, however, be taken when interpreting the results in terms of a shear modulus, as systems lacking isotropy possess more than two independent elastic coefficients - the exact amount depending on the number of remaining symmetries.

A far more challenging extension of the modeling is to include non-affinity. For such systems, the local Cauchy strain tensor does vary from place to place. That it is, ultimately, very important however is borne out by Figure 2.3, which shows three important aspects of non-affinity from numerical simulations by Huisman et al. [35]: (1) non-affinity can *order* filamentous networks, (2) non-affinity can *soften* semi-flexible networks, and (3) non-affinity can take the form of a highly *localized*, coherent deformation mode.

The above really only scratches the surface of the mechanical properties of hierarchical biomaterials. Even for far more complicated structures, such as collagen fibril meshworks or ordered composites like the blood vessel wall, the general philosophy remains the same. First, identify the key physical design features of the individual filaments. Then, at the aggregate level, integrate out the intrafilament degrees of freedom, and take the architecture into account via the orientational distribution function. Non-affinity must be accounted for by a spatially varying deformation tensor, which contributes to the elasticity right from the very beginning [36, 37, 38]. In this thesis, we adopt a simulational point of view, and apply it to the actual structure of the collagen fibril. In our simulations, the geometry is highly anisotropic but known and may serve as a starting point. Likewise, the bare mechanical response of the constituent filaments is known. Finally, the TRACTRIX algorithm that we shall present in Chapter 4 allows for a full, non-affine treatment of the fluctuations and deformational behavior. As such, we work towards a complete and microscopically faithful representation of the load-bearing elements of the collagen fibril. In order, however, to connect this to bulk mechanical properties as outlined above we cannot simply shear a periodic volume, because the fibril is a finite entity. Instead, what we will do is to subject the filament to a tip load, and interpret the bent shapes in terms of continuum beam theory. In what follows, we set forth the required theory as it applies to this particular loading configuration.

2.3 Continuum Elasticity Theory of Beams

The theory of continuum elasticity provides a very powerful mathematical framework for describing the strength of materials. Therefore, it is convenient to seek a means of fitting our work within this framework. Moreover, many laboratory experiments report the strength of collagen in terms of elastic moduli, which are defined within the framework of linear elasticity theory. Hence, to be able to discuss results of collagen fibril mechanics from our simulations (which are of microscopic origin), we compare the deformation profile of the fibril to a tip-loaded Timoshenko beam in a cantilever setup (which is a result from continuum elasticity theory). The essentials of Timoshenko beam theory are therefore discussed in the following

2.4 Elements of Continuum Elasticity Theory

This section gives a brief overview of the formulation of continuum elasticity theory, also called nonlinear elasticity theory.

In essence, continuum elasticity theory models any solid material as a continuum of material coordinates¹ $\mathbf{r}(t)$ occupying a region of space, and over which a strain tensor field $\varepsilon(\mathbf{r}(t))$ (which can be integrated to give the finite displacements of the material coordinates, and satisfies compatibility conditions²) and a (Cauchy) stress tensor field $\boldsymbol{\sigma}(\mathbf{r}(t))$ (which describes forces per unit area in the bulk and on the boundary of the solid, and furthermore obeys Newton's laws) are defined. This picture of materials of course breaks down as one zooms in, all the way down to the molecular length scales, so that structure begins to emerge, and the discreteness of the material becomes more apparent. At this point, a microscopic dynamic or statistical approach incorporating the behaviour of the molecular constituents of the solid is better suited for its mechanical description, as exemplified by the present work.

¹Recently, it has been suggested that for some types of solid, such as bone and nematic elastomers, material coordinates alone are not sufficient for a complete description of their mechanics, but that an additional field with 3 degrees of freedom (related to the average orientation of each generally biaxial mesogen, which need not coincide with the local rotation of the material coordinate volume element at the same point of material) needs to be included. This inclusion gives rise to a new theory of elasticity known as Cosserat Elasticity, in which the stress tensor is not necessarily symmetric. A description of this theory is however beyond the scope of the present work.

²The vector displacement field of the material coordinates is determined from the integration of the components of the strain tensor field. This is an overdetermined system of equations, since the number of independent strain tensor components is larger than the number of components of the displacement field. Thus to ensure that the displacement field is single-valued and continuous (as required by a simply-connected material that must not develop gaps nor overlaps during deformation) it becomes necessary to impose certain conditions on $\varepsilon(\mathbf{r}(t))$. These conditions are known as the *compatibility conditions*.

Continuum elasticity appears to have birthed two branches, namely linear elasticity (which assumes infinitesimal strains) and nonlinear elasticity (or finite strain elasticity). The latter is actually a generalization of the former, since the assumption of infinitesimal strains enables the linearization of the more general finite strain elasticity theory.

The two tensor fields of stress and strain are not independent of each other. Indeed a constitutive law that relates them to each other needs to be provided, usually by phenomenological means (incorporating the symmetries of the material), or more completely, by considerations of the molecular constituents of the solid and the energies of interaction between them. (See Section 2.2 for the example of rubber elasticity.) And this is how a bridge may be formed between continuum elasticity theory and statistical mechanics.

The constitutive law, together with Newton's laws (or the variational principle) and the compatibility conditions form a set of equations that enable the prediction of the mechanical response of any solid material in an arbitrary shape and under any given boundary conditions. Usually a numerical scheme, namely the finite element method, is used to solve these equations. But in a few simple cases, such as for an elastic rod, more easily accessible methods may be employed, as demonstrated in the following section.

2.5 Elastic Beam Bending Theories

To predict the bending response of a solid in the shape of a slender and initially straight elastic beam, elastic beam theories exploit its one-dimensional nature and axial symmetry to reduce the equations of elasticity theory to a much more simplified form involving only the axial deflection, and the force and moment distributions along the axis of the rod.

The Euler-Bernoulli beam theory assumes that the beam is bent without extension of the beam axis. Moreover, all cross-sections of the rod are assumed to remain planar and also to tilt in such a way that they are always normal to the bent axis.

Timoshenko beam theory improves on the Euler-Bernoulli theory by including the effect of shear in the beam equations, meaning that the cross-sections, though they remain planar, may develop a non-perpendicular tilt to the bent axis [39]. Furthermore, there exist Timoshenko beam theories which allow the axis of the beam to develop an extension or compression in addition to bending [40, 41]. We employ the latter theory to predict the shear and Young's moduli of a collagen fibril.

2.6 Extensible Timoshenko Beam Theory

Many authors [40, 41, 42, 43] in the literature present slightly different derivations of Timoshenko beam theory that lead to the same result. In this section, we follow the analysis due to Irschik *et al.* [43] because it shows how the mechanical balance equations of the beam follow from nonlinear elasticity theory and the virtual work principle.

Kinematics

A beam is a solid body occupying a certain region of three-dimensional space, where one dimension of this region, the axial length of the beam, is much larger than the other two dimensions, which are called cross-sectional dimensions. We make use of the material or Lagrangian description of continuum mechanics, in which the straight undeformed configuration is taken as the reference configuration. We assume that the deformation is plane, that is, the beam axis in the deformed and in the reference configurations are situated in a common plane, and that no twist of the cross-sections about the beam axes takes place.

We note the following definitions:

- \mathbf{r} – the position vector,
- \mathbf{F} – the deformation gradient (which is the same as Λ used for networks in the preceding sections),
- J – the Jacobian determinant of the deformation gradient,
- \mathbf{G} – the Green strain (whose components are the same as u_{ij} used for networks in the preceding sections)

We choose a common Cartesian x - y - z coordinate system to describe the beam deformation, see Figure 2.4 [43].

This common Cartesian frame is fixed in the reference configuration, and it is oriented such that x represents the coordinate of the beam-axis in the reference configuration. The y axis is selected such that the deformed axis remains situated in the x - z plane. Plane cross-sections of the beam in the reference configuration therefore are spanned by the unit vectors $\hat{\mathbf{y}}$ and $\hat{\mathbf{z}}$. The position vector of a particle, which was located at the point $x\hat{\mathbf{x}} + y\hat{\mathbf{y}} + z\hat{\mathbf{z}}$ in the reference configuration, having the transverse distance $|z|$ and out-of-plane distance $|y|$ away from the straight reference axis, in the deformed configuration can be written in the following form:

$$\mathbf{r}(x, y, z) = \mathbf{r}_0(x) + y\hat{\mathbf{y}} + z\hat{\boldsymbol{\zeta}}(x). \quad (2.39)$$

The position vector of an axis point in the deformed configuration is denoted by \mathbf{r}_0 (see Figure 2.4).

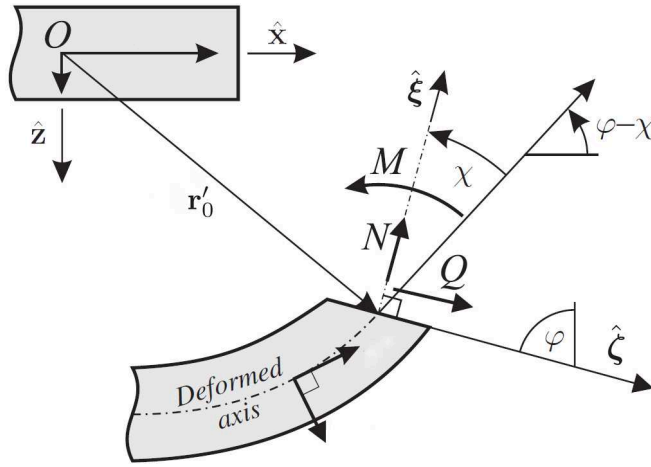


Figure 2.4: (Top left) Section of the undeformed Timoshenko beam lying along the x -axis. (Bottom) The same section of the now deformed Timoshenko beam in the zx -plane where bending occurs. M refers to the bending moment, N the normal force, and Q the shear force exerted at a cross-section of the beam. The cross-section is tilted at angle χ to the deformed axis, while φ is the angle the cross-section make with the vertical (z -axis).

Equation (2.39) reveals the Timoshenko assumption, namely that the deformed cross-section is assumed to remain plane and undistorted in comparison to the reference configuration. The cross-section in the deformed configuration is spanned by the unit vectors \hat{y} and $\hat{\zeta}$, the latter vector being situated in the x - z plane (see also Figure 2.4).

Thus the three-dimensional problem can be reduced to finding the displacement field \mathbf{u}_0 of the beam axis, and the orientation field $\hat{\zeta}$ of planar cross-sections along the beam axis. We define the displacement field as

$$\mathbf{u}_0(x) = \mathbf{r}_0(x) - x\hat{\mathbf{x}} = u(x)\hat{\mathbf{x}} + w(x)\hat{\mathbf{z}}. \quad (2.40)$$

The components u and w are referred to as axial displacement and deflection, respectively.

Now the deformation gradient tensor can be obtained by partial spatial differentiation of Equation (2.39) with respect to the reference coordinates, noting that the common Cartesian frame is fixed in the reference configuration:

$$\mathbf{F} = \nabla \mathbf{r} \quad (2.41)$$

$$= \mathbf{r}' \otimes \hat{\mathbf{x}} + \hat{\mathbf{y}} \otimes \hat{\mathbf{y}} + \hat{\zeta} \otimes \hat{\mathbf{z}} \quad (2.42)$$

$$= (\mathbf{r}'_0 + z\hat{\zeta}') \otimes \hat{\mathbf{x}} + \hat{\mathbf{y}} \otimes \hat{\mathbf{y}} + \hat{\zeta} \otimes \hat{\mathbf{z}}, \quad (2.43)$$

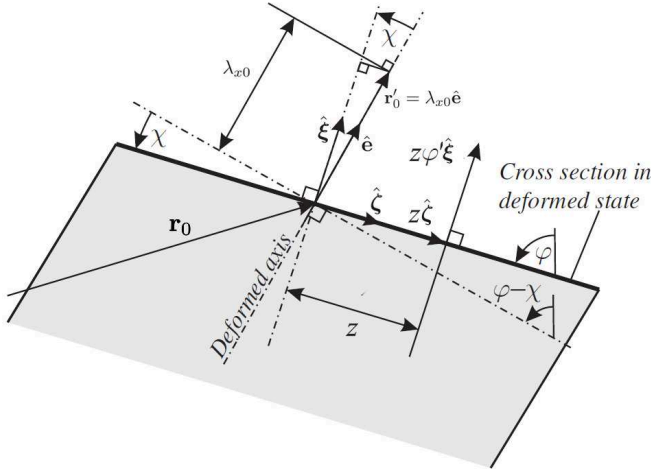


Figure 2.5: A section of the deformed Timoshenko beam in the zx -plane where bending occurs showing the quantities that describe the strain in the beam. We denote $\mathbf{r}'_0 + z\hat{\zeta}'$ and $\hat{\zeta}$ as deformation gradient vectors, representing the mapping of $\hat{\mathbf{x}}$ and $\hat{\mathbf{z}}$ via \mathbf{F} onto the deformed plane, for example, $\mathbf{F} \cdot \hat{\mathbf{x}} = (\mathbf{r}'_0 + z\hat{\zeta}')$. The principal stretch of the element of the beam axis, that is, the ratio of the length of a differential axis element in the deformed and in the undeformed configuration, is denoted by λ_{x0} (that is, $\mathbf{r}'_0 = \lambda_{x0}\hat{\mathbf{e}}$).

where the prime denotes the derivative with respect to the axial coordinate x , and the symbol \otimes stands for the dyadic vector product. We denote $\mathbf{r}'_0 + z\hat{\zeta}'$ and $\hat{\zeta}$ as deformation gradient vectors, representing the mapping of $\hat{\mathbf{x}}$ and $\hat{\mathbf{z}}$ via \mathbf{F} onto the deformed plane, for example, $\mathbf{F} \cdot \hat{\mathbf{x}} = (\mathbf{r}'_0 + z\hat{\zeta}')$.

To obtain a suitable kinematic description for the entity $\hat{\zeta}$, we denote the angle, by which a reference cross-section with axial coordinate x is rotated about the y axis into the deformed configuration, as $\varphi(x)$. Hence, we may write

$$\hat{\zeta} = \sin \varphi \hat{\mathbf{x}} + \cos \varphi \hat{\mathbf{z}}, \quad (2.44)$$

from which it follows that

$$\hat{\zeta}' = \varphi' (\cos \varphi \hat{\mathbf{x}} - \sin \varphi \hat{\mathbf{z}}). \quad (2.45)$$

Since $\hat{\zeta}$ is a unit vector, $\hat{\zeta}'$ is perpendicular to $\hat{\zeta}$, and we shall denote the unit vector normal to $\hat{\zeta}$ as

$$\hat{\xi} = \cos \varphi \hat{\mathbf{x}} - \sin \varphi \hat{\mathbf{z}}. \quad (2.46)$$

For further reference, we note that the unit vector $\hat{\mathbf{x}}$ is rotated by φ into the unit vector $\hat{\xi}$ (see Figures 2.4 and 2.5). The deformation gradient in Equation (2.41)

now becomes

$$\mathbf{F} = (\mathbf{r}'_0 \cdot \hat{\mathbf{x}} + z\varphi' \cos \varphi) \hat{\mathbf{x}} \otimes \hat{\mathbf{x}} + \sin \varphi \hat{\mathbf{x}} \otimes \hat{\mathbf{z}} \quad (2.47)$$

$$+ \hat{\mathbf{y}} \otimes \hat{\mathbf{y}} \quad (2.48)$$

$$+ (\mathbf{r}'_0 \cdot \hat{\mathbf{z}} - z\varphi' \sin \varphi) \hat{\mathbf{z}} \otimes \hat{\mathbf{x}} + \cos \varphi \hat{\mathbf{z}} \otimes \hat{\mathbf{z}}, \quad (2.49)$$

where we have projected \mathbf{r}'_0 , which is tangent to the deformed axis, onto the fixed x and z directions to obtain a formulation which can be directly assigned with a matrix in the common frame. A suitable kinematic description can be obtained for the latter projections by noting that \mathbf{r}'_0 in general will not be perpendicular to the deformed cross-section, and hence will not be perpendicular to the vector $\hat{\boldsymbol{\zeta}}$, because the tangent to the deformed axis generally encloses the shear angle χ with the normal to the cross-section in the deformed configuration (see Figures 2.4 and 2.5). Had the unit vector $\hat{\boldsymbol{\zeta}}$ been perpendicular to the deformed axis, such that no shear deformation were present, then one would have had $\chi = 0$, which is commonly denoted as the Euler-Bernoulli assumption. In the following, however, we study the Timoshenko case of generally non-vanishing shear angles χ . The angle to the tangent of the deformed axis, and hence to \mathbf{r}'_0 , measured from the x direction about the y -axis, is given by $(\varphi - \chi)$. We denote the unit vector in the direction of \mathbf{r}'_0 by $\hat{\mathbf{e}}$ (see Figure 2.5), such that we can write

$$\mathbf{r}'_0 = \lambda_{x0} \hat{\mathbf{e}}, \quad \lambda_{x0} = \|\mathbf{r}'_0\| = \sqrt{(1 + u')^2 + w'^2}. \quad (2.50)$$

Therefore,

$$u' = \lambda_{x0} \cos(\varphi - \chi) - 1, \quad (2.51)$$

$$w' = \lambda_{x0} \sin(\varphi - \chi). \quad (2.52)$$

The principal stretch of an element of the beam axis, that is, the ratio of the length of a differential axis element in the deformed and in the undeformed configuration, is denoted by λ_{x0} . The projections of \mathbf{r}'_0 in Equation (2.47) now become (see Figure 2.5):

$$\mathbf{r}'_0 \cdot \hat{\mathbf{x}} = \lambda_{x0} \cos(\varphi - \chi), \quad (2.53)$$

$$\mathbf{r}'_0 \cdot \hat{\mathbf{z}} = -\lambda_{x0} \sin(\varphi - \chi). \quad (2.54)$$

From this, we obtain the following matrix representation for \mathbf{F} in the common frame

$$\mathbf{F} = \begin{pmatrix} \lambda_{x0} \cos(\varphi - \chi) + z\varphi' \cos \varphi & 0 & \sin \varphi, \\ 0 & 1 & 0 \\ -[\lambda_{x0} \sin(\varphi - \chi) + z\varphi' \sin \varphi] & 0 & \cos \varphi \end{pmatrix}. \quad (2.55)$$

The Jacobian determinant J of \mathbf{F} in the framework of the Timoshenko assumption follows to

$$J = \lambda_{x0} \cos \chi + z\varphi'. \quad (2.56)$$

The symmetric right Cauchy-Green tensor is generally defined as

$$\mathbf{C} = \mathbf{F}^T \mathbf{F}. \quad (2.57)$$

Within the Timoshenko assumption it has the matrix representation

$$\mathbf{C} = \begin{pmatrix} \lambda_{x0}^2 + 2z\varphi'\lambda_{x0}\cos\chi + (z\varphi')^2 & 0 & \lambda_{x0}\sin\chi \\ 0 & 1 & 0 \\ \lambda_{x0}\sin\chi & 0 & 1 \end{pmatrix}. \quad (2.58)$$

The Green strain tensor, which has the general definition,

$$\mathbf{G} = \frac{1}{2}(\mathbf{C} - \mathbf{1}_3) \quad (2.59)$$

is thus found to have a matrix representation that reads

$$\mathbf{G} = \frac{1}{2} \begin{pmatrix} \lambda_{x0}^2 + 2z\varphi'\lambda_{x0}\cos\chi + (z\varphi')^2 - 1 & 0 & \lambda_{x0}\sin\chi \\ 0 & 0 & 0 \\ \lambda_{x0}\sin\chi & 0 & 0 \end{pmatrix}. \quad (2.60)$$

Note that \mathbf{G} in Equation (2.60) indeed reflects the Timoshenko kinematic assumption, in the framework of which only axial strains G_{xx} and shear strains $G_{zx} = G_{xz}$ should be present.

We are now in the position to relate the above continuum mechanics-based results to the generalized strains that are fundamental in Reissner's structural mechanics formulation [40]. Reissner introduced a bending strain as

$$\kappa = \varphi' \quad (2.61)$$

and generalized normal and shear strains in the form

$$\varepsilon = \lambda_{x0}\cos\chi - 1, \quad (2.62)$$

$$\gamma = \lambda_{x0}\sin\chi. \quad (2.63)$$

So that, from Equations (2.51)-(2.52),

$$u' = (1 + \varepsilon)\cos\varphi + \gamma\sin\varphi - 1, \quad (2.64)$$

$$w' = (1 + \varepsilon)\sin\varphi - \gamma\cos\varphi. \quad (2.65)$$

It is to be emphasized that the expressions for J , \mathbf{C} and \mathbf{G} given in Equations (2.56), (2.58) and (2.60) can be completely expressed by the generalized strains presented in Equations (2.61)-(2.63) and the transverse coordinate z . This shows that Reissner's generalized strains are proper strain measures also in the sense of continuum mechanics, because J , \mathbf{C} and \mathbf{G} are known to be material frame indifferent deformation measures, for which the components of proper matrix representations must not change when the reference or the

deformed configurations are subjected to rigid body rotations. In this case, this becomes evident when kinematically interpreting the term $\lambda_{x0} \cos \chi$ as projection of the axial stretch to the direction of $\hat{\xi}$ normal to the deformed cross-section, and the term $\lambda_{x0} \sin \chi$ as projection onto the deformed cross-section, in the direction of $\hat{\xi}$. Moreover, the expression φ' represents a proper curvature measure, known from the geometric analysis of curves. The kinematic entities in Equations (2.61)-(2.63), which describe the deformation of the actual configuration with respect to the reference configuration only, of course, do not change when the rigid body rotations of the respective configurations are superimposed. Note also that the cross-sectional coordinates y and z are not stretched in the framework of the Timoshenko assumption³.

2.7 Internal Forces and Moments

The application of the principle of virtual work is basic for Reissner's structural mechanics theory presented in [40], in which he postulated a particular simple expression for the virtual work of the internal forces per unit length of the undeformed axis as

$$\delta W_{\text{int}} = N \delta \varepsilon + Q \delta y + M \delta \kappa, \quad (2.66)$$

where generalized static entities were introduced as normal force N , shear force Q and bending moment M on a cross-section of the beam (see Figure 2.4). Reissner denoted these generalized static entities as stress resultants; the exact relations to stress definitions from continuum mechanics, however, were not addressed. In Equation (2.66) and in the following equations, δ denotes a variation, that is, a virtual change in deformation. In this section, we show that when using the above Timoshenko-type expressions for the Green strain, Equation (2.60), and defining the generalized static entities properly, the virtual work expression, which is known to be generally valid for the material description of continuum mechanics, does exactly lead to Reissner's structural mechanics postulate for the virtual work (Equation (2.66)). We introduce the symmetric second Piola-Kirchhoff stress S^4 by writing its matrix representation in the common frame as follows:

$$\mathbf{S} = \begin{pmatrix} S_{xx} & S_{yx} & S_{zx} \\ S_{xy} & S_{yy} & S_{zy} \\ S_{zx} & S_{yz} & S_{zz} \end{pmatrix}. \quad (2.67)$$

The virtual work of S done upon a virtual change of the Green strain \mathbf{G} is known to define the virtual work of the internal forces in the framework of the

³This assumption is corrected later in Section 2.9 by the introduction of a so-called shear coefficient k which depends on the Poisson ratio ν of the material from which the beam is made.

⁴ \mathbf{S} is related to the Cauchy stress σ_{ij} of Equation (2.22) by: $\sigma_{ij} = \frac{1}{J} \mathbf{F} \cdot \mathbf{S} \cdot \mathbf{F}^T$.

material description of continuum mechanics in the form:

$$\delta W_{\text{int}} = \int_A dA \mathbf{S} \cdot \delta \mathbf{G}, \quad (2.68)$$

where the dot indicates the scalar or double-contracted tensor product, and the integration is to be performed over the cross-sectional area A in the reference configuration. Using the Timoshenko-type matrix representation for \mathbf{F} in Equation (2.60), and noting that \mathbf{S} in Equation (2.67) is symmetric, $S_{zx} = S_{zx}$, we obtain

$$\delta W_{\text{int}} = \int_A dA \left(S_{xx} \frac{1}{2} \delta(\lambda_{x0}^2 + 2z\varphi' \lambda_{x0} \cos \chi + (z\varphi')^2 - 1) + S_{zx} \delta(\lambda_{x0} \sin \chi) \right). \quad (2.69)$$

Motivated by the fact that Equations (2.61)- (2.63) yield the variations,

$$\delta \kappa = \delta(\varphi'), \quad (2.70)$$

$$\delta \varepsilon = \delta \lambda_{x0} \cos \chi - \delta \chi \lambda_{x0} \sin \chi, \quad (2.71)$$

$$\delta \gamma = \delta \lambda_{x0} \sin \chi + \delta \chi \lambda_{x0} \cos \chi, \quad (2.72)$$

the virtual work expression in Equation (2.69) is identically expanded into the form

$$\delta W_{\text{int}} = \int_A dA [S_{xx}(\lambda_{x0} \cos \chi + z\varphi')(\delta \lambda_{x0} \cos \chi - \delta \chi \lambda_{x0} \sin \chi) \quad (2.73)$$

$$+ (S_{xx} \lambda_{x0} \sin \chi + S_{zx})(\delta \lambda_{x0} \sin \chi + \delta \chi \lambda_{x0} \cos \chi) \quad (2.74)$$

$$+ S_{xx} z(\lambda_{x0} \cos \chi + z\varphi') \delta \varphi']. \quad (2.75)$$

Hence, defining the generalized static entities as

$$N = \int_A dA S_{xx} (\lambda_{x0} \cos \chi + z\varphi') = \int_A dA S_{xx} J \quad (2.76)$$

$$Q = \int_A dA (S_{xx} \lambda_{x0} \sin \chi + S_{zx}) = \int_A dA (S_{xx} \gamma + S_{zx}) \quad (2.77)$$

$$M = \int_A dA S_{xx} z(\lambda_{x0} \cos \chi + z\varphi') = \int_A dA J z \quad (2.78)$$

it follows that the continuum mechanics expression for the virtual work, Equation (2.68), in the framework of the Timoshenko assumption indeed yields Reissner's relation, Equation (2.66). As is seen from Equations (2.76)-(2.78), the static entities N , Q and M represent generalized stress resultants. The second Piola-Kirchhoff stress tensor is generally considered as a proper stress measure to be related to the Green strain tensor in the form of constitutive stress-strain relations, see below. A further continuum mechanics-based justification of Equations (2.76)-(2.78) nevertheless seems to be necessary. The

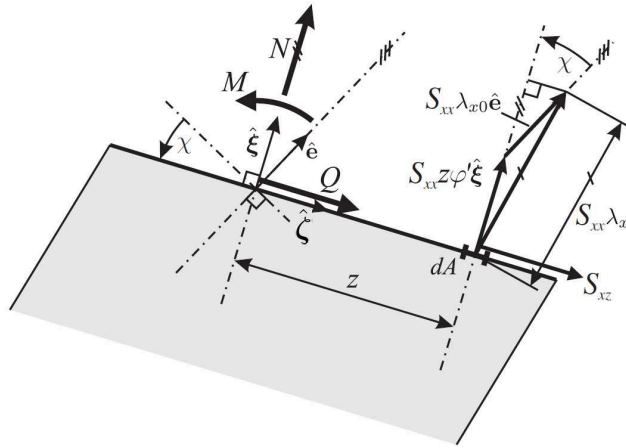


Figure 2.6: Graphical interpretation of the second Piola-Kirchhoff stress components S_{xx} and S_{zx} .

following arguments rest upon the sketch given in Figure 2.6. As is well known, the Lagrangian stress vector, which is taken per unit area in the undeformed state, is to be decomposed with respect to the generally non-orthogonal and non-unit deformation gradient vectors, see, for example, Ziegler and Washizu. For the Timoshenko case, these deformation gradient vectors are represented by $\mathbf{r}'_0 + z\varphi'\hat{\xi}$ and $\hat{\zeta}$. The corresponding skew stress components are formed by the second Piola-Kirchhoff stresses S_{xx} and S_{zx} , respectively, see Figure 2.6. Projecting onto the directions of $\hat{\xi}$ and $\hat{\zeta}$, and forming the resulting force components by integration over the undeformed cross-sectional area, yields Equations (2.76) and (2.77). That the continuum mechanics expression for the virtual work, Equation (2.68), in the framework of the Timoshenko assumption, yields Reissner's structural mechanics relation, Equation (2.66), proves that the definitions for the generalized static entities given in Equations (2.76)-(2.78) are consistent with the local structural mechanics relations of beam equilibrium that were stated by Reissner. Moreover, we now have at our disposal relations between the static entities N , Q and M and components of the second Piola-Kirchhoff stress tensor \mathbf{S} , which can be used to consistently introduce constitutive models at the stress-strain level of continuum mechanics into the boundary value problems for the generalized static entities and the generalized strains that were stated by Reissner.

2.8 Mechanical Balance Equations

According to the principle of virtual work, the virtual work of the internal forces δW_{int} is balanced by the virtual work of the external forces δW_{ext} . In the present chapter, only uniformly distributed loads are considered. Let p_x and p_z denote the components of the force vector per unit undeformed length in the horizontal and vertical direction, $\mathbf{p} = p_x \hat{\mathbf{x}} + p_z \hat{\mathbf{z}}$, then the virtual work of the external forces is given by

$$\delta W_{\text{ext}} = \int_L dx \mathbf{p} \cdot \delta \mathbf{u}_0 = \int_L dx (p_x \delta u + p_z \delta w), \quad (2.79)$$

where the integral is over the length L of the beam. Consequently, the principle of virtual work reads

$$\delta W_{\text{int}} - \delta W_{\text{ext}} = \int_L dx (N \delta \varepsilon + Q \delta \gamma + M \delta \kappa - p_x \delta u - p_z \delta w) = 0. \quad (2.80)$$

Analogously to Reissner [40], the local form of the mechanical balance equations and the corresponding boundary conditions are obtained from the variational formulation Equation (2.80) by substituting the virtual changes of the generalized strains $\delta \varepsilon$, $\delta \gamma$ and $\delta \kappa$ [expressed as linear combinations of $\delta(u')$, $\delta(w')$, and $\delta(\varphi')$] and subsequently integrating by parts. Then after using standard arguments, the balance equations are deduced as

$$(N \cos \varphi - Q \sin \varphi)' + p_x = 0, \quad (2.81)$$

$$(N \sin \varphi + Q \cos \varphi)' + p_z = 0, \quad (2.82)$$

$$M' + (1 + \varepsilon)Q - \gamma N = 0. \quad (2.83)$$

Correspondingly, the boundary conditions for a beam with length L are deduced as

$$u = \text{given} \quad \text{or} \quad \mu(N \cos \varphi - Q \sin \varphi) = f_x, \quad (2.84)$$

$$w = \text{given} \quad \text{or} \quad \mu(N \sin \varphi + Q \cos \varphi) = f_z, \quad (2.85)$$

$$\varphi = \text{given} \quad \text{or} \quad \mu M = c. \quad (2.86)$$

where f_x and f_z are the x - and z -components of the applied concentrated loads at the end; c is the applied concentrated moment there, reckoned to be positive when it is clockwise; μ is defined by

$$\mu = \begin{cases} 1 & \text{at } x = L, \\ -1 & \text{at } x = 0. \end{cases} \quad (2.87)$$

2.9 Constitutive Relations

We assume a perfectly elastic material with no viscous effects whatsoever, and the strains are assumed to be negligibly small when compared with unity. Although constitutive relations have often been discussed in terms of the stress resultants in conjunction with the strain energy, it may be straightforward to specify them in terms of the stress components and their corresponding strain measures. In the linear elastic case, they may be given by

$$S_{xx} = E\varepsilon, \quad S_{zx} = G\gamma, \quad (2.88)$$

where E and G are the elastic moduli. Although substitution of Equation (2.88) into Equations (2.76)-(2.78) results in highly nonlinear expressions, we can linearize these nonlinear constitutive relations using the small-strain assumption, to obtain

$$N \approx EA\varepsilon, \quad (2.89)$$

$$M \approx EI\varphi', \quad \text{and} \quad (2.90)$$

$$Q \approx GkA\gamma, \quad (2.91)$$

where I is the moment of inertia of a cross-section, and the shear coefficient k is introduced in Equation (2.91) to allow for the fact that the shear stress S_{zx} is actually not uniform over the cross-section. Numerous attempts have been made to evaluate k theoretically or experimentally [44, 45, 42], but the general consensus is that for beams of circular cross-section

$$k = \frac{6(1 + \nu)^2}{7 + 12\nu + 4\nu^2}, \quad (2.92)$$

which was first obtained by Timoshenko and is supported by experimental evidence [44]. Here ν is Poisson's ratio.

2.10 Dimensionless Expressions of Field Equations

For clear comparison, all the field equations, Equations (2.64)-(2.65), (2.84)-(2.86), (2.89)-(2.90), can be expressed in terms of the dimensionless quantities

[41] if the beam is uniform in shape and material. Let

$$z_1 = (N \cos \varphi - Q \sin \varphi)L^2/(EI), \quad (2.93)$$

$$z_2 = (N \sin \varphi + Q \cos \varphi)L^2/(EI), \quad (2.94)$$

$$z_3 = ML/(EI), \quad (2.95)$$

$$z_4 = u/L, \quad (2.96)$$

$$z_5 = w/L, \quad (2.97)$$

$$z_6 = \varphi, \quad (2.98)$$

$$y_1 = z_1 \cos z_6 + z_2 \sin z_6, \quad (2.99)$$

$$y_2 = -z_1 \sin z_6 + z_2 \cos z_6, \quad (2.100)$$

$$q_1 = p_x L^3/(EI), \quad (2.101)$$

$$q_2 = p_z L^3/(EI). \quad (2.102)$$

Then the field equations can be written from Equations (2.64)-(2.65), (2.84)-(2.86) as

$$\dot{z}_1 = -q_1, \quad (2.103)$$

$$\dot{z}_2 = -q_2, \quad (2.104)$$

$$\dot{z}_3 = -[1 + \beta^2(1 - \alpha)y_1] y_2, \quad (2.105)$$

$$\dot{z}_4 = (1 + \beta^2 y_1) \cos z_6 - \alpha \beta^2 y_2 \sin z_6 - 1, \quad (2.106)$$

$$\dot{z}_5 = (1 + \beta^2 y_1) \sin z_6 + \alpha \beta^2 y_2 \cos z_6, \quad (2.107)$$

$$\dot{z}_6 = z_3, \quad (2.108)$$

where a superposed dot indicates differentiation with respect to the dimensionless variable (x/L), and

$$\alpha = E/(kG), \quad \beta = \sqrt{I/A}/L. \quad (2.109)$$

Given values for E and G , the solutions of Equations (2.103)-(2.108) are determined numerically using MATLAB[®] routine `bvp4c`⁵. The tolerance for the iterations of this routine is set to 10^{-10} .

By varying the moduli E and G for a beam of specific dimensions and boundary conditions, we can find a displacement field (u, w, φ) which is close to that determined from the simulations of a collagen fibril of the same dimensions and boundary conditions of the beam. The values of E and G that give the closest displacement field (in a least-squares sense) to that of the fibril are taken to be the effective Young's modulus and the effective shear modulus of the collagen fibril. In the next chapter, we outline the simulation of the fibril.

⁵`bvp4c` is a finite difference code that implements the three-stage Lobatto IIIa formula [46]. This is a collocation formula and the collocation polynomial provides a C^1 -continuous solution that is fourth-order accurate uniformly in the domain. Mesh selection and error control are based on the residual of the continuous solution.

2.11 Outlook

This completes our discussion of the multiscale modeling philosophy we adopt, and the specific settings we shall use. We model the basic constituents as discretized worm-like chains, arrange few or many of these constituents into 3D cross-linked architectures, and analyze their collective mechanical response in terms of appropriately chosen continuum models to obtain microstructurally determined effective mechanics. This modeling strategy must now be implemented in a specific computational framework. We have chosen Markov Chain Monte Carlo - a choice that is not without consequences as the potential speed-up it offers is hindered by numerous practical hurdles. In the next two chapters, we address these issues and present our solutions.

CHAPTER 3

COMPUTATIONAL METHODS

In this chapter we discuss computational methods in general, particularly, the Markov Chain Monte Carlo method of simulation. The treatise is background information only. Yet it is not intended to be a complete discussion of all existing methods of simulation, and in fact we touch on only the most common methods, namely the Molecular Dynamics (MD) and Markov Chain Monte Carlo (MCMC) methods, motivating their use, and noting their limitations. We pay more attention to the Metropolis algorithm, which is the traditional implementation of the MCMC method. In the next chapter, we move on to describe specialized moves of the Metropolis algorithm that were invented in this work to simulate cross-linked polymeric systems, and whose acceptance ratios are evaluated by means of expressions presented in this chapter.

3.1 Why not Molecular Dynamics?

Ideally, we want to identify the sources of complex behaviour in the physical systems we encounter in biology by closely following their evolution in time. Mathematically speaking, this means that we want to determine the microstate variables $(\mathbf{r}(t), \mathbf{p}(t))$ of the system as a function of time, where $\mathbf{r}(t)$ denotes the positions, and $\mathbf{p}(t)$ the momenta of the particles that make up the system. Then the properties that we wish to investigate are defined as functions $A(\mathbf{r}(t), \mathbf{p}(t))$ of the microstate variables, and they can also be tracked as the system evolves.

The most desirable approach to determining $(\mathbf{r}(t), \mathbf{p}(t))$ would be to solve analytically the equations of motion of the system, as determined by Newton's laws of motion, or by the Variational Principle (that is, the Lagrangian or Hamiltonian formulation). Unfortunately, in only the simplest systems (for example, two point particles connected by a spring) is it possible to obtain an analytically closed form solution of the complete motion of the system. In particular, when the number of degrees of freedom of the system is very large, the number of equations of motion is correspondingly large, and consequently, the services of a computer program (for example, Mathematica[®]) with the ability to perform symbolic computation are employed for their solution. Still, the non-linearities inherent in all but the simplest inter-particle interactions (for instance, the harmonic interaction), filters down into the equations of motion, thereby making them very difficult to solve.

Another approach, more commonly resorted to, is the use of a modern digital computer to very quickly integrate the equations of motion numerically for a particular set of initial and boundary conditions, and for a suitably chosen discretization of time. This option is the realm of Molecular Dynamics (MD) simulations, which has developed a strong following in the physicist community, and in the past few decades has been very instrumental in simulating biological systems.

If all that was required was to follow the system's trajectory in time, then this would be the end of the story. However, the overwhelming majority of biological systems under study are not isolated from their environment and hence they are often already specified in terms of (and sometimes controlled by) thermodynamic or macroscopic variables such as temperature, pressure, chemical potential, and so on. Thermodynamic variables can only be introduced into the above classical dynamics formalisms (that is, the Newtonian and Variational formulations) in a nontrivial manner.

To address these issues, certain smart *ad hoc* methods have been devised, such as the Berendsen and Nosé-Hoover thermostats that can maintain and control the temperature of the system [47, 48]. Another is the Parrinello-Rahman barostat used to maintain and control the pressure and stresses on the system, which in turn determine size and shape [49]. But a full description of these devices is beyond the scope of the present work.

To see a more natural means (than the aforementioned thermostats and barostats) by which classical dynamics connects with thermodynamics and statistical mechanics, let us now turn our attention to the phase space \mathcal{P} of the physical system at hand. In the course of its evolution, and depending on its energy, the representative point $(\mathbf{r}(t), \mathbf{p}(t))$ may spend more time in some regions of phase space than in others. If one is able to devise a means of counting the frequency with which a system visits any arbitrary region of phase space relative to some other arbitrary region of phase space in a period of time t , then one obtains the so-called phase-space distribution function $\pi_t(\mathbf{r}, \mathbf{p})$ of the system. As the time $t \rightarrow \infty$ the shape of this distribution is expected to approach its asymptotic form $\pi^*(\mathbf{r}, \mathbf{p})$ and remain invariant with time.

Another way of looking at this is to consider not only one system but an asymptotically large number N of identical systems (called an ensemble of systems) all sharing the same boundary conditions, and which at some instant of time are spread over the entire phase space, according to some arbitrarily chosen initial distribution $\pi_0(\mathbf{r}(t), \mathbf{p}(t))$. All the systems in the ensemble are then allowed to evolve, each according to its equations of motion and initial conditions. Note that the only thing that then distinguishes one system from another within the ensemble is its initial condition. Then as each system of the ensemble evolves, this phase space distribution will also evolve in time, albeit according to Liouville's equation for distributions of classical systems.

As time approaches infinity the distribution asymptotically no longer changes with time and a stationary-state (or equilibrium) distribution solution $\pi^*(\mathbf{r}(t), \mathbf{p}(t))$ to Liouville's equation is reached. This stationary state solution can be shown to be, in general, a function of the total energy $\mathcal{E}(\mathbf{r}, \mathbf{p})$ of the system. But its precise shape depends on the thermodynamic variables describing the systems of the ensemble: for the canonical ensemble (in which T is constant), for instance, this stationary state solution turns out to be the Maxwell-Boltzmann equilibrium distribution function $\pi^*(\mathbf{r}(t), \mathbf{p}(t)) = \exp(\mathcal{E}(\mathbf{r}(t), \mathbf{p}(t))/k_{\text{B}}T)$. Hence we establish a link between classical dynamics and statistical mechanics.

It must be noted that these two viewpoints – the single system viewpoint and the ensemble viewpoint – are not equivalent unless a single system beginning at some point in phase space can, given enough time for evolution, always reach all possible phase space points admitted by the system's macroscopic conditions. A system that satisfies this equivalence is known as an ergodic system.

One is often only interested in determining certain equilibrium properties $A(\mathbf{r}, \mathbf{p})$ of the system which are averaged over long durations of the system's evolution. This time-averaging tends to wash out the details of the microscopic trajectory of the system in phase space. Indeed, the ergodic hypothesis states that for an ergodic system, asymptotic time-averaging of a property is tantamount to taking the ensemble average of the property over the equilib-

rium phase space distribution¹:

$$\lim_{t \rightarrow \infty} \frac{1}{t} \int_0^t dt A(\mathbf{r}(t), \mathbf{p}(t)) = \int_{\mathcal{P}} \mathcal{D}\mathbf{r} \mathcal{D}\mathbf{p} \pi^*(\mathbf{r}, \mathbf{p}) A(\mathbf{r}, \mathbf{p}) \equiv \langle A(\mathbf{r}, \mathbf{p}) \rangle, \quad (3.1)$$

where $\langle \dots \rangle$ denotes the ensemble average.

Here is where Monte Carlo simulations justify their use, that is, since for the average properties $\langle A(\mathbf{r}, \mathbf{p}) \rangle$ of an ergodic system, the details of the microscopic trajectory of the system tend not to be important, so that an ensemble average can rather be used, then one may instead resort to sampling microstates of the system directly from the known equilibrium phase space distribution without necessarily following the true dynamics of a single system.

The theory of probability and statistics provides many established algorithms, known as Monte Carlo methods, that enable one to sample states directly from their distribution. Of these, the Markov Chain Monte Carlo (MCMC) algorithm has won a major following in the physicist community [50, 51]. In the present work we also adopt the MCMC methodology.

Through the MCMC method one achieves a more direct means, than MD, of studying the quasi-static/adiabatic evolution of a system's properties with temperature and other macroscopic variables, for these merely feature as parameters of the equilibrium distribution.

It should be noted that over the years, the art of designing MCMC algorithms has greatly advanced, and that many different algorithms have been devised for many different purposes [50, 51]. In particular, not all of them are restricted to sampling from equilibrium distributions alone, but some have been designed to provide kinetic information, while others can simulate non-equilibrium ensembles [51, 52]. But the description of these methods is beyond the scope of the present work.

3.2 Limitations

For both MD and MCMC simulations, the typical amount of available computer memory resources becomes severely limited in the face of the system's sheer large number ($N \sim 10^{23}$) of degrees of freedom that would need to be stored in memory, were their fully atomistic motion to be computed. Consequently one is forced to simulate only a small representative portion (the simulation box) of the entire system for a short evolution time, accompanied by the imposition of artificial boundary conditions such as periodic boundary conditions.

¹It is difficult to prove that a particular system is truly ergodic, hence this statement cannot be any more than a supposition.

The problem with such an approach is that finite-size effects come into play: first of all, the section of the system under study may just not be large enough to represent the full system under study, since some properties of the system are defined as averages of certain functions over a larger number of system particles than exist in the simulation box, and over longer evolution times than the computer can run for.

Secondly, by imposing periodic boundary conditions on the simulation box, one invariably introduces an upper limit to the possible wavelengths of thermal fluctuations that the system assumes during simulation. Yet long wavelength fluctuations are thought to be important contributors to the mechanics of systems especially under low strains and stresses [53, 1].

An alternative, which forms a key part of the so-called ‘multiscale’ simulation paradigm alluded to in the previous chapter, involves integrating out the fastest varying and the shortest wavelength degrees of freedom thus reducing the total number of state space variables to the few degrees of freedom that vary slowly, both spatially and temporally. Following this procedure, it is sometimes possible to do away with the simulation box and the periodic boundary conditions altogether. Such is the case for our simulations of collagen fibrils described later in Chapter 6.

3.3 A Brief on Markov Chain Theory

The aim of Markov Chain Monte Carlo methods, in general, is to obtain a representative set of sampled states from a target distribution whose functional form over the state space is already known at least up to a multiplicative constant. The tool employed, namely the Markov chain, is a well-defined abstract object found in the theory of probability and statistics. However in this discussion we will limit ourselves only to those aspects of Markov chains that are relevant to the present work. For a full treatment of the subject the reader is referred to Ref. [54].

A Markov chain is a sequence of random variables X_0, X_1, X_2, \dots whose values are the outcomes of trials of a particular kind, namely the Markov trial. For a trial to be defined as a Markov trial, the following condition (the Markov property) must be satisfied: the probability of a particular outcome X_i in an experiment is conditional only on the result of the outcome X_{i-1} immediately before it. In other words,

$$P(X_i | X_0, X_1, \dots, X_{i-1}) \equiv P(X_i | X_{i-1}). \quad (3.2)$$

The value of the zeroth sample X_0 is specified *a priori*. All the possible values x_r of X_i form a countable set $\mathcal{S} = \{x_0, x_1, \dots\}$ called the state space of the Markov chain.

Equation (3.2) is defined for a discrete countable state space. Hence the

conditional probabilities are usually represented as the components $T_{rs} = P(x_r | x_s)$ of a matrix, namely the transition matrix \mathbf{T} .

One approach to generalizing Markov chain theory to a continuous state-space \mathcal{Q} involves introducing a suitable infinitesimal subdivision of state-space together with a conditional probability density $p(y | x)$, so that

$$P(X_{i+1} = y | X_i = x) = p(y | x) dy \quad (3.3)$$

where $p(y | x)$ is often taken as the value of a two point function called the transition kernel defined for every pair of states x and y . The transition kernel is a conditional probability density distribution function that represents the probability per unit state space volume of moving from x to y . By virtue of its being a distribution function, we have $\int_{\mathcal{Q}} p(y | x) dy = 1$, where it is permitted that the chain can make a transition from the state x to x , that is, $p(x | x) dx$ is not necessarily zero.

In analogy with the ensemble picture discussed in the previous section, we may consider spreading an asymptotically large number of *a priori* outcomes over the entire state space \mathcal{Q} in the beginning according to some arbitrary distribution $\pi^{(0)}(x) dx$ which is defined as the probability of finding an *a priori* outcome in state x . If each of these outcomes is set to correspond with the zeroth outcome of its own Markov chain with a common transition kernel $p(y | x)$, then the ensemble of first outcomes in each Markov chain will in general have a different distribution $\pi^{(1)}(x) dx$, because for all $n = 1, 2, 3, \dots$

$$\pi^{(n+1)}(y) = \int_{\mathcal{Q}} dx p(y | x) \pi^{(n)}(x). \quad (3.4)$$

A Markov chain is called an ergodic chain if it is possible to go from every state to every state (not necessarily in one move). And once again we recognize that it is this property of ergodicity that makes the ensemble picture equivalent to the single Markov chain picture.

A major concern of Markov chain theory is to determine conditions under which there exists an invariant distribution $\pi^*(x)$ and conditions under which iterations of the transition kernel converge to the invariant distribution. The invariant distribution satisfies

$$\pi^*(y) = \int_{\mathcal{Q}} dx p(y | x) \pi^*(x). \quad (3.5)$$

MCMC methods turn the theory around: the invariant density $\pi^*(x)$ is known (perhaps up to a constant multiple) and samples from it are desired, hence the transition kernel needs to be solved for. We discuss how to this in the following section.

3.4 The Metropolis Algorithm

The way to obtain the representative set of samples is to devise an algorithm that mimics a Markov process/chain stepping through state space and whose transition probability matrix/kernel is constructed in such a way that it reproduces the target distribution as the limiting distribution of the Markov chain.

In this way, the algorithm produces a sample state with every step, and after sufficiently many steps N these samples are distributed according to the target distribution. Once the representative set of sampled states is obtained, the sample mean of any property over this set is a good estimate for the ensemble average of that property over the target distribution:

$$\langle A(\mathbf{r}) \rangle \approx \frac{1}{N} \sum_{n=0}^N A(\mathbf{r}_n). \quad (3.6)$$

In the present work, the state space is the configuration space (not the phase space) of the system under study, and the target distribution is actually the Boltzmann distribution $\exp(-E(\mathbf{r})/k_B T)$ over the configuration space, that is, the momenta have been integrated out.

The Metropolis algorithm, in particular, mimics a reversible Markov chain. Here, reversibility means that the Markov chain, in addition, obeys the detailed balance condition for the target distribution; it is an imposition on the transition probability matrix/kernel. For systems with a discrete state space (such as in lattice systems), this reads:

$$\pi_j^* T_{ij} = \pi_i^* T_{ji}. \quad (3.7)$$

For continuous state-space (such as in off-lattice systems), one may generalize the above relation by introducing a suitable subdivision of state-space together with a state probability density, and subsequently taking the limit as the subdivision becomes finer and finer:

$$\pi^*(x) dx p(y | x) dy = \pi^*(y) dy p(x | y) dx. \quad (3.8)$$

Of course, the above equation reduces to a relation involving only the probability densities and the transition kernel, since we can immediately eliminate the infinitesimal volume elements from both sides of the equation. However we shall maintain Equation 3.8 in its present form, since, as we shall soon see, the transition kernel is usually not explicitly known for the Metropolis algorithm. Instead the products $p(y | x) dy$ and $p(x | y) dx$ are fully known.

Detailed balance is sufficient, but not necessary, for the limiting distribution of the Markov chain to equal the target distribution.²

²Note that it is merely a coincidence that detailed balance, which here is introduced only *ad hoc*, also holds for a microcanonical ensemble of physical systems governed by classical dynamics.

The step from state x to y may be, in general, described by a transformation $\mathbf{f} : x \mapsto y$, that is,

$$y = \mathbf{f}(x), \quad (3.9)$$

where $\mathbf{f}(\cdot)$ is an invertible function.³ Then the detailed balance equation may be rewritten as:

$$\pi(x) p(y | x) dy = \left| \left| \frac{\partial y}{\partial x} \right| \right| \pi(y) p(x | y) dx \quad (3.10)$$

where $\left| \frac{\partial y}{\partial x} \right|$ is the Jacobian determinant of the transformation \mathbf{f} . Note that it is mandatory that $\mathbf{f}(\cdot)$ possess an inverse, since, according to the detailed balance condition there has to be a non-zero probability $p(x | y) dx$ of returning to state x conditional on y being the current state.

With each step, the Metropolis algorithm proceeds in two stages, it begins by proposing a new state y , and next it determines whether it should accept the newly proposed state y as the next state, otherwise it rejects the proposed state by taking the current state x as the next state. The Metropolis algorithm achieves this process by separating the transition kernel $p(y | x)$ into two factors: the acceptance probability $\text{acc}_{x \rightarrow y}$ and the *a priori* proposal probability density $P_{\text{gen}}(y | x)$:

$$p(y | x) dy = \text{acc}_{x \rightarrow y} P_{\text{gen}}(y | x) dy. \quad (3.11)$$

The latter factor, which is equal to the probability per unit state-space volume of proposing y as the next state, given the current state is x is, in general, not explicitly known, but it is implicit in the following form:

$$P_{\text{gen}}(y | x) dy = P_{\text{gen}}(\Delta) d\Delta, \quad (3.12)$$

where the density $P_{\text{gen}}(\Delta)$ is explicitly known, and Δ is a computer-generated random variable (of generally much lower dimension than that of x) that roughly denotes the ‘displacement’ of the trial move $x \rightarrow y$. Indeed Δ is used to ‘displace’ the current state x via parameterization of the transformation, that is, $y = \mathbf{f}_{\Delta}(x)$. Furthermore, one is free to construct $P_{\text{gen}}(\Delta)$ and \mathbf{f}_{Δ} at will, as long as they cause the system being studied to be ergodic. The transformation \mathbf{f}_{Δ} is called a ‘move type’, and it is typically randomly chosen from

For there, detailed balance is actually a consequence of the physical phenomenon of microscopic reversibility (time-reversal symmetry of the equations of motion) among other things. Here, on the other hand, the dynamics are quite different, being governed by the master equation for Markov chains.

³In MD simulations, $\mathbf{f}(x)$ is completely determined after every time step by the Verlet algorithm (or the particular adopted numerical scheme of the equations of motion) and all microstate coordinates are transformed in the process, whereas in MCMC simulations \mathbf{f} may be any invertible function not necessarily corresponding to a physical move of the system. In fact, one may even choose to restrict the move \mathbf{f} to a small subset of the configuration coordinates of the system.

among other move types in a set, called the ‘move set’ \mathcal{M} . In the next chapter, we will discuss certain move types that are especially suited for the simulation of polymers.

The acceptance probability $\text{acc}_{x \rightarrow y}$, on the other hand, is solved for at every step so as to satisfy detailed balance. The solution is:

$$\text{acc}_{x \rightarrow y} = \min \left(1, \frac{\pi(y)}{\pi(x)} \frac{P_{\text{gen}}(x | y) dx}{P_{\text{gen}}(y | x) dy} \left\| \frac{\partial y}{\partial x} \right\| \right). \quad (3.13)$$

The reader may verify that this is correct by substituting this expression into the detailed balance condition Equation (3.8).

Now the Metropolis algorithm may be summarized as follows. Let the steps be labeled by the integers $t = 0, 1, 2, \dots$. Then, given that the current state is \mathbf{r}_t :

1. Proposal: choose an invertible move type \mathbf{f}_Δ at random from \mathcal{M} ; generate a random value for Δ from the distribution $P_{\text{gen}}(\Delta)d\Delta$; and find $y = \mathbf{f}_\Delta(\mathbf{r}_t)$.
2. Acceptance: the proposed move $\mathbf{r}_t \mapsto \mathbf{r}_{t+1}$ should be accepted with a probability:

$$\text{acc}_{\mathbf{r}_t \rightarrow \mathbf{r}_{t+1}} = \min \left(1, \frac{\pi(\mathbf{r}_{t+1})}{\pi(\mathbf{r}_t)} \frac{P_{\text{gen}}(\mathbf{r}_t | \mathbf{r}_{t+1}) d\mathbf{r}_t}{P_{\text{gen}}(\mathbf{r}_{t+1} | \mathbf{r}_t) d\mathbf{r}_{t+1}} \left\| \frac{\partial \mathbf{r}_{t+1}}{\partial \mathbf{r}_t} \right\| \right). \quad (3.14)$$

Otherwise reject the move and set $\mathbf{r}_{t+1} = \mathbf{r}_t$.

Note that P_{gen} is often constructed to be symmetric, that is, $P_{\text{gen}}(\Delta)d\Delta = P_{\text{gen}}(-\Delta)d\Delta$, which implies [see Equation (3.12)] that $P_{\text{gen}}(y | x) dy = P_{\text{gen}}(x | y) dx$ for any pair of states x and y . Then the second argument in Equation (3.14) reduces to

$$\alpha_{(t) \rightarrow (t+1)} = \frac{\pi(\mathbf{r}_{t+1})}{\pi(\mathbf{r}_t)} \left\| \frac{\partial \mathbf{r}_{t+1}}{\partial \mathbf{r}_t} \right\|, \quad (3.15)$$

which is called the acceptance ratio of the move.

CHAPTER 4

MARKOV CHAIN MONTE CARLO FOR POLYMERIC SYSTEMS

In this chapter we introduce novel moves for the Metropolis algorithm to simulate cross-linked networks of freely-jointed and discrete worm-like chains. These new moves are:

1. The Discrete Tractrix Transformation of a rigid bond [$\chi(\delta)$],
2. TRACTRIX for Free Linear Chains [$\mathcal{T}_F(\delta)$], and
3. TRACTRIX for Anchored Linear Chains [$\mathcal{T}_A(\Delta)$].

In all cases, bond movement is based on the discrete tractrix construction which preserves the fixed-length constraints of bonds. The Jacobians of these moves are also computed in this chapter. The next chapter reports on certain tests that were performed to validate these moves.

4.1 The Issues of Kinematic Constraints and Network Connectivity

The Kratky-Porod worm-like chain (WLC) [30] has proven to be an indispensable model for the coarse-grained description of semi-flexible polymers. Biophysicists, in particular, have applied the model to glean the mechanics of a large variety of biological filaments, including double-stranded DNA [31], unstructured RNA, tropocollagen [7], and many other polypeptides. However, in a living organism such filaments hardly ever occur or function alone as single chains. Instead, they often occur cross-linked together with many other chains thus becoming the building blocks of much larger bundles or networks. It is therefore only natural to consider the supramolecular structures of WLC's and study the effect of cross-linking in them. The WLC is specified by a continuously differentiable space curve $\mathbf{r}(s)$ of length ℓ_c parametrized by the arc length parameter s . It is further endowed with a Hamiltonian that quantifies the cost of bending the curve [55]:

$$\mathcal{H} = \frac{\kappa}{2} \int_0^{\ell_c} ds \left(\frac{\partial^2 \mathbf{r}}{\partial s^2} \right)^2, \quad (4.1)$$

where κ is the bending modulus. Implicit in this definition is the constraint of local inextensibility, that is, the local tangent magnitude $|\partial \mathbf{r} / \partial s|$ is unity. An important length-scale that arises from this model is the persistence length $\ell_p = \kappa / k_B T$ which is the characteristic length governing the decay of tangent-tangent correlations and provides a quantitative measure for a polymer's flexibility. Though the specification of the WLC model appears to be simple, the constraint of local inextensibility inherent in the model leads to considerable mathematical difficulty when attempting to obtain an analytical solution of even the simplest of such thermally fluctuating network structures. Nonetheless, Wilhelm *et al.* [32] have obtained the radial distribution function for the single stiff polymer (i.e., with $\ell_p \gtrsim \ell_c$). Furthermore, Storm *et al.* [34] have produced elasticity estimates of affinely-deformed isotropic random networks of WLC's.

Laboratory experiments and computer simulations may have to pave the way to investigate the properties of those biological network architectures that remain analytically intractable. Even so, non-trivial complications arise since one often, as a first step, needs to discretize the WLC reducing it to a chain of tethers of fixed length. The widely used Molecular Dynamics (MD) constraint algorithms, such as SHAKE and RATTLE [56, 57] have been developed to deal with these fixed-length constraints. But these algorithms have been reported as being limited to mechanical systems with tree-structures and rigid loops [58]. (See Figure 4.1 b and c.)

Markov Chain Monte Carlo (MCMC) constraint algorithms offer a tantalizing alternative in that being purely stochastic, they allow for unphysical moves

thus eliminating the need for time-step integration and quickly providing good equilibrium statistics. Over the past 30 years, a number of ‘smart’ MCMC moves have been advanced for the simulation of atomistic models of melts of polymeric systems [50, 59, 60]. After a few modifications (for example, after removing the fixed bond-angle constraint inherent in many atomic-scale models) most of these techniques can be carried over into the simulation of the more coarse-grained discrete WLC models (where bond-lengths could be $0.25\ell_p$ or less, stretching over many atomic bonds). However, these techniques are limited in the variety of cross-linked architectures which they are able to address [60, 61].

In this chapter we introduce a Metropolis algorithm sampling technique that may be used to accurately simulate various cross-linked freely-jointed ($\ell_p = 0$) or discrete WLC architectures such as those shown in Figure 4.1 (d, e, and f). The common feature of these networks that sets them apart from the rest [a, b, and c in Figure 4.1] is the existence of conjoined closed loops that share one or more polymer links, a feature which we wish to address. This very feature is immediately apparent in biological gels when they are observed under the microscope. These gels often have a density of chemical entities generally called *cross-links* that affect the mechanical properties of the gel. A cross-link typically binds together two polymers at some point along their contours, therefore often producing four-fold coordination at each cross-linking site.

Three main technical problems are to be addressed in the implementation of our method: preservation of the connectivity of the network structure, conformance to the fixed-length constraints of the inter-linking tethers, and *detailed balance*. For the latter requirement, we adhere to the recipe of the standard Metropolis algorithm, which is to ensure that each trial move is reversible, and that its probability of acceptance – the so-called *acceptance ratio* – is correctly computed to eventually yield Boltzmann statistics. As pointed out by Maggs [62], the computation of the acceptance ratio for trial moves in systems whose phase space is a continuum (i.e., off-lattice systems) often requires the computation of a Jacobian determinant, since in transforming from one state of the system to another during a simulation, the infinitesimal volume element in the vicinity of the state is also transformed, the measure of which, in general, is not preserved during the transformation (see Section 3.4). In what follows, we will describe the moves and the computation of their acceptance ratios.

The structure of networks requires the use of a set of specialized types of moves, called the *move set* \mathcal{M} , from which the algorithm may randomly select a move as a proposal. Any desired probability distribution can be built over \mathcal{M} to increase the frequency of occurrence of some move types over others. In the following sections we outline the types of proposal moves belonging to our move set.

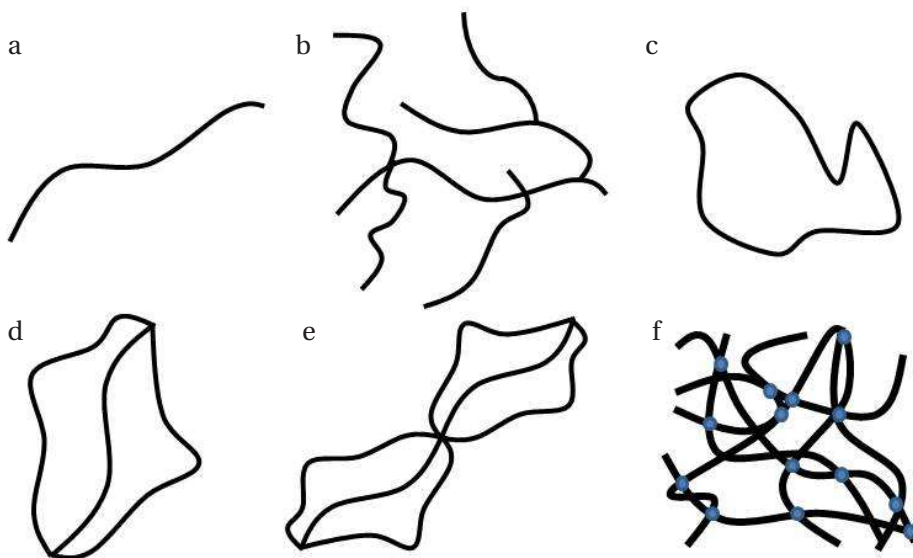


Figure 4.1: Examples of polymeric architectures that the MCMC sampling technique introduced in this chapter can address. Legend: (a) Linear chain, (b) loop-less branched polymer, (c) closed-loop, (d), (e) and (f) are network structures which possess two or more closed-loops that share the same polymeric link.

4.2 Crank-Shaft $\mathcal{C}(\theta_c)$

The crank-shaft move type is not new. It has often been used in the simulation of single linear chains because of its simplicity and ease of computation. It works as follows: first randomly select a pair of distinct points (called mass-points) along the same linear chain, then rotate that section of the linear chain occurring between these two mass-points around the axis joining the two mass-points and through an angle θ_c whose value is randomly selected from a symmetric distribution over a given interval $[-\theta_{\max}, \theta_{\max}]$ (see Figure 4.2). The distribution of angles θ_c needs to be symmetric over the interval so as to ensure that the condition of reversibility stipulated by the Metropolis algorithm is obeyed. The Jacobian of such a transformation is unity.¹

Care should be taken to ensure that the algorithm does not randomly select a pair of mass-points whose intervening chain fragment goes through a cross-link, because then the subsequent crank-shaft rotation would destroy

¹Another variant of the crank-shaft move (not used in the present work) involves three linear chains that terminate at one point. In this case, three points are randomly selected (one on each chain). These three points define a plane about which those linear portions of the chains between the mass-points and the terminus can be reflected. Unlike TRACTRIX (described in the following sections), such a move offers little control over where to place the mass-points.

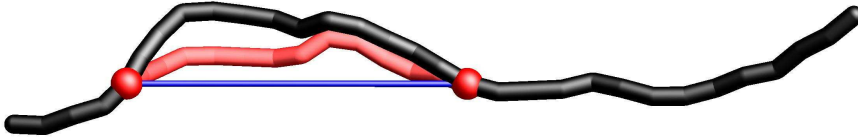


Figure 4.2: The crank-shaft move: the fragment intervening the two randomly chosen mass-points (represented by the red balls) on a linear chain is rotated by a random angle about the axis (represented by the blue line) joining these mass-points. See Section 4.2 for more details.

the cross-link, immediately compromising our model. Thus, crank-shaft rotations must occur only for those linear chain fragments occurring between cross-links. As a result, the cross-links of a network are never moved during a crank-shaft move.

The foregoing discussion means that another type of move is required to displace also the cross-links, enabling them to fluctuate while simultaneously preserving the connectivity of the cross-linked system. Such a move would prove useful in an investigation of the importance of long-wavelength fluctuations to elasticity, which are mediated by cross-link fluctuations in a polymer network (such as, for example, in rubber [53]).

It is for this reason that we formulate a novel type of move called TRACTRIX. In the following sections, we outline this move.

4.3 The Idea: Tractrix

The tractrix is the answer to the following question [63]: “Given two points linked by a rigid joint, if one point moves along a given curve, how does the other point move?” Historically², the tractrix was the name given to the path

²This problem is usually attributed to Leibniz (1646-1716). He states it in his 1693 *Leipziger Acta Eruditorum* problem: “In the xy -plane drag a point P with a tightly strained string PZ of length a . The ‘drag point’ Z shall propagate along the positive y -axis, and at the beginning P shall be in $(a, 0)$. Which curve is described by P ?” For comprehension Leibniz imagined a pocket watch on a chain. But as source of the problem he mentions the Parisian architect Claude Perault. The curve was also studied by Isaac Newton (1676) and Christian Huygens (1692), who gave it the

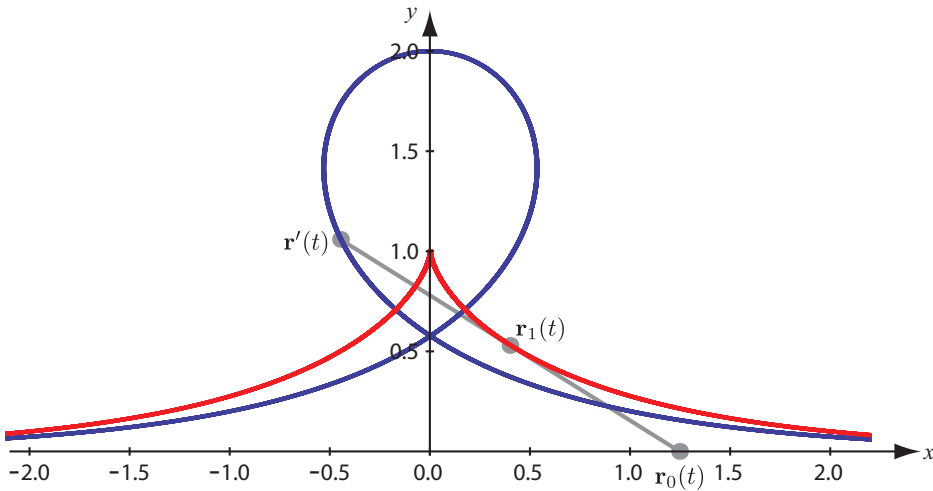


Figure 4.3: The tractrix (red curve) of the x -axis: here the pulling point $\mathbf{r}_0(t)$ moves along the x -axis, while the pulled point $\mathbf{r}_1(t)$ moves along the red curve, a distance of one unit length away from $\mathbf{r}_0(t)$, another point $\mathbf{r}'(t)$, two unit lengths away from $\mathbf{r}_0(t)$, follows the blue curve, called the Darboux transform of the x -axis. When time $t = 0$, $\mathbf{r}_0(t) = (0, 0)$, $\mathbf{r}_1(t) = (0, 1)$, and $\mathbf{r}'(t) = (0, 2)$.

of pursuit along which an object moves, under the influence of friction, when pulled on a horizontal plane by a piece of thread. For instance an initially stationary water skier follows the path of a tractrix when he/she is pulled by means of a taut rope attached to a boat moving in a straight line.

The key properties here are that the velocity of the object being pulled is always directed along the rope towards the pulling object, and secondly, the distance between the pulling object and the pulled object, that is, the length ℓ of the rope, is constant (see, for example, Figure 4.3).

Thus the tractrix may be described by the following differential problem: given $\mathbf{r}_0(t)$ and ℓ , find $\mathbf{r}_1(t)$ such that

$$\frac{\partial \mathbf{r}_1(t)}{\partial t} \propto (\mathbf{r}_0(t) - \mathbf{r}_1(t)) \quad \text{and} \quad (4.2)$$

$$|\mathbf{r}_0(t) - \mathbf{r}_1(t)| = \ell. \quad (4.3)$$

In a discretization of this problem, the curve $\mathbf{r}_0(t)$ on which the first point moves would be a sequence of points $\mathbf{r}_0^{(s)}$ with $s = 0, 1, \dots$. Now a straight forward discretization of the tractrix would be the following: if $\mathbf{r}_0^{(s)}$ moves (jumps) to $\mathbf{r}_0^{(s+1)}$, then $\mathbf{r}_1^{(s+1)}$ is chosen to be the point on the straight line through $\mathbf{r}_0^{(s+1)}$ and $\mathbf{r}_1^{(s)}$ that is a distance ℓ from $\mathbf{r}_0^{(s+1)}$ and on the same side as $\mathbf{r}_1^{(s)}$. While

name 'tractrix'.

this discretization might work well and even converge to the smooth solution eventually, it has a crucial drawback: in contrast to the smooth model the discretization is not time-reversible. That is, if $\mathbf{r}_0^{(s+1)} = \mathbf{r}_0^{(s-1)}$ then $\mathbf{r}_1^{(s+1)}$ need not be equal to $\mathbf{r}_1^{(s-1)}$.

There is, however, a smooth result, due to Hoffmann [63], that leads to a simple discretization that overcomes this. In the smooth case it turns out that there is a third curve $\mathbf{r}'(t)$ at distance 2ℓ from $\mathbf{r}_0(t)$ so that $\mathbf{r}_1(t) = \frac{1}{2}(\mathbf{r}_0(t) + \mathbf{r}'(t))$ and $\mathbf{r}_0(t)$ and $\mathbf{r}'(t)$ are arc-length related: $|\frac{\partial \mathbf{r}_0(t)}{\partial t}| = |\frac{\partial \mathbf{r}'(t)}{\partial t}|$. This curve $\mathbf{r}'(t)$ is usually called a Darboux transform of $\mathbf{r}_0(t)$ [64].

The relation between $\mathbf{r}_0(t)$ and $\mathbf{r}'(t)$ translates easily into the discrete realm: $|\mathbf{r}_0^{(s+1)} - \mathbf{r}_0^{(s)}| = |\mathbf{r}'^{(s+1)} - \mathbf{r}'^{(s)}|$. And since $|\mathbf{r}_0^{(s)} - \mathbf{r}'^{(s)}| = |\mathbf{r}_0^{(s+1)} - \mathbf{r}'^{(s+1)}| = 2\ell$ one sees that the four points $\mathbf{r}_0^{(s)}$, $\mathbf{r}_0^{(s+1)}$, $\mathbf{r}'^{(s+1)}$, and $\mathbf{r}'^{(s)}$ form a parallelogram folded along one of its diagonals. The second solution is the one we are interested in. The discrete tractrix of $\mathbf{r}_0(t)$ can now be defined as simply $\mathbf{r}_1^{(s)} = \frac{1}{2}(\mathbf{r}_0^{(s)} + \mathbf{r}'^{(s)})$, and since the construction of $\mathbf{r}'^{(s+1)}$ from $\mathbf{r}_0^{(s)}$, $\mathbf{r}_0^{(s+1)}$ and $\mathbf{r}'^{(s)}$ is completely symmetric in s and $s + 1$, time-reversibility is built in the definition this time.

4.4 The Discrete Tractrix Transformation of a Rigid Bond $[\chi(\delta)]$

The foregoing discussion strongly suggests that one might employ the time-reversible discrete tractrix construction to create a Metropolis move for a rigid bond \mathbf{t} of a discrete linear chain. The reason is because of the following requirements that need to be met for the Metropolis move to be valid:

1. The length of the bond must not change after the move, and
2. the move must possess an inverse for detailed balance to hold.

Thus, if at some MCMC step s , we assign to the two ends of the rigid bond the coordinates $\mathbf{r}_0^{(s)}$ and $\mathbf{r}_1^{(s)}$, then these two requirements are exactly met in the discrete tractrix construction through the constancy of the distance $\ell = |\mathbf{r}_1^{(s)} - \mathbf{r}_0^{(s)}|$ and the time-reversibility of the construction, respectively. Moreover, the displacement δ of the end, with coordinates $\mathbf{r}_0^{(s)}$, to the new position $\mathbf{r}_0^{(s+1)}$ completely determines the new position $\mathbf{r}_1^{(s+1)}$ of the other end.

We will coin this new move the ‘Discrete Tractrix Transformation’ (DTT) $\chi(\delta)$. The DTT $\chi(\delta)$ is pictured in Figure 4.4, and it can be described as follows:

1. Rigidly translate the bond \mathbf{t} by δ so that $\{\mathbf{r}_0^{(s)}, \mathbf{r}_1^{(s)}\}$ is moved to $\{\mathbf{r}_0^{(s+1)}, \mathbf{r}_1^{(s)}\}$.

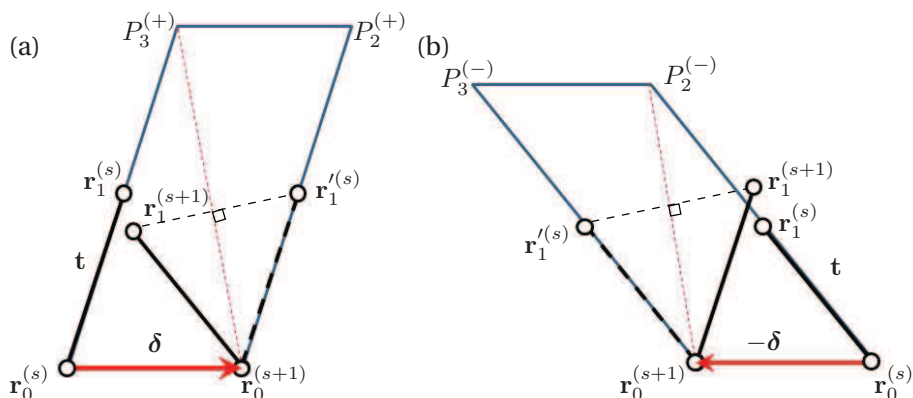


Figure 4.4: (a) Discrete tractrix transformation of the bond t : 1. Rigidly translate the bond t by δ so that $\{r_0^{(s)}, r_1^{(s)}\}$ is moved to $\{r_0^{(s+1)}, r_1'^{(s)}\}$. 2. Form the parallelogram spanned by δ_0 and ft . (Here we set $f = 2$.) 3. To obtain $r_1^{(s+1)}$ reflect $r_1'^{(s)}$ in the parallelogram's diagonal which passes through $r_0^{(s+1)}$. (b) Inverse of the transformation in (a) showing that the tractrix transformation is reversible. In both cases the length of the bond is preserved.

2. Form the parallelogram spanned by δ_0 and ft , where f is some adjustable factor ($f = 2$ in Figure 4.4).
3. To obtain $r_1^{(s+1)}$ reflect $r_1'^{(s)}$ in the parallelogram's diagonal which passes through $r_0^{(s+1)}$.

Figure 4.4b shows that following the same procedure for the inverse transform $\chi(\delta)^{-1} = \chi(-\delta)$, but this time starting from the initial position $\{r_0^{(s+1)}, r_1'^{(s)}\}$ we recover the original pair $\{r_0^{(s)}, r_1^{(s)}\}$ thus demonstrating the transform's reversibility. The free parameter f featured in these equations has a nominal value of 2 which corresponds to the physical situation of an object being dragged under the influence of friction. However, since the MCMC move need not be a physical move, the value of f may be arbitrarily chosen before the start of the simulation and thereafter held constant. Roughly, f controls the amount of translation, as opposed to rotation, that the bond undergoes during the move: the higher its value, the less the bond rotates and the more the bond is merely translated.

For completeness, the proof of the reversibility of $\chi(\delta)$ is given geometrically in Figure 4.5, in which the parallelograms of Figures 4.4a and b are superimposed.

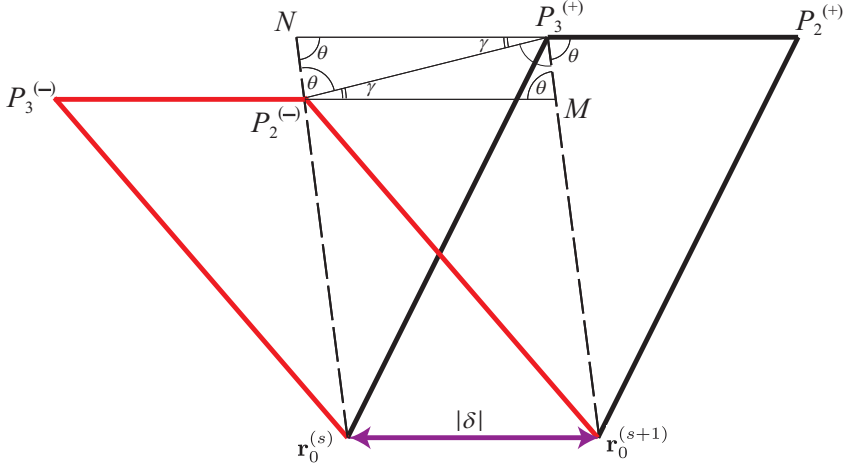


Figure 4.5: Geometric proof of reversibility of $\chi(\delta)$: the two parallelograms of Figures 4.4a and b are superimposed; $P_2^{(-)}$ is the reflection of $P_2^{(+)}$ in the diagonal $\overline{r_0^{(s+1)}P_3^{(+)}}$ of parallelogram $r_0^{(s)}r_0^{(s+1)}P_2^{(+)P_3^{(+)}}$. Line $\overline{P_2^{(+)P_3^{(+)}}$ is extended to point N . A close look at the labeled angles of the diagram reveals that $\overline{P_2^{(-)}M}$ is parallel to $\overline{P_3^{(+)P_2^{(+)}}$, and that both lines have the same length $|\delta|$ as $\overline{P_2^{(-)}P_3^{(+)}}$. Therefore the parallelogram diagonals $\overline{r_0^{(s)}P_2^{(-)}}$ and $\overline{r_0^{(s+1)}P_3^{(+)}}$ are parallel. This leads to $P_3^{(+)}$ being the reflection of $P_3^{(-)}$ in $r_0^{(s)}P_2^{(-)}$. The two parallelograms are therefore dual to one another. Since these relations are independent of the value of f , we conclude that $\chi(\delta)^{-1} = \chi(-\delta)$.

By writing out the transformation $\chi(\delta)$ in vector form, it is automatically generalized to any spatial dimension $d > 1$:

$$\mathbf{r}_0^{(s+1)} = \mathbf{r}_0^{(s)} + \boldsymbol{\delta}, \quad (4.4)$$

$$\mathbf{r}_1^{(s+1)} = \chi_{\text{T}}(\mathbf{r}_1^{(s)}, \mathbf{r}_0^{(s)}, \boldsymbol{\delta}, f) \equiv \mathbf{p} + 2 \left[\frac{(\mathbf{r}_0^{(s)} - \mathbf{r}_1^{(s)}) \cdot \mathbf{w}}{\mathbf{w} \cdot \mathbf{w}} \right] \mathbf{w}, \quad (4.5)$$

where $\mathbf{p} = \mathbf{r}_1^{(s)} + \boldsymbol{\delta}$ and $\mathbf{w} = f(\mathbf{r}_1^{(s)} - \mathbf{r}_0^{(s)}) - \boldsymbol{\delta}$.

4.5 TRACTRIX for Free Linear Chains [$\mathcal{T}_F(\delta_0)$]

We now proceed to formulate a MCMC move for a linear chain which is represented by a sequence of jointed bonds of fixed length. We will start with a linear chain for which *both* ends are initially free to move and we will determine its new position after we displace one end (here called the ‘driver node’)

by δ_0 . In the next section, we will consider a linear chain which must have one end (called the ‘anchor’) fixed during the move.

Without loss of generality, a linear chain may be discretized into a series of N_P bonds $\mathbf{t}_1, \mathbf{t}_2, \dots, \mathbf{t}_{N_P}$ of fixed length t interlinking the sequence of vertices P_0, P_1, \dots, P_{N_P} (here called ‘mass-points’) with coordinates $\mathbf{r}_0^{(s)}, \mathbf{r}_1^{(s)}, \dots, \mathbf{r}_{N_P}^{(s)}$, so that the i -th bond $\mathbf{t}_i = \mathbf{r}_i^{(s)} - \mathbf{r}_{i-1}^{(s)}$. The coordinates thus obey a set of constraints: $\left| \mathbf{r}_i^{(s)} - \mathbf{r}_{i-1}^{(s)} \right| - t = 0 \quad (t = \text{const.}), \quad i = 0, 1, \dots, N_P$.

The choice of a suitable value for N_P or t depends on such factors as the persistence length ℓ_p in the case of a WLC, or the Kuhn length in the case of a freely-jointed chain. The bending energy of the discretized WLC may be given by $\mathcal{E}(\mathbf{r}_k) = -\varepsilon \sum_{i=1}^{N_P-1} \mathbf{t}_i \cdot \mathbf{t}_{i+1}$, where $\varepsilon = k_B T \ell_p / t^3$. This expression can be shown to approach the energy for the continuous chain in Eq. (4.1) in the limit of $N_P \rightarrow \infty$ and $t \rightarrow 0$ while keeping constant $N_P t = \ell_c$ and $\varepsilon t^2 / N_P$. However, it is sufficient to discretize the WLC so that there are at least 3 bonds in one persistence length [32].

Clearly, whatever move $\mathcal{T}_F(\delta_0)$ we come up with for the entire chain should maintain the connectivity of its rigid links. Then the most obvious way to effect such a transformation on the entire chain is by displacing the polymer end $\mathbf{r}_0^{(s)}$ by δ_0 so that $\mathbf{r}_0^{(s+1)} = \mathbf{r}_0^{(s)} + \delta_0$, then successively applying the discrete tractrix transformation $\chi(\delta_i)$ with constant f to every bond $\mathbf{t}_1, \mathbf{t}_2, \dots, \mathbf{t}_{N_P}$ in that order, each time setting $\delta_i = \mathbf{r}_i^{(s+1)} - \mathbf{r}_i^{(s)}$. The following are the recursive relations describing the move $\mathcal{T}_F(\delta_0) : \{\mathbf{r}_0^{(s)}, \mathbf{r}_1^{(s)}, \dots, \mathbf{r}_{N_P}^{(s)}\} \mapsto \{\mathbf{r}_0^{(s+1)}, \mathbf{r}_1^{(s+1)}, \dots, \mathbf{r}_{N_P}^{(s+1)}\}$:

$$\begin{aligned} \mathbf{r}_0^{(s+1)} &= \mathbf{r}_0^{(s)} + \delta_0, \\ \mathbf{r}_i^{(s+1)} &= \chi_T(\mathbf{r}_i^{(s)}, \mathbf{r}_{i-1}^{(s)}, \mathbf{r}_{i-1}^{(s+1)} - \mathbf{r}_{i-1}^{(s)}, f), \quad 0 < i \leq N_P. \end{aligned} \quad (4.6)$$

None of the lengths of the bonds are changed by this process, but rather the bonds are rotated and displaced causing the end-to-end vector of the chain also to change, albeit not by the given displacement δ_0 , since the tail P_{N_P} of the chain is also displaced in the process. This particular feature of the transformation is used to formulate a MCMC move for anchored linear chains in the next section.

Evidently $\mathcal{T}_F(\delta_0)$ is also reversible, since, to recover the original configuration from the new one, all we need to do is apply $\mathcal{T}_F(-\delta_0)$ to the new configuration.

We recall that to compute the acceptance ratio for this move, its Jacobian determinant $\det \mathbf{J}_{\mathcal{T}_F(\delta_0)}$ needs to be determined. To do so, first of all we recognize that in d -dimensions the Jacobian matrix $\mathbf{J}_{\mathcal{T}_F(\delta_0)}$ can be written down as block matrix, each block being a $d \times d$ matrix. The square block located at the i -th block row and j -th block column of $\mathbf{J}_{\mathcal{T}_F(\delta_0)}$ is the matrix $\frac{\partial \mathbf{r}_i^{(s+1)}}{\partial \mathbf{r}_j^{(s)}}$, where $\mathbf{r}_j^{(s)}$ is the position of the j -th mass-point in the current state s of the system, and

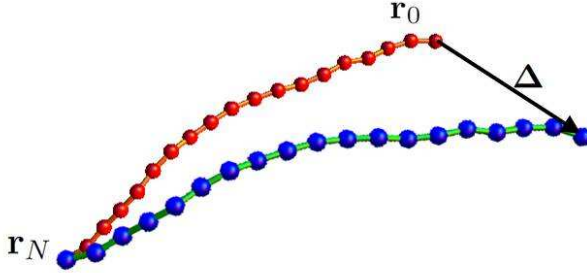


Figure 4.6: Action of the transformation $\mathcal{T}_A(\Delta)$: it moves one end of the chain \mathbf{r}_0 so that its end-to-end vector is incremented by exactly Δ , while keeping the other end fixed in space and respecting all the fixed bond-length constraints.

$\mathbf{r}_i^{(s+1)}$ is the position of the i -th mass-point in the newly proposed state $s + 1$ of the polymer.

Secondly, as far as $\mathcal{T}_F(\delta)$ is concerned, the new position $\mathbf{r}_i^{(s+1)}$ of any mass-point P_i on the linear chain fragment is determined only by the positions of all mass-points along the chain between P_i and the driver node P_0 inclusive (see Equation. 4.6). This dependency gives rise to a lower d -block-triangular Jacobian matrix if the d -block rows and d -block columns are arranged in the same order in which their corresponding mass-points appear along the linear chain, beginning with the mass-point nearest the driver node, and going from top to bottom (for the rows), and from left to right (for the columns). Then $\det \mathbf{J}_{\mathcal{T}_F(\delta_0)}$ is simply the product of determinants of the d -block matrices along the diagonal:

$$\det \mathbf{J}_{\mathcal{T}_F(\delta_0)} = \prod_{i=1}^{N_P} \left\| \frac{\partial \mathbf{r}_i^{(s+1)}}{\partial \mathbf{r}_i^{(s)}} \right\|, \quad (4.7)$$

where the index i runs over all mass-points of the free linear chain (excluding that of the driver node P_0 which contributes a trivial factor of 1 to the determinant). Each factor of the product in the latter equation can be obtained by differentiating Equation (4.6) appropriately.

For further details, we refer the reader to the C++ codes implementing the above formulae. These codes are provided as supplementary material and can be found at Ref. [65].

4.6 TRACTRIX for Anchored Linear Chains [$\mathcal{T}_A(\Delta)$]

As mentioned in the previous section, one important feature of $\mathcal{T}_F(\delta_0)$ is that, due to the concerted rotation of the bonds, the end-to-end vector $\mathbf{R}^{(s)} = \mathbf{r}_0^{(s)} - \mathbf{r}_{N_P}^{(s)}$ of the linear chain changes, albeit not by δ_0 , since the other end \mathbf{r}_{N_P} is also displaced in the process. However, suppose we wanted to change the end-to-end vector of the polymer by exactly Δ , there may exist some $\delta_0 = \delta^*$ for which the application of $\mathcal{T}_F(\delta^*)$ makes this possible, i.e., $\mathbf{R}^{(s)} + \Delta = \mathbf{r}_0^{(s)} + \delta^* - \mathbf{r}_{N_P}^{(s+1)}$.

Therefore we may address the problem of an anchored polymer chain by temporarily setting it free, next determining $\mathcal{T}_F(\delta^*)$ for which $\mathbf{R}^{(s)}$ is incremented by exactly Δ . Then, after applying $\mathcal{T}_F(\delta^*)$ to obtain $\{\mathbf{r}'_0^{(s)}, \mathbf{r}'_1^{(s)}, \dots, \mathbf{r}'_{N_P}^{(s)}\}$, we *rigidly* translate the entire chain by a displacement $\mathbf{r}_{N_P}^{(s)} - \mathbf{r}'_{N_P}^{(s)}$ so that the tail end which was temporarily set free coincides once more with its previous position. We summarize the full transformation $\mathcal{T}_A(\Delta)$: $\{\mathbf{r}_0^{(s)}, \mathbf{r}_1^{(s)}, \dots, \mathbf{r}_{N_P}^{(s)}\} \mapsto \{\mathbf{r}_0^{(s+1)}, \mathbf{r}_1^{(s+1)}, \dots, \mathbf{r}_{N_P}^{(s+1)}\}$ of the anchored linear discretized chain as follows:

$$\mathbf{r}_0^{(s+1)} = \mathbf{r}_0^{(s)} + \delta^* - (\mathbf{r}_{N_P}^{(s)} - \mathbf{r}'_{N_P}^{(s)}) = \mathbf{r}_0^{(s)} + \Delta, \quad (4.8)$$

$$\mathbf{r}_i^{(s+1)} = \mathbf{r}'_i^{(s)} - (\mathbf{r}_{N_P}^{(s)} - \mathbf{r}'_{N_P}^{(s)}), \quad 0 < i < N_P, \quad (4.9)$$

where δ^* solves the second equality in Eq. (4.8), and

$$\begin{aligned} \mathbf{r}'_0^{(s)} &= \mathbf{r}_0^{(s)} + \delta^*, \\ \mathbf{r}'_i^{(s)} &= \chi_T(\mathbf{r}_i^{(s)}, \mathbf{r}'_{i-1}^{(s)}, \mathbf{r}'_{i-1}^{(s)} - \mathbf{r}_{i-1}^{(s)}, f), \quad 0 < i \leq N_P. \end{aligned} \quad (4.10)$$

In d dimensions, Eq. (4.8) is a system of d nonlinear equations in d unknowns which may be solved for δ^* . In practice, a numerical solver (e.g., a Newton-Raphson routine) is employed for such a computation.

However, during a MCMC simulation, due to the nonlinearity of these d equations, additional care should be taken to ensure that the numerical solver employed also reproduces the inverse transformation. If at some step, the numerical solver fails to produce an inverse configuration equal to the original configuration, then the MCMC move must be rejected in accordance with the Metropolis algorithm, that is, by setting the next state equal to the original configuration (see Section 3.4).

Due to the inherent nonlinearity of Equations (4.8), and especially in the case of very stiff chains, the numerical solver does not always succeed in finding a solution δ^* , thus leading to low acceptance rates during the simulation. (Note that $\mathcal{T}_F(\delta)$ is utilized by $\mathcal{T}_A(\Delta)$ in the search for this solution.) Below we provide a simple modification of $\mathcal{T}_F(\delta)$ that considerably increases the success rate of the numerical solver.

The efficacy of $\mathcal{T}_A(\Delta)$ depends on the success rate of the numerical solver (for example, a Newton-Raphson routine) in solving the set of d non-linear

algebraic equations involved. In some cases, such as for stiff chains, the success rate is rather low, and an improvement of the yield of the solver is desired. We can do this by subdividing δ into n equal parts, and successively applying $\mathcal{T}_F(\delta/n)$ n times. Then using, instead of $\mathcal{T}_F(\delta)$, the modification $\mathcal{T}_F^n(\delta) \equiv [\mathcal{T}_F(\delta/n)]^n$, and by increasing n , the yield of the numerical solver can be improved by as much as 10 times in some cases. However, this improvement comes at the cost of more evaluations.

The Metropolis algorithm acceptance ratio of $\mathcal{T}_A(\Delta)$ is given by

$$\alpha_{(s) \rightarrow (s+1)} = \frac{e^{-\beta \mathcal{E}(\mathbf{r}_k^{(s+1)})}}{e^{-\beta \mathcal{E}(\mathbf{r}_k^{(s)})}} \left| \frac{\partial(\mathbf{r}_1^{(s+1)}, \dots, \mathbf{r}_{N_P-1}^{(s+1)})}{\partial(\mathbf{r}_1^{(s)}, \dots, \mathbf{r}_{N_P-1}^{(s)})} \right|, \quad (4.11)$$

the last factor being the Jacobian determinant $\det(\mathbf{J}_{\mathcal{T}_A(\Delta)})$ of the transformation. Notice that we have used the fact that $\frac{\partial \mathbf{r}_0^{(s+1)}}{\partial \mathbf{r}_k^{(s)}} = \delta_{0k} \mathbf{1}_d$, where $\mathbf{1}_d$ is the $d \times d$ identity matrix and δ_{ij} is the kronecker-delta [see Eq. (4.8)], to eliminate the first three rows and columns of $\mathbf{J}_{\mathcal{T}_A(\Delta)}$ as they do not contribute to the value of the determinant. The key to computing $\mathbf{J}_{\mathcal{T}_A(\Delta)}$ lies in first differentiating Eq. (4.8) with respect to $\mathbf{r}_k^{(s)}$ and solving it to obtain:

$$\left. \frac{\partial \mathbf{r}'_0^{(s)}}{\partial \mathbf{r}_k^{(s)}} \right|_{\Delta} = \left[\mathbf{1}_d - \left. \frac{\partial \mathbf{r}'_{N_P}^{(s)}}{\partial \mathbf{r}'_0^{(s)}} \right|_{\{\mathbf{r}_j^{(s)}\}} \right]^{-1} \cdot \left. \frac{\partial \mathbf{r}'_{N_P}^{(s)}}{\partial \mathbf{r}_k^{(s)}} \right|_{\delta_0=\delta^*} + (\delta_{0k} - \delta_{N_P k}) \mathbf{1}_d$$

where both derivatives in the right-hand-side may be found by differentiating Eq. (4.10) appropriately. The other derivatives $\left. \frac{\partial \mathbf{r}'_i^{(s)}}{\partial \mathbf{r}_k^{(s)}} \right|_{\Delta}$ for $i = 1, \dots, N_P$ follow recursively from the latter equation after differentiating Eq. (4.10). Finally, one may obtain all the matrix elements of $\mathbf{J}_{\mathcal{T}_A(\Delta)}$ by differentiating Eq. (4.9) and substituting these results. The determinant itself may be computed numerically by using *LU*-decomposition which has a complexity of $O(N_P^3)$. A suitable cut-off for the number of bonds taking part in the discrete tractrix move may be chosen beforehand to suit the speed of the computer.

4.7 MCMC Simulation of Cross-linked Networks

In this section, we describe how the moves of the preceding sections enable us to simulate cross-linked networks of polymers.

The basic unit of any network is the *star* which consists of n_s linear chains that terminate at a single central node (see Figure 4.7) by means of a cross-link. Any positive integer value for n_s constitutes a star, but typically for biological networks $n_s = 4$. Without loss of generality, let us consider the 3-arm star illustrated in Figure 4.7b and assume that the ends *A*, *B*, and *C* of its arms are

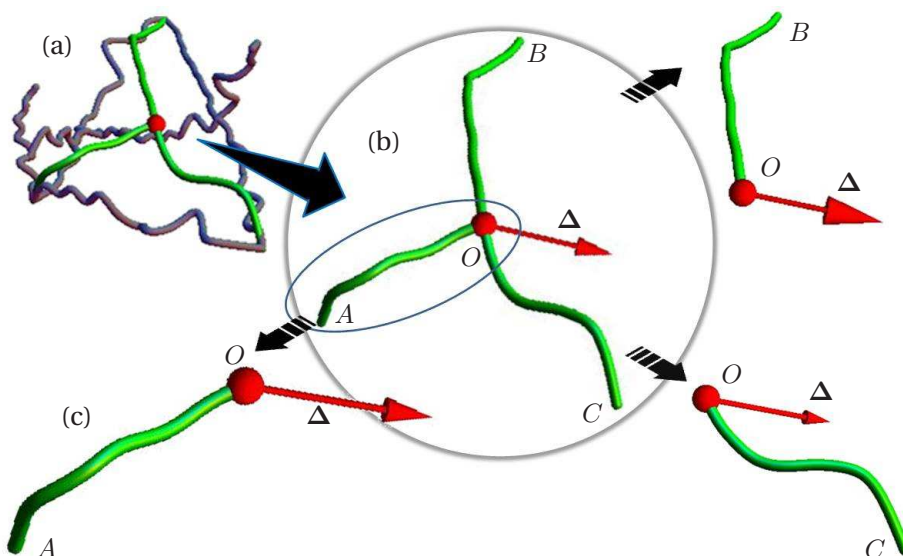


Figure 4.7: (a) Section of a network of WLC's. (b) The basic unit of a network: the star. When the central node O is displaced by a random vector Δ , each of the arms [e.g., link \overline{AO} in (c)] of the star may be treated independently.

temporarily fixed in space but that the central node O is free to move. To preserve the network connectivity at all times we must, whenever O is displaced by some vector Δ , move all the ends of the linear chains that terminate at O by the same displacement. Typically Δ is a random displacement chosen from a spherically symmetric distribution during the simulation. We may thus treat each of the linear chains independently so our focus may now narrow down to a single linear chain anchored at one end but with the other end free to move.

The problem at hand may be set forth in two parts: firstly, given the initial contour of the chain, how may we reversibly deform it so that its free end is displaced by exactly Δ ?³ Secondly, with what probability must we accept this deformation? From the preceding section, we have an answer to these two questions, namely $\mathcal{T}_A(\Delta)$ together with its acceptance ratio.

Typically, for one simulation step, a central node of a network is picked at random and displaced by Δ . The corresponding δ^* for each arm originating from the central node is numerically solved to a specified precision and $\mathcal{T}_A(\Delta)$ applied. If no solution for δ^* is found for an arm, or if the numerical solver cannot reproduce the original configuration after the inverse transformation $\mathcal{T}_A(-\Delta)$ is applied, then the entire simulation step is rejected according to the usual rules of the Metropolis Monte Carlo algorithm, otherwise the com-

³Coincidentally, this problem is equivalent to the so-called 'Inverse Kinematics Problem' which arises in robotics.

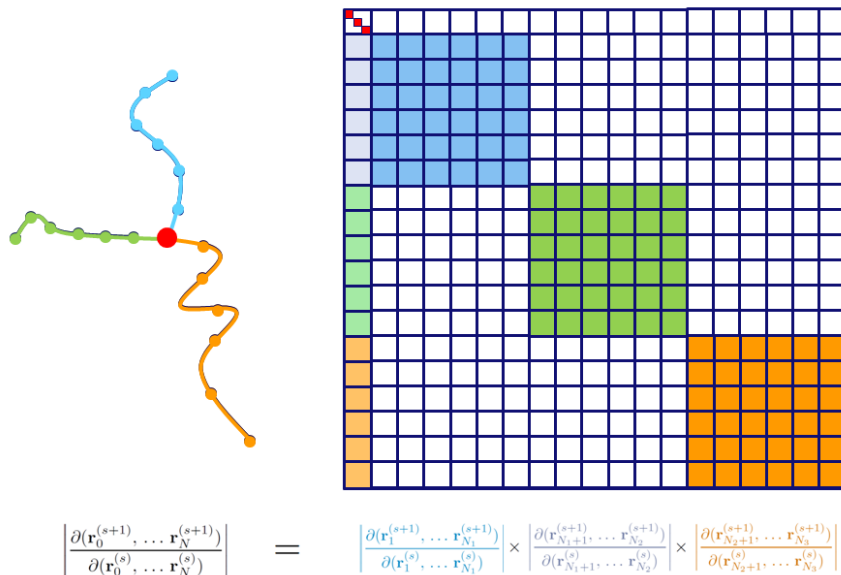


Figure 4.8: The Jacobian determinant of the move that displaces the central node of a star is the product of its arms' Jacobian determinants because the corresponding Jacobian matrix may be rearranged by means of row/column operations in a block triangular form with each block being the Jacobian matrix of one arm of the star, while the central node of the star corresponds to the d -dimensional identity matrix at the top-most and leftmost block of the Jacobian matrix.

plete acceptance ratio for the deformation of the star is found by computing its total change in energy, the product of its arms' Jacobian determinants (see Figure 4.8), and finally plugging them into Eq. (4.11). To ensure ergodicity, a few steps with random crank-shaft rotations, whose Jacobian determinants are unity, can be applied to each arm between those steps that use the discrete tractrix moves — the crank-shaft rotations will enable each linking linear chain between nodes of the network to explore more of its possible conformations as the nodes remain fixed in space, while the discrete tractrix moves will displace the nodes themselves. This is only one of the possible variations of simulation. In Chapter 6 we will outline in greater detail several other efficient variations which are based on the same mathematical formulation presented in this chapter.

The reliability of TRACTRIX is attested to by the results of tests that we performed to validate it. We applied these moves to simulate various freely-

jointed architectures with both large and small numbers of bonds. In each case, TRACTRIX reproduced the equilibrium end-to-end distance distributions in exact agreement with their theoretical predictions (see next chapter) and with near 100% acceptance rates.

Note that in all variants of TRACTRIX discussed in this chapter, there is no requirement that all the bonds should be of the same length. Nor does it mean that TRACTRIX is not useful for fluctuating bond-length simulations. Indeed, other types of moves (not used in the present work) may be included in the move set \mathcal{M} that may randomly change the bond-lengths in the system, while in turn TRACTRIX's only task is to drag and rotate them.

It is also worth noting that the techniques introduced in this chapter lend themselves well to parallelization strategies.

4.8 Trapped Entanglements

The methods described in the preceding section do not deal with the problem of entanglement prevalent in Monte Carlo simulations of polymer networks. As we shall see in Chapter 6, entanglement turns out not to be an issue for the cross-linked polymers of a collagen fibril. Nevertheless, our intention is to present a simulational method that is capable of treating the most general setting, and in this section we suggest a solution which is based on the computation of Gauss linking numbers for detecting and preventing topological inconsistencies in MCMC simulations of polymeric networks.

4.9 Topological Constraints

Perhaps the simplest way to demonstrate the issue of trapped entanglements is to consider 2 polymeric loops (shown outlined in bold in the network meshes of Figure 4.9) that start out in an entangled configuration. Classically, it is impossible for these loops to become unlinked, as in Figure 4.9, without first severing one of them.

Transverse stretching of the sample in Figure 4.9 results in the formation of a 'physical cross-link' at the intersection of the two meshes. In contrast to fixed chemical cross-links discussed in the previous chapters, these physical cross-links are able to slip along the chains during the deformation and may change their position for the next deformation. But nevertheless they are trapped and their number within the entire network is fixed unless some mesh is severed.

One advantage that MD simulations have over MCMC simulations is that with the choice of a small enough value of the time step, such issues of entanglement between polymers are dealt with in a natural way through the repulsive forces of interaction between the particles and hence one never has to worry about violating topological constraints. Thus in MD simulations the

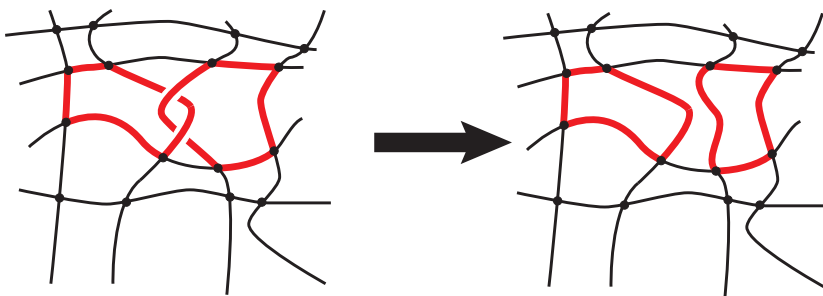


Figure 4.9: A trapped entanglement in a polymer network (*left*). A proposed MCMC move that results in the new state on the right must be disallowed since it corresponds to a physically unattainable state.

loops on the left side of Figure 4.9 will remain linked in that way throughout the duration of the simulation.

But with MCMC simulations of polymeric networks the situation is grave: for even in the presence of repulsive potentials of interaction between the particles in the system, there is no built-in way of detecting violations of topological restrictions after a move. Thus an extrinsic means of detecting, or preventing, violations of topological constraints after every MCMC step is required. Unfortunately this problem, which is the central question in the mathematical theory of knots and links, is still open having not yet been completely solved.

One suggestion for preventing violations of topological constraints would be to restrict all Monte Carlo moves to those that are equivalent to Reidemeister move types [66] when viewed in a suitably chosen planar projection of the network⁴. This approach is utilized in the Berg-Foerster-Aragao de Carvalho-Caracciolo-Froehlich (BFACF) algorithm [68, 69] for lattice polymers. We know of no similar approach for off-lattice polymers.

Other possible approaches could involve the computation of certain global quantities, namely topological invariants, such as the Gauss linking number (GLN), the Milnor invariants, Vassiliev invariants, Jones polynomial, HOMFLY polynomials, etc to distinguish between different knots or links⁵. Any two configurations of a link that have different values of a topological invariant are indeed different⁶. However, the converse is not always true: that is, two different knots may have the same value of an invariant. There is currently no known universal link invariant that completely distinguishes all knots and links. Therefore, by using any of the aforementioned invariants, some entangled states are bound to escape detection.

A common example illustrating the ambiguity one faces when using the

⁴Kauffman [67] has extended the Reidemeister moves (which were originally applicable to ring polymers) to four-fold and three-fold coordination networks.

⁵Knots refer to self-entangled loops, while links refer to entanglements between two or more

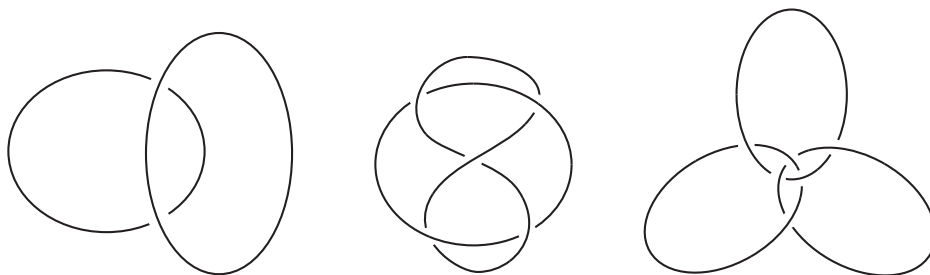


Figure 4.10: Using the GLN alone to detect trapped entanglements can lead to error: the unlink (*left*) and the Whitehead link (*middle*) have the same GLN, yet the Whitehead link is entangled while the unlink is not. The GLN for each pair of rings of the Borromean rings (*right*) is 0 yet the link cannot be undone without first severing one of the loops.

GLN as an invariant to detect entanglements is the unlink and the Whitehead link shown in Figure 4.10, which both have a GLN of zero. Another example that demonstrates the inadequacy of the GLN to reliably identify links is the Borromean rings (see Figure 4.10), which consist of three rings that are pairwise-unlinked, yet linked as a triple. Thus the GLN for any pair of rings in the Borromean link is zero. For this case, the higher-order invariant, the Milnor invariant for 3-component links generalizes the GLN to distinguish three-component links.

To make matters worse, all the aforementioned topological invariants are computationally very expensive to compute and are likely to heavily slow down the simulation when computing the invariants after every MCMC step. For instance, for the polynomial-valued invariants such as the Jones, Kauffman, and HOMFLY polynomials, the size of the memory necessary for computing them will grow exponentially with respect to the number of bonds in the link. Still we provide in this chapter an incomplete but nearly optimal solution which uses the GLN, the simplest link invariant.

4.10 Another Problem: Loop Counting

In general, it is not very difficult to see how two network meshes entangle, but it is almost impossible to count the right number of trapped entanglements as part of a network. The reason is that most meshes share chains with other meshes. These shared chains lead to multiple counting of the same entanglement. Furthermore the entanglement cannot be fixed at one chain due to its mobility along the mesh. For investigations on the effect of entanglements

loops. The components of a link may contain self-intersections

⁶In the terminology of knot theory, two equivalent links are said to be link isotopic.

during the deformation process of a polymer network and their comparison to chemical cross-links it is necessary to determine the accurate number of these entanglements and to determine their behavior during deformation [70].

4.11 The Gauss Linking Number

The GLN is a numerical invariant that describes the linking of two oriented closed curves in three-dimensional space. Intuitively, the linking number represents the number of times that each curve winds around the other. The linking number is always an integer, but it may be positive or negative depending on the orientation of the two curves. It was Edwards [55] who began to use the GLN for a better description of entanglements and topology of single polymer chains. The GLN between two oriented closed curves C_i and C_j is defined as a double line integral

$$\text{Lk}(C_i, C_j) = \frac{1}{4\pi} \oint_{C_i} \oint_{C_j} d\ell_i \times d\ell_j \cdot \frac{\ell_i - \ell_j}{|\ell_i - \ell_j|^3}, \quad (4.12)$$

where $d\ell_i$ and $d\ell_j$ are the infinitesimal elements of C_i and C_j respectively. The line integrals above are taken along the directions given by the orientation of the closed curves.

In computer simulations of polymers, loops are discretized into piecewise-linear polymeric loops $C_i = \{\mathbf{r}_m^{(i)}\}_{m=0}^{M-1}$ and $C_j = \{\mathbf{r}_n^{(j)}\}_{n=0}^{N-1}$ with M and N bonds respectively, so that the integral above is converted into the double sum:

$$\text{Lk}(C_i, C_j) = \frac{1}{4\pi} \sum_{m=0}^{M-1} \sum_{n=0}^{N-1} (\mathbf{r}_{m+1}^{(i)} - \mathbf{r}_m^{(i)}) \times (\mathbf{r}_{n+1}^{(j)} - \mathbf{r}_n^{(j)}) \cdot (\mathbf{r}_m^{(i)} - \mathbf{r}_n^{(j)}) G_{mn}^{(ij)} \quad (4.13)$$

where, for loop closure $\mathbf{r}_M^{(i)} = \mathbf{r}_0^{(i)}$ and $\mathbf{r}_N^{(j)} = \mathbf{r}_0^{(j)}$,

$$G_{mn}^{(ij)} = \int_0^1 ds \frac{2}{4a_n c_{mn}(s) - b_{mn}(s)^2} \left(\frac{2a_n + b_{mn}(s)}{\sqrt{a_n + b_{mn}(s) + c_{mn}(s)}} - \frac{b_{mn}(s)}{\sqrt{c_{mn}(s)}} \right) \quad (4.14)$$

and

$$a_n = |\mathbf{r}_n^{(j)} - \mathbf{r}_{n+1}^{(j)}|^2, \quad (4.15)$$

$$b_{mn}(s) = -2s(\mathbf{r}_m^{(i)} - \mathbf{r}_{m+1}^{(i)}) + \mathbf{r}_m^{(i)} - \mathbf{r}_n^{(j)} \cdot (\mathbf{r}_n^{(j)} - \mathbf{r}_{n+1}^{(j)}), \quad (4.16)$$

$$c_{mn}(s) = |(s(\mathbf{r}_m^{(i)} - \mathbf{r}_{m+1}^{(i)}) + \mathbf{r}_m^{(i)} - \mathbf{r}_n^{(j)})|^2. \quad (4.17)$$

The integral in Equation (4.14) can be computed numerically for every pair of linear segments between the directed curves. However, these formulae are computationally expensive to evaluate at every MCMC step, especially when

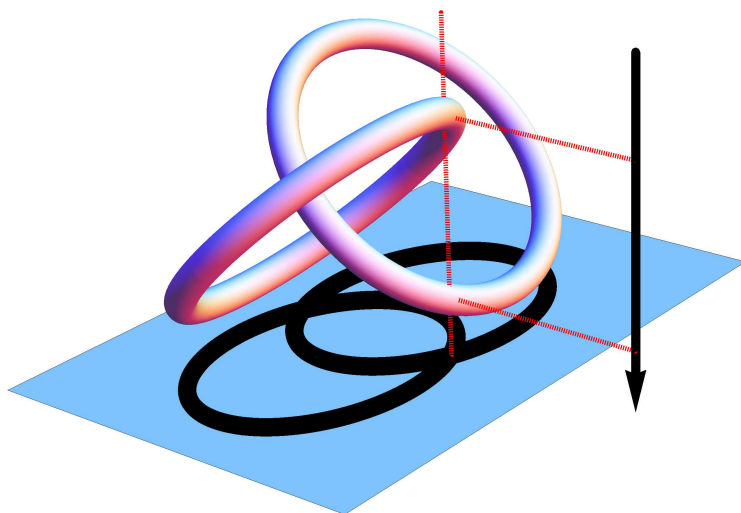


Figure 4.11: Projection of the Hopf link on a plane perpendicular to the direction \hat{u} given by the arrow. The projection is ‘good’ as it contains no double points.

the number of bonds in each polymeric loop is large. Fortunately there is a more efficient way.

The more efficient way makes use of an observation due to Hermann Karl Brunn [71], that the GLN of a link between two curves can be obtained rather easily from a ‘good’ planar projection (diagram) of the link. A planar projection of the link is obtained by first choosing a unit vector \hat{u} so that orthogonal projection of the link onto the plane perpendicular to \hat{u} gives a link diagram (see for example Figure 4.11). A good planar projection is given by a diagram whose graph has at most double points, which means that at each intersection no more than two strands cross. By an appropriate choice of the projecting vector \hat{u} , we can always select a good projection. Suppose the link has directed closed curve components \mathcal{C}_i and \mathcal{C}_j , we consider any good projection of the link and count each point at which \mathcal{C}_i crosses (over or under) \mathcal{C}_j as $+1$ if at that point the curve element that passes over the other needs to be rotated anti-clockwise to coincide with the direction of the element passing underneath it, and as -1 if at that point the curve element that passes over the other needs to be rotated clockwise to coincide with the element underneath it. The sum

of these over all crossings of C_i and C_j divided by 2 is $\text{Lk}(C_i, C_j)$. Note that the GLN is insensitive to self-intersections of a curve. This fact causes errors in the detection of entanglements (see for example Figure 4.10b).

The problem of computing the GLN of 2 piecewise-linear chains is thus reduced to the task of counting the number of signed intersections between the projected images of these curve's straight line bonds on a plane. Furthermore, for most MCMC moves, only a small portion of the entire system is deformed at each step while the rest of the system is left unchanged. Therefore one needs only to count the change in the number of crossings in the vicinity of the portion that is deformed in each step.

In computational geometry, the line segment intersection problem supplies a list of line segments in the plane and asks to determine whether any two of them cross. Naive algorithms examine each pair of segments, but for a high number of possibly intersecting segments this becomes increasingly inefficient since most pairs of segments are not anywhere close to one another in a typical configuration. The most common, more efficient way to solve this problem for a high number of segments is to use a 'sweep-line' algorithm, where we imagine a line sliding across the line segments and we track which line segments it intersects at each point in time using a dynamic data structure based on binary search trees.

The Bentley-Ottmann algorithm works by this principle to list all intersections in logarithmic time per intersection. In this work we implemented the Bentley-Ottmann algorithm described in reference [72] which is also able to deal with multiple intersections (that is, when more than two line segments pass through the same point) using data structures provided by the C++ Standard Template Library in order to count the number of signed crossings in a planar projection of the vicinity of the moved portion of the system before and after the move. By examining the coordinates of those line segments at each crossing projected onto any line parallel to the projecting vector (see for example the horizontal dashed lines in Figure 4.11), we can determine the the sign of each crossing and subsequently the change of GLN during the MCMC move for any pair of loops in the network.

4.12 Summary and Outlook

This concludes our presentation of the MCMC computational framework and the modifications and add-ons it requires to deal with the most general architectures of cross-linked Worm-Like Chains. While the entire package is difficult to implement, we demonstrate in the next Chapter that indeed this may be done, applying the TRACTRIX algorithm to simple and less simple architectures of Freely Jointed and Worm-Like Chains, which compare very well with known results in those cases that these exist, but also are capable of producing novel insights into the principles of supramolecular design in those cases

where TRACTRIX allows the first glimpses into effective mechanical behavior.

CHAPTER 5

VALIDATION OF TRACTRIX

The TRACTRIX algorithm is a crucial step towards our ambition to perform MCMC on hierarchical polymers like collagen. To test it, we have applied it to various freely-jointed and worm-like chain architectures with both large and small numbers of bonds. In each case, TRACTRIX reproduced the equilibrium end-to-end distance distributions in exact agreement with their predicted analytical results. For systems where no such results exist, we conclude this Chapter with a demonstration of TRACTRIX' proper functioning and use.

5.1 Freely-Jointed Chains

We performed simulations of freely-jointed chains using TRACTRIX. In these simulations, one end of the chain was fixed while the opposite end was displaced using TRACTRIX. Occasionally, crank-shaft moves were applied on the rest of the vertices of structure. The freely-jointed architectures simulated were a linear chain of 30 rigid bonds and the closed loop of 60 bonds. Since freely jointed structures have no energy, the acceptance ratio (see Equation (3.13)) for the MCMC moves depend only on the Jacobian determinant of the moves. Thus freely-jointed structures provide a crucial test for the validity of TRACTRIX.

Histograms of the end-to-end distance of the aforementioned structures were obtained from these simulations and their plots are given in Figure 5.1. The theoretical estimates of these curves fit exactly on these curves and are given by formulae for the end-to-end vector probability density distribution for a linear freely-jointed chain of N bonds each of length b [73]:

$$P(\mathbf{R}) = \left(\frac{3}{2\pi N b^2} \right)^{3/2} \exp \left[-\frac{3R^2}{2N b^2} \right], \quad (5.1)$$

where $R \equiv |\mathbf{R}|$.

Now the central limit theorem tells us that as the number of bonds increases, the distribution of the end-to-end distance must approach a normal distribution. So we thought it necessary to check whether TRACTRIX would also maintain its accuracy in the case of freely jointed architectures with a small number of bonds. Thus we considered three simple freely-jointed architectures with very few rigid bonds and for which the end-to-end distance distributions have exact analytical expressions. The probability density distribution of the end-to-end vector \mathbf{R} of a freely-jointed linear chain of N inextensible bonds, each of length b is [74, 73]

$$P(\mathbf{R}) = \frac{(N-1)N}{8\pi b^2 R} \sum_{t=0}^{\tau} \frac{(-1)^t}{t!(N-t)!} \left(\frac{bN-R}{2b} - t \right)^{N-2} \quad (5.2)$$

where $R = |\mathbf{R}|$, $\tau = \lfloor (Nb-R)/(2b) \rfloor$ and $\lfloor x \rfloor$ denotes the largest integer less than x .

The normalized histogram of the end-to-end distance for a linear freely-jointed chain with $N = 3$ of this structure is shown in Figure 5.2(c) which follows the theoretical prediction of Equation (5.2) (integrated over all directions in space, that is, multiplied by $4\pi R^2$) exactly, thus proving the correctness of the MCMC method particular the Jacobian determinant of TRACTRIX.

However, the power of TRACTRIX enables us to go even further: to obtain similar statistics for the 6-bond freely-jointed ring shown in Figure 5.2(b), which consists essentially of 2 linear freely-jointed chains joined end-to-end. The theoretical prediction for the probability density distribution of the separation vector between any two directly opposite ends of this ring must be equal

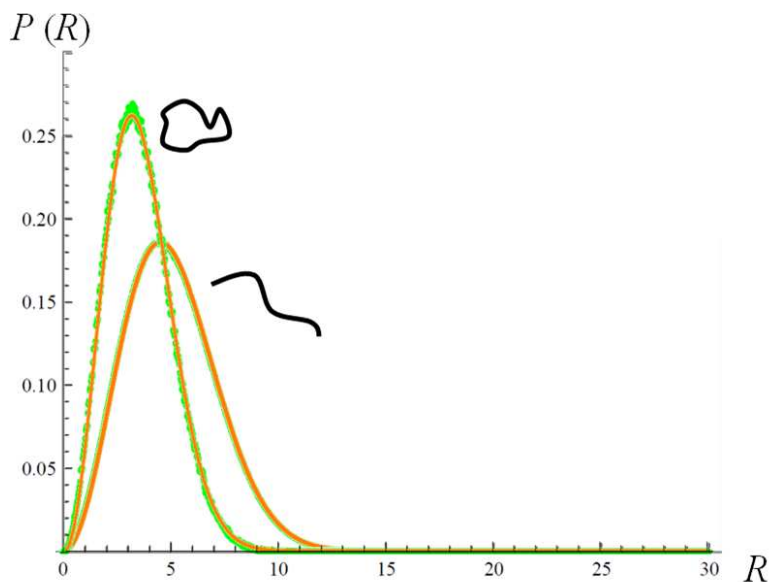


Figure 5.1: Histograms (colored green) of the end-to-end distance probability density distribution after ≈ 2 million MCMC steps for freely jointed chains: one being a linear chain of 30 bonds each of length b , and the other being a closed loop of 60 bonds each of length b . The histograms fit perfectly with their theoretical predictions (the orange curves). The prediction for the linear chain was obtained by integrating Equation (5.1) over all directions in three-dimensional space, thus obtaining $W(R) = 4\pi R^2 P(\mathbf{R})$. Likewise, the prediction for the closed loop was $W(R) = 4\pi R^2 P(\mathbf{R})^2$.

to the square of Equation (5.2). Results for the ring also follow exactly the theoretical prediction for all pairs of opposite ends of the ring, even though the TRACTRIX move was applied to only one end of the ring while its opposite end was held fixed in space throughout the simulation.

A similar procedure was followed for three linear freely-jointed chains joined end-to-end. The end-to-end distance distribution is Equation (5.2) cubed. The results of the end-to-end distance distribution are shown in Figure 5.2(c) and they also follow the theoretical prediction exactly.

5.2 Worm-like Chains and Semi-flexible polymers

An exact closed-form expression for the probability density distribution of the end-to-end vector \mathbf{R} of a worm-like chain or a semi-flexible polymer has not yet been found. Nonetheless, an asymptotic expansion for a semi-flexible

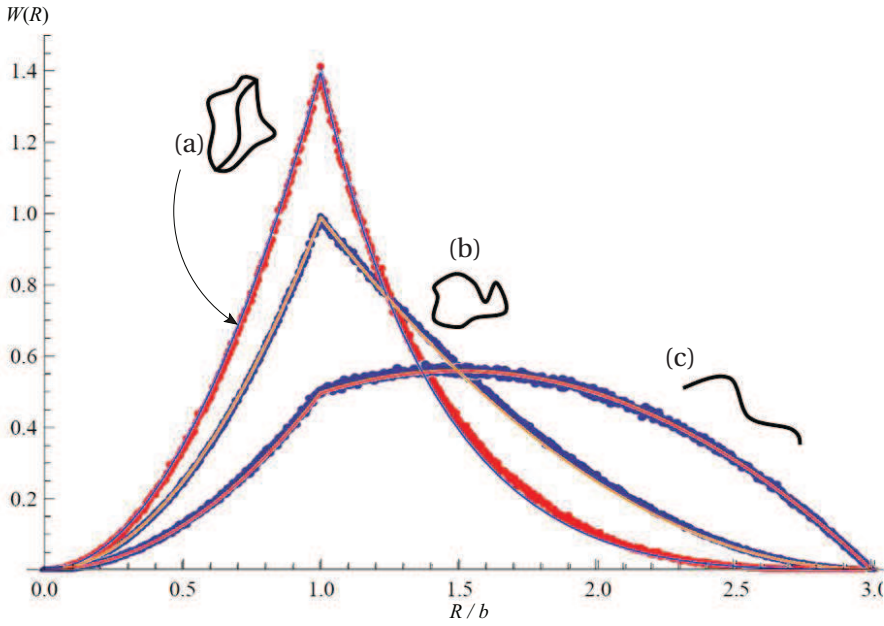


Figure 5.2: Results of the end-to-end distance probability density distributions for various freely-jointed architectures of 3-bond links after 10 million MCMC steps using TRACTRIX. The simulation points are in exact agreement with their predicted theoretical curves. LEGEND: (a) system of 3 polymers connected in parallel end-to-end, each with 3 freely-jointed bonds. (b) A six-bond freely-jointed ring. (c) A 3-bond freely-jointed linear chain. The histograms fit perfectly with their theoretical predictions (the smooth curves) [74]. The prediction for (a) was obtained by integrating Equation 5.2 over all directions in three-dimensional space, thus obtaining $W(R) = 4\pi R^2 P(\mathbf{R})$. Likewise, the prediction for (b) was $W(R) = 4\pi P(\mathbf{R})^2$, and (c) was $W(R) = 4\pi R^2 P(\mathbf{R})^3$.

polymer ($\ell_p \gtrsim \ell_c$) has been derived by Wilhelm *et al.* [32]:

$$P(\mathbf{R}) = \frac{2\ell_p}{\ell_c^2} \sum_{m=1}^{\infty} \pi^2 (-1)^{m+1} m^2 \exp\left[-\frac{\pi^2 m^2 \ell_p}{\ell_c} \left(1 - \frac{R}{\ell_c}\right)\right]$$

if $R \leq \ell_c(1 - 0.2\ell_c/\ell_p)$, (5.3)

and

$$P(\mathbf{R}) = \frac{\ell_p}{2\sqrt{\pi}\ell_c^2 \left(\frac{\ell_p(1-\frac{R}{L})}{L}\right)^{3/2}} \sum_{m=1}^{\infty} \exp\left[-\frac{\ell_c(m-\frac{1}{2})^2}{\ell_p\left(1-\frac{R}{\ell_c}\right)}\right] \left(\frac{4\ell_c(m-\frac{1}{2})^2}{\ell_p\left(1-\frac{R}{\ell_c}\right)} - 2\right) \quad \text{if } R > \ell_c(1 - 0.2\ell_c/\ell_p). \quad (5.4)$$

For a recent review of the end-to-end distributions of worm-like chains and MCMC simulations of them see for example Ref. [75].

Our own simulations of discrete worm-like chains using TRACTRIX yield curves that follow very closely with these expressions (see Figure 5.3). The discrepancies for the smaller values of ℓ_p are due to the large error in the above theoretical estimates, not TRACTRIX.

5.3 Bundles of Three Cross-linked Worm-like Chains

Figure 5.4 shows the results of simulations of various cross-linked WLC architectures, demonstrating an effect of some biological significance: cross-linked supramolecular polymers show a rising *effective* persistence length ℓ_p^* with cross-linking density n_\times . Here ℓ_p^* is defined as the persistence length of that WLC which has the same ℓ_c and expected value of the end-to-end distance $\langle r \rangle \equiv [\int dr r P(r)/(4\pi r^2)]/[\int dr P(r)/(4\pi r^2)]$ as the n_\times -cross-linked bundle [$P(r)$ denotes the end-to-end distance distribution].

Using this design motif, Nature may create supramolecular filaments of tunable effective stiffness with only two kinds of molecules at its disposal: identical chains and cross-linkers applied in varying concentrations. Note, too, that $P(r)$ of an n_\times -cross-linked bundle is *not* the same as that of a single WLC with $\ell_p = \ell_p^*(n_\times)$ — in fact, one may have to use an extensible WLC variant to capture the complete effective mechanics. Though the stiffness of a bundle in reality also depends on the cross-linkers' stiffness and size [76], we did not consider this dependence in this initial survey. Nor did we consider the effect of excluded volume interactions between chains, which would result in further stiffening each bundle while incurring the additional computational cost of having to reject all MCMC moves that cause filaments of now finite cross-section to overlap or violate topological constraints.

Extensive simulations of the collagen fibril, a supramolecular assembly of polypeptide triple helices will be reported on in Chapter 6. We emphasize that, although this work was inspired by biopolymeric structures, TRACTRIX is in fact capable of dealing with similar configuration-space constraints in much more general settings and as such may find use well beyond biological polymers.

5.4 Summary and Outlook

We have shown that TRACTRIX performs reliably, and is capable of accurately and quickly reproducing non-trivial distributions in MCMC simulations of supramolecular structures. Also, we have demonstrated how bundles of three worm-like chains may display tunable effective mechanics if the extent of cross-linking is controlled. Though it was obtained in an arguably oversimplified model system, this observation goes to the heart of our ambitions with this work in general. Given a limited set of constituents (in this case, polymers and cross-linkers) we may exploit the architecture (i.e., different arrangements of many constituents) to create a much wider range of *effective* properties. These effective properties, notably, may be much different from those of the constituents themselves. In the current chapter, we demonstrate how three WLC's linked together produce a filament that is itself semi-flexible, but in addition is extensible (contour length fluctuations of the effective, center-of-mass polymer are allowed and present). This, after much work, is not fundamentally different from the conclusions we present towards the end of this work about the collagen fibril. It, too, is a supramolecular arrangement of inextensible WLC's. It, too, is best captured by a model that is finitely extensible, but - and this is the main surprise - the effective fibril turns out to be a helical structure, whereas the constituent filaments are not: the helicity is embedded into the architecture rather than the molecules themselves. This is the central added value of the multiscale approach: we are able to let the microscopic structure speak for itself, revealing effective properties at the macroscopic/continuum scales without any bias imposed by the model adopted at the larger scale. Indeed, we shall argue this the other way around, demonstrating that the effective properties borne out by the fibril model demand continuum descriptions beyond simple linear elasticity.



Figure 5.3: Results of the end-to-end distance probability density distributions $W(R) = 4\pi R^2 P(R)$ for various worm-like chains after 10 million MCMC steps using TRACTRIX. The simulation points, which are for a 30-bond discrete worm-like chain, are in qualitative agreement with their predicted theoretical estimates [32] (see Equations (5.3) and (5.4)). KEY: from left to right, $\ell_p/\ell_c = \frac{18}{30}, \frac{21}{30}, \frac{24}{30}, \frac{27}{30}, \frac{30}{30}, \frac{33}{30}, \frac{36}{30}, \frac{39}{30}, \frac{42}{30}, \frac{45}{30}, \frac{48}{30}, \frac{51}{30}, \frac{54}{30}, \frac{57}{30}, \frac{60}{30}$. The large discrepancies between the simulation results and the theoretical predictions for the smaller values of ℓ_p/ℓ_c are expected as they are due to the inherent increase in error with a decrease in ℓ_p of the theoretical model of Ref. [32] (not the TRACTRIX method).

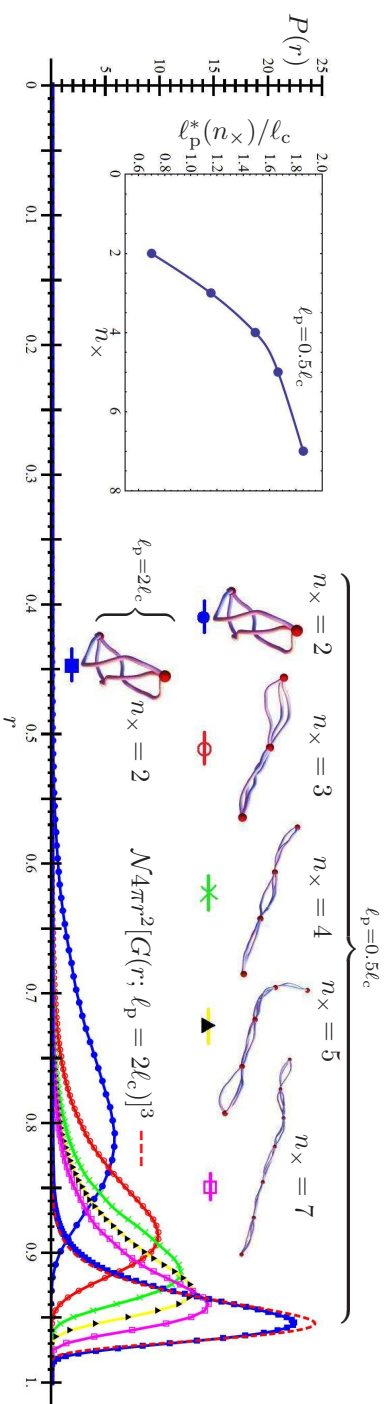


Figure 5.4: Simulation results (after $\sim 10^7$ Monte-Carlo steps): probability density distribution functions $P(r)$ for the end-to-end distance r (normalized to unity) of freely fluctuating bundles of three WLCs each with $l_p = 0.5\ell_c$ except for the last bundle which has $l_p = 2\ell_c$. Each bundle is cross-linked at equal intervals along the contour lengths of its chains. n_x is the number of cross-links in a bundle. The red dashed curve is an analytical estimate for the last bundle: $\mathcal{N}4\pi r^2 [G(r)]^3$ where $G(r)$ is the spherically symmetric radial distribution function for a stiff WLC [32] (here $l_p = 2\ell_c$), and \mathcal{N} is a normalization constant. As expected, this prediction agrees fairly well with results for bundles with $l_p \gtrsim \ell_c$. The inset shows the dependence of *effective persistence length* l_p^* (of those bundles with $l_p = 0.5\ell_c$) on n_x . Here $l_p^*(n_x)$ is defined as the persistence length of that WLC whose ends are constrained to move on a fixed straight line, and which has the same ℓ_c and expected value of the end-to-end distance $\langle r \rangle \equiv [\int dr r P(r)/(4\pi r^2)]/[\int dr P(r)/(4\pi r^2)]$ as those of the n_x -cross-linked bundle under the same constraints.

CHAPTER 6

A 3D MECHANICAL MODEL OF A FIBRIL

We propose a mesoscopic computational model for studying the mechanics of fibrils or, in general, bundles of optionally cross-linked polymers. The model offers a set of parameters whose values can be tuned to match the properties or ambient conditions of the fibril under consideration, such as the extent of cross-linking, the temperature, and the dimensions of the fibril. Although it is fairly general in its applicability, the model is discussed in the context of collagen fibrils. Monte Carlo simulation of this model is made possible by means of a recently introduced move known as `TRACTRIX` (described in Chapter 4), and we outline an adaptation of this technique for bundles of many polymers. In particular, this adaptation enables the simultaneous deformation, in one simulation step, of several polymers spanning the entire cross-section of the fibril. By subjecting our model fibril to external forces that cause it to bend, estimates of the axial Young's Modulus and axial shear modulus of collagen fibrils can be made after comparing the bent profile with a Timoshenko beam in a tip-loaded cantilever setup.

6.1 Introduction

In this chapter, we focus on the effective mechanical properties of collagen type I fibrils and how these properties are related to its dimensions, underlying structure, and intermolecular interactions. For this purpose, we propose a coarse-grained computational model that we use to simulate, and thus predict the bending response of collagen fibrils. The model is fairly general and can be modified by parameters whose values can be tuned to match certain conditions and characteristics of the fibril under consideration. Indeed, it may be applied to model bundles of various sorts, not only collagen fibrils.

By comparing the bent profile of our model fibril with a bent Timoshenko beam (a beam which is both extensible and shearable), of circular cross-section, and made up of a linear elastic solid continuum with isotropic symmetry¹, we are then able to estimate the mechanical constants of the collagen fibril, namely the axial Young's modulus and the axial shearing modulus.

As an example of its use, we put our model fibril in a tip-loaded cantilever configuration, that is, one of its ends is kept fixed while the other is subjected to a constant force perpendicular to its initial axis (see Figure 6.1). The result is of course a bent fibril.

This model can be easily adapted to study other deformation modes of fibrils, for example, twisting and stretching. Moreover, we expect this model to set the stage for incorporating the effects of different kinds of intermolecular interactions and molecular organization within the fibril.

The helical structure of tropocollagen (TC), which was introduced in Chapter 1), is an example of the ubiquitous coiled-coil motif found in biology. This structure is a source of chirality which is likely to frustrate the columnar ordering of these molecules within well-ordered crystallite domains. In our coarse-grained model we have largely ignored the effect of chirality, assuming it to be a higher order effect, and thus treating the entire TC molecule as a homogeneous, inextensible, but bendable polymer.

On its own, tropocollagen is a very flexible polymer which behaves as a worm-like chain [7, 77] at small extensions. This means that at room or physiological temperatures its bending modes are so soft that they are susceptible to thermal agitation. We may therefore assume that for the typical time duration of an applied external force a TC molecule is instantaneously excited through all its available bending modes. As such, the mechanical response of

¹A collagen fibril is more accurately described as being transversely isotropic (uniaxial), that is, it is isotropic in any plane perpendicular to the molecular axis. Hence it may be characterized by five independent elastic constants. But in fact, even transverse isotropy is also an approximation, as the crystal structure of collagen is known to possess triclinic symmetry [4]. Nonetheless, since the longest dimension of the crystal unit cell is roughly parallel to the molecular axis and furthermore is nearly perpendicular to the shorter dimensions, one is fairly justified in treating it as a transversely isotropic medium. Our bending setup, however, is able to probe only the axial shear modulus and axial Young's modulus and therefore it cannot distinguish between the different types of isotropy.

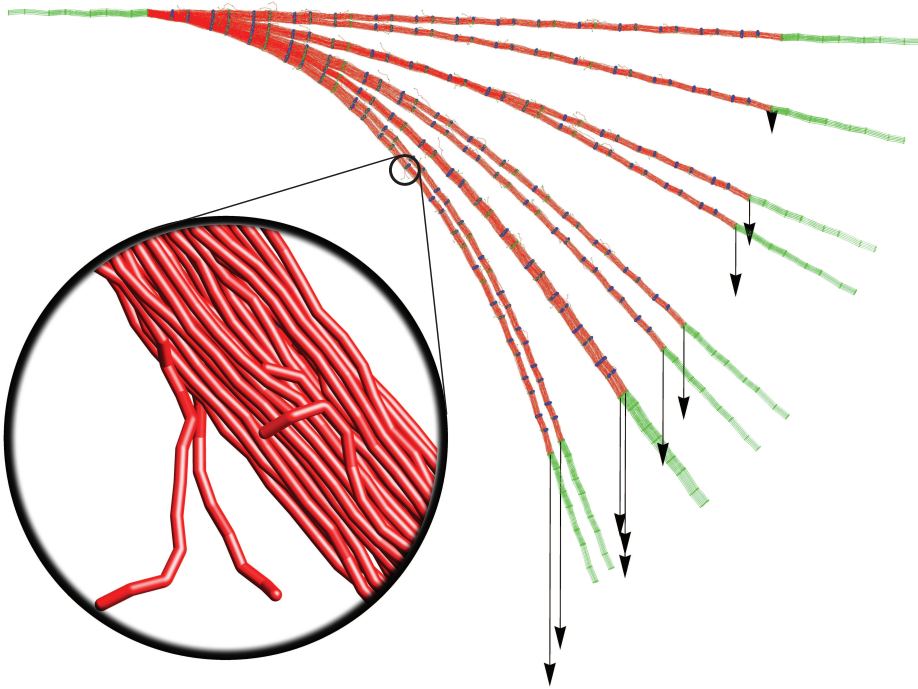


Figure 6.1: Snapshots of our model fibril early in the simulation fixed at one end (the green colored region at the top left) and subjected to progressively larger forces (denoted by the arrows) at the other end. The green colored portions are frozen during the simulation (i.e., they are not allowed to thermally fluctuate).

tropocollagen to stretching at small extensions is chiefly as a result of reduction in entropy as the thermal fluctuations of its contour line are accordingly suppressed [31]. The mechanical response however tends to be energetic near full extension as inter-atomic bonds begin to stretch, giving rise to a non-linear force-extension curve (see Figure 6.2). The persistence length of tropocollagen (Type I) in physiological conditions has been measured in laboratory pulling experiments using optical tweezers to be about 14.1 ± 7.6 nm [7]. At even higher extensions tropocollagen begins to unfold irreversibly [77]. However, we do not incorporate bond stretching or protein unfolding in the present model, since we confine ourselves to the low strain regime.

Within the fibril, a TC molecule is expected to be near full extension, though not due to tension but rather due to confinement within a narrow channel or cage formed by its surrounding neighbours whose intermolecular interactions maintain a strong lateral compression.

Despite these severe caging restrictions inside the fibril, X-ray diffraction

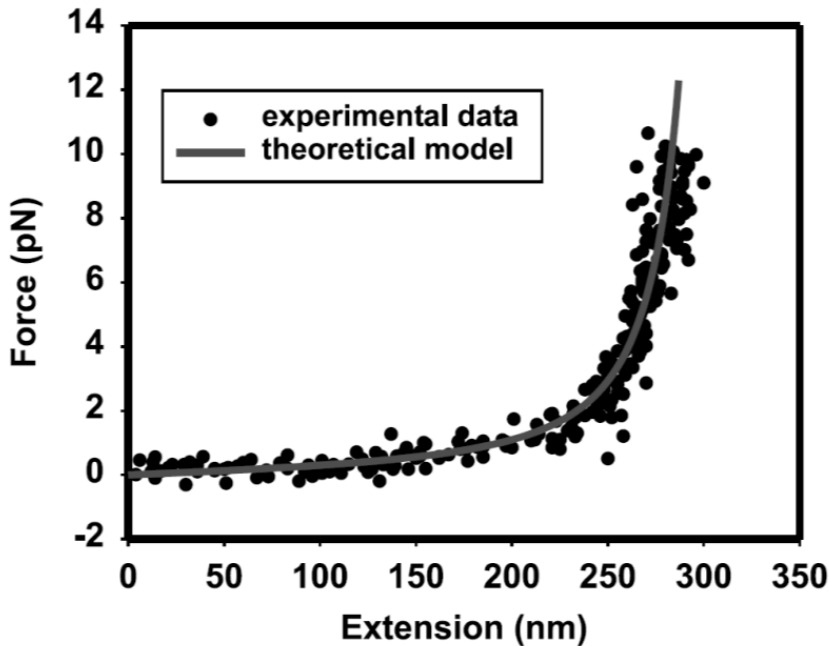


Figure 6.2: The force-extension curve for stretching a single Type I TC molecule. The data were fitted to the Marko-Siggia worm-like chain entropic elasticity model [31]. The molecule contour length and persistence length of this sample are 320 nm and 8.0 nm, respectively. (Source: Ref. [7].)

strongly suggest that there are still some spacious regions within the fibril [4], albeit very narrow, wherein we anticipate, especially considering its high flexibility, that a TC molecule will thermally fluctuate giving rise to a certain amount of entropic elasticity for the entire fibril at small strains. In the present work we perform Monte Carlo simulations to investigate such entropic contributions.

The cross-linking agents in natural collagen are not external chemical entities but are rather short non-helical chain appendices called telopeptides that occur at both ends of every TC molecule and that covalently bond via Schiff base cross-links to specific sites on the helical regions of neighboring TC molecules. These sites are not precisely known. However, a number of different sites have been implicated for cross-linking [25, 4], and the mechanics of a fibril will depend on which cross-linking mechanism is chosen.

Partially cross-linked fibrils are often described as liquid crystals, with varying amounts of well-ordered crystallite domains [78, 13], reflecting the level of disorder within the fibrils. We expect these considerations too to determine

the mechanics of the collagen fibril, and as such we input the extent and mechanism of cross-linking in our model by means of a connectivity graph which specifies the cross-links between the chains.

We also reckon that the intermolecular interactions that drive the self-assembly of TC molecules into collagen fibrils are the same as those which are responsible for the mechanical properties of collagenous tissue after formation. The possible interactions are many and there seems to be little consensus over which ones are dominant [79, 5, 80]. They include hydrophobic, hydrophilic, electrostatic, chiral, and Van der Waals interactions.

In our modeling we account for the overall and averaged effect of these intermolecular interactions with a finitely-ranged overlap potential endowed upon all coarse-grained sections of the TC molecule that are short enough to be assumed rigid (see Figure 6.4). It is an attractive, pairwise additive potential that favors the mutual alignment of neighboring TC molecules. In addition, we assign to each molecule a hardcore (infinite) potential that prevents any two TC molecules from occupying the same volume. The procedure may be *ad hoc*, but it is computationally convenient and is expected to capture the essential features of the mechanics of the fibril.

To describe the computational challenges one faces when simulating a collagen fibril using a fully atomistic description we refer the reader to the work of Gautieri et al. [81] who have performed molecular dynamics simulations of an atomistic model of a fibril using no more than 5 TC molecules surrounded by fully atomistic water molecules (57 000 atoms in all) within a simulation box with periodic boundary conditions. In doing so, they report having reached the limit of their academic computational resources (a 32-CPU parallel computer), with 6 hours per nanosecond of simulation time. Though their values for the elasticity of both wet and dry fibrils compare well with experiment, the method raises some issues. For instance, given such restrictive periodic boundary conditions, it is not possible to capture the long wavelength fluctuations or deformations within the fibril, which could be a major contributor to the elasticity of the fibril for small strains. Moreover, it is not possible with such a method to investigate finite-size effects (such as the dependence on fibril diameter and length) or surface effects which have recently been noted to be significant contributors to the elasticity of nanometer-sized biomaterials such as bone [82].

While we do not claim to have sufficiently incorporated all these effects in our model, our methodology is in accord with the ‘multiscale’ approach described by Buehler [27] which exploits an often recurring phenomenological result of soft condensed matter physics: that effective (or macroscopic) properties of a material are often the consequence of a renormalization of microscopic (that is, smaller length-scale) details; and that this renormalization tends to be independent of the microscopic details.

This work is the first stage in an attempt to determine to what extent the aforementioned phenomenological result carries over to collagen fibrils; it

paves the way for later honing in on the relevant, or dominant, microscopic contributions to collagen fibril mechanical behavior by adjusting the microscopic interactions. Here we construct a mesoscopic model of a microfibril, with fewer degrees of freedom per TC molecule than its fully atomistic version, so that the entire fibril can be simulated on modest computational resources. For instance, our model consists of more than 200 coarse-grained TC molecules (see Table 6.1), each being a discretized worm-like chain with more than 100 fluctuating rigid bonds.

Moreover, instead of MD we employ an off-lattice Markov Chain Monte Carlo (MCMC) simulation technique in a constant temperature ensemble, which is based on a recently published method for cross-linked polymers known as TRACTRIX (Chapter 4). The unique ability of TRACTRIX to offer precise control over the end-to-end displacement of any discretized linear polymer chain is what makes our simulation possible. Note that because the underlying algorithm (the Metropolis algorithm) is a non-kinetic one, we are unable to capture the real-time dynamics of the collagen fibril, but instead we aim for the fibril's long-time, or thermally equilibrated quantities.

The organization of the rest of this chapter is as follows: in Section 6.2 we describe the details of our model. In Section 6.3 we describe the MCMC technique based on TRACTRIX. There we also describe a special adaptation of TRACTRIX (the collective move) which is specially suited for fibrils. In Section 6.4, we present our results for the bending of a micrometer-sized fibril in a tip-loaded cantilever arrangement, and we compare the conformation of the fibril with that of a Timoshenko beam of the same length subjected to the same boundary conditions in order to extract its mechanical constants. In Section 6.5, our results are discussed.

6.2 The Model

Our model is specified by the sum of all free energy contributions imposed on a suitable discretization of the fibril constituents, and the graph which specifies the cross-links of the fibril. The contributing free energies are (i) the bending energy, (ii) the interaction energy, and (iii) the external work. In this section we detail these energies and describe a possible graph of the collagen fibril. These are then fed as input into our Monte Carlo algorithm which is outlined in the next section, and whose task is to compute the entropic contributions to the elasticity.

6.2.1 The Bending Energy

As mentioned in the introduction, for computational reasons, although each TC molecule (which, henceforth, we will often refer to as a TC molecule) constituting the fibril is in reality a triple-helix containing more than 30 000 atoms,

we choose to coarse-grain each one as a homogeneous discretized worm-like chain (DWLC) made up of a single linear chain of N rigid bonds, with a bending free energy specified by:

$$\mathcal{E}(\{\mathbf{t}_k\}) = -\varepsilon \sum_{i=1}^{N-1} \mathbf{t}_i \cdot \mathbf{t}_{i+1}, \quad (6.1)$$

where $\varepsilon = k_B T \ell_p / t^3$, ℓ_p is the persistence length, \mathbf{t}_i is the i -th bond (counting sequentially from one end of the polymer) of fixed length t . T is the absolute temperature and k_B is the Boltzmann constant.

This energy expression can be shown to approach the bending energy for the continuous worm-like chain in the limit of $N \rightarrow \infty$ and $t \rightarrow 0$ while keeping constant the contour length $\ell_c = Nt$ and $\varepsilon t^2 / N$. It is often sufficient to adopt a discretization that allows at least 3 bonds in one persistence length [32].²

Optionally, one may remove this fixed-length constraint and instead include a Hookean or reactive bond-stretching potential as an additional term to Equation (6.1), thus allowing the lengths of the bonds to fluctuate and respond to external forces. However, we expect these considerations to be important only in the high strain limit, in which the triple-helix begins to untwist and eventually fragment, and which we do not study in the present work. Such considerations are analogous to a similar assumption that was made when modeling double-stranded DNA (see for example Ref. [31, 33]) and which was sufficient to capture the salient features of its force-extension behaviour. This assumption is also motivated by an observation that has been reported in stress-strain experiments of collagen fibrils conducted synchronously with X-ray diffraction [84, 85]. These experiments reveal that fibril extension just before failure results in only 40% of this lengthening being a contribution from the extension of the triple-helical TC molecules. This implies that for a large part of the force-extension curve most of the TC molecules remain intact.

The contour length of a TC molecule is $\ell_c = 300$ nm, and for an isolated TC molecule in physiological conditions ℓ_p can be as short as 8 nm, making it rather flexible. Note that ℓ_p is a function of its bending modulus κ and T : $\ell_p = \kappa / k_B T$. Additional contributions to ℓ_p arise with changes in pH and the ionic strength of the ambient solvent [86, 87, 7]. Therefore ℓ_p is a parameter of the model that is set by the ambient conditions of the fibril.

In short, Equation (6.1) penalizes any non-zero angles between consecutive bonds, with an energetic cost proportional to ℓ_p and (to first order) the sum of the squares of the angles.

Recent extensive MD simulations of the full human Type I collagen triple helix [88] and X-ray diffraction studies [89] of the collagen fibril have shown

²We caution here that for worm-like chains confined inside narrow channels, which is the typical situation for TC molecules deep within a fine cylindrical fibril, a perhaps more suitable discretization should involve the so-called Odijk deflection length rather than the persistence length [83]. However, in this thesis, we have not investigated the importance of this assertion.

the TC molecule to be axially heterogenous rather than homogenous. Furthermore, mutations in the amino-acid sequence cause heterogeneity in the triple-helix and modify the conformation statistics and mechanics of the TC molecule which is believed to be the cause of various defective collagen-associated diseases, such as Ehlers-Danlos syndrome, for example. Heterogeneity is expected to reflect in a variation of the TC molecule's bending modulus (and hence persistence length) along the contour of the TC molecule. In the future, we hope to incorporate this property of heterogeneity into our model in order to investigate its effect on the mechanics of the fibril as a whole.

6.2.2 The Excluded Volume Interaction

As no two TC molecules can occupy the same volume, we endow each bond of every TC molecule with a short-ranged hardcore potential which acts to exclude all other bonds except its nearest neighboring bonds lying along the same TC molecule. The hardcore interaction is essentially a result of overlapping molecular electron orbitals referred to as Pauli repulsion (from the Pauli exclusion principle) whose origins lie deep in quantum mechanics.

Here, each bond is modeled as a hard spherocylinder of radius r and cylinder length t (see for example Figure 6.4). The radius r is the measured average diameter of the TC molecule, and is the same for all bonds of the TC molecule in accordance with the assumption of homogeneity. Note that in reality, the triple-helix is not cylindrical: the chemical side groups of its alpha chains bulge outward radially from the TC molecule axis, giving its surface a corrugated rather than smooth topography.

For wet fibrils (that is, fibrils with interstitial water molecules), the value of r may be adjusted to a larger value to reflect the thickness of the hydration layer that covers the extant hydrophilic patches on the surface of tropocollagen [80].

During the simulation, every sampled configuration of the fibril that results in the overlap of any two spherocylindrical bonds must be summarily rejected. This calls for a fast algorithm to check for bond overlaps after every proposed MCMC move. Below we describe an efficient algorithm to check for overlap between pairs of only neighboring bonds without having to check for overlap between bonds that are very far apart³.

Supposing a new position of a particular bond $\overline{P_1P_2}$ is proposed during a MCMC step. Clearly, for a large system occupying a large region of space it would be desirable to restrict the overlap tests to only the few other bonds that are nearest this given bond $\overline{P_1P_2}$ in its newly proposed position.

The three-dimensional space which contains the entire assembly of mass-points of the system can be visualized as being tessellated into a grid of cubes each with edges of length Δh which are parallel to the Cartesian axes x , y , and z . Each cube of the grid is indexed by a unique tuple of three integers (l, m, n) ,

³A slightly different algorithm can found in Ref. [90].

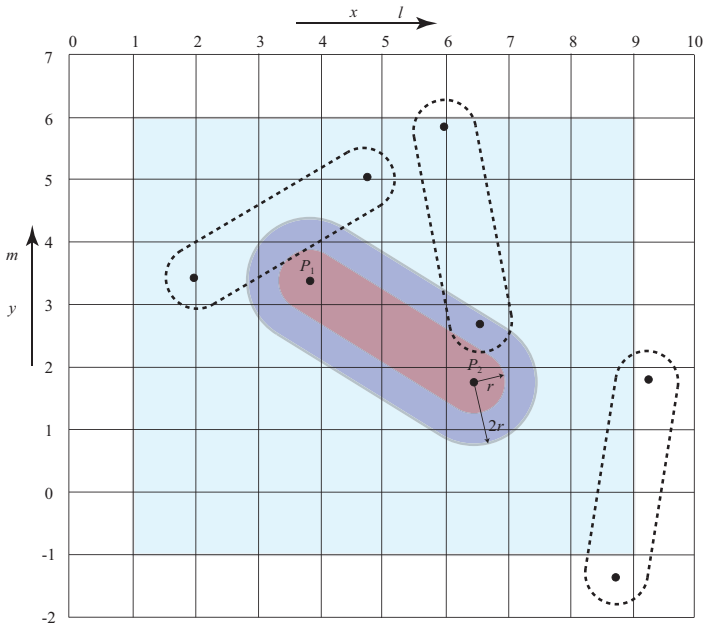


Figure 6.3: Two-dimensional representation of a spherocylindrical bond $\overline{P_1P_2}$ of radius r of a TC molecule (here shown isolated from its neighbouring bonds on the same TC molecule) in the xy -plane (or in the lm -grid) and in its newly proposed position. The spherocylindrical region of radius $2r$ (colored in blue) surrounding this bond denotes that region of space where it is absolutely necessary to test for the presence of other spherocylindrical bonds that will overlap with bond $\overline{P_1P_2}$. However, to identify these overlapping bonds, the algorithm will test for overlap of all the spherocylindrical bonds whose mass-points lie within the light-blue colored rectangular region enclosing the bond $\overline{P_1P_2}$. The entire region outside this shaded region need not be included in the overlap test, thus effectively reducing the time required for overlap testing.

while each mass-point (here, a mass-point is defined as any end of a chosen bond. For instance P_1 is a mass point of bond $\overline{P_1P_2}$.) is indexed by an integer i . The cube (l, m, n) in which a given mass-point P_i with position coordinate $\mathbf{r}_i = (x_i, y_i, z_i)$ is located can always be determined from the coordinates of P_i through the following formulae: $l = \lfloor x_i/\Delta h \rfloor$, $m = \lfloor y_i/\Delta h \rfloor$, and $n = \lfloor z_i/\Delta h \rfloor$, where $\lfloor x \rfloor$ represents the greatest integer less than x .

In computer memory, an array \mathcal{A} of lists, each indexed by the same integer tuples (l, m, n) as the grid-cubes, can be maintained with each list containing the indices i of all mass-points P_i located inside its corresponding grid-cube. Therefore during the simulation, whenever any mass-point actually changes its position the relevant lists in \mathcal{A} must be promptly updated to reflect the change.

With the aforementioned scheme in place, clearly any given spherocylindrical bond $\overline{P_i P_j}$, with hemispherical cap centers of radius r coinciding with mass-points P_i and P_j , can overlap only with those other spherocylindrical bonds with hemispherical cap centers located in cubes with indices (l, m, n) within the following ranges:

$$\begin{aligned} \min(x_i - 2r - t/2, x_j - 2r - t/2) &\leq l \leq \max(x_i + 2r + t/2, x_j + 2r + t/2), \\ \min(y_i - 2r - t/2, y_j - 2r - t/2) &\leq m \leq \max(y_i + 2r + t/2, y_j + 2r + t/2), \text{ and} \\ \min(z_i - 2r - t/2, z_j - 2r - t/2) &\leq n \leq \max(z_i + 2r + t/2, z_j + 2r + t/2), \end{aligned}$$

where $t = |\overline{P_i P_j}|$ is the length of the bond. Hence the bond-overlap tests need only be restricted to only those bonds found in these cubes (See Figure 6.3).

The width Δh of the grid-cube may be chosen to be $2r$. Note that the smaller Δh is, the more computer memory is needed to store the array \mathcal{A} . On the other hand, the larger Δh is, the more unnecessary bond-overlap tests will be made that slow down the simulation.

Our implementation for the test for overlap itself between a pair of neighbouring spherocylindrical bonds of radius r involves finding the length a of the shortest line segment linking their (hemispherical cap) center-to-center axis-segments and comparing it to $2r$. If $a < 2r$ then the two bonds overlap, otherwise they do not. A fast algorithm to find a has been outlined in Ref. [91] which is essentially the same as ours.

6.2.3 The Attractive Interactions

The thermal stability of the fibril is due to many energetic and entropic influences also involving the solvent in which the TC molecules are immersed. These interactions are not completely understood [79, 8]. Nonetheless, the result of all these influences is a generally attractive and mutually-aligning interaction between TC molecules which drives the self-assembly of the fibril, maintains its high aspect-ratio shape, and contributes to its mechanical properties.

A variety of intermolecular interactions have been tagged to drive the self-assembly of collagen TC molecules into fibrils, and could therefore provide the required aligning effect between TC molecules. These include hydrophobic, hydrophilic (via hydrogen bonding), electrostatic solvation (including dipolar) [92, 93, 94], achiral dispersion (van der Waals) and chiral dispersion interactions.

A complete treatment of all intermolecular interactions would involve an extremely computationally expensive summation over all pairs of atoms making up the different triple-helices and solvent water molecules. Note that there are more than 30 000 atoms in a TC molecule. To make matters even worse, some of these interactions are not pairwise-additive in general, nor do they

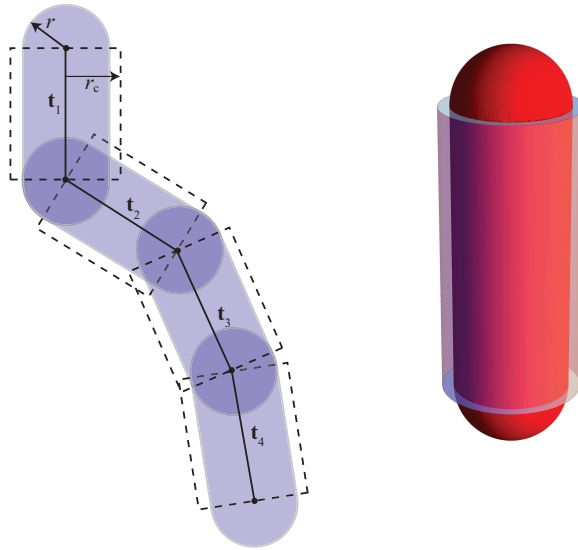


Figure 6.4: (Left) The spherocylindrical excluded-volume regions surrounding a planar 4-bond TC molecule backbone $\mathbf{t}_1, \mathbf{t}_2, \mathbf{t}_3, \mathbf{t}_4$. The dashed rectangles outline the cylindrical region used to compute the overlap potential energies. (Right) A three-dimensional rendering of one bond isolated from the rest of the TC molecule.

act within spatial ranges⁴.

For this reason, our approach is somewhat *ad hoc*: we choose to circumvent all these issues by endowing each bond with an *effective* TC molecule-aligning, achiral, pairwise-additive, and attractive overlap potential which is of finite range, and acting within a specified cutoff distance r_c from the axis of each bond. The precise implementation is as follows: a cylindrical region concentric with the spherocylindrical bond and of the same cylindrical height as the spherocylinder, but of radius $r_c > r$, is defined (see Figure 6.4) so that the potential energy of attraction between any pair of bonds, \mathbf{t}_i and \mathbf{t}_j , is taken to be a constant $-v_A$ multiplied by the volume of overlap $V_{O_{ij}}$ between the cylinders surrounding the two bonds:

$$\mathcal{V}(\mathbf{t}_i, \mathbf{t}_j) = -v_A V_{O_{ij}}. \quad (6.2)$$

The total interaction energy of the fibril is then the sum of $\mathcal{V}(\mathbf{t}_i, \mathbf{t}_j)$ over all neighboring bond-pairs \mathbf{t}_i and \mathbf{t}_j , except pairs of nearest consecutive bonds that lie along the same TC molecule. v_A is here called the cohesive energy density whose (positive) value can be adjusted so that a fine slender fibril is

⁴For the simpler case of the computation of the thermal stability of a short tropocollagen-like fragment with length only 1/30-th of the full triple-helix, which takes over 80 hours of computations, taking into account quantum mechanical considerations, see for example Refs. [95, 96].

maintained. The same grid-scheme described in the previous subsection for testing for overlap between neighbouring pairs of bonds may also be used to determine which pairs of bonds need to be considered when computing their overlap volumes.

In Section 6.4, we demonstrate how we arrive at the specific value of v_A which we use in our simulations. The parameter r_c is called the ‘cohesive distance’, whose value may be suitably adjusted. Equation 6.2 is reminiscent of the Asakura-Oosawa depletion interaction potential [97] between hard-particles in a solution of penetrable spheres. Recently, the depletion interaction has been implicated as a driving mechanism for protein assembly [98, 99] and also the onset of helical formation of filamentous proteins [100, 98, 99] in crowded environments. It has also been suggested as a surrogate for the hydrophobic interaction [98, 100]. This is because both the depletion attraction and hydrophobic effect [101] tend to minimize the surface area exposed to the solvent. They are also superficially similar in that one is purely, and the other mainly, driven by entropic effects. However, an increase in free volume available to a macromolecular solute drives the depletion attraction, whereas an increase in hydrogen-bonding states available to water underlies the hydrophobic effect [101]. Indeed, if r_c is only slightly larger than r , the overlap volume $V_{O_{ij}}$ becomes roughly proportional to the solvent-*inaccessible* surface area of the TC molecules, and then $\mathcal{V}(\mathbf{t}_i, \mathbf{t}_j)$ approximates the hydrophobic-like interaction of bonds whose entire surfaces are hydrophobic.⁵

An analytical expression for the volume of overlap between two infinite cylinders each of radius r with minimum distance $\ell < 2r$ between their axes, and angle θ (a non-integral multiple of π) between their axes can be determined analytically by integration and is given by:

$$V_{OV}(\ell, \theta, r) = \frac{4}{\sin \theta} \int_{\ell-r}^r dx \sqrt{r^2 - x^2} \sqrt{r^2 - (\ell - x)^2} = \frac{2\sqrt{4r^2 - \ell^2}}{3 \sin \theta} \left[(\ell^2 + 4r^2) E \left(\arcsin \frac{\sqrt{4r^2 - \ell^2}}{2r} \middle| \frac{4r^2}{4r^2 - \ell^2} \right) - \ell^2 F \left(\arcsin \frac{\sqrt{4r^2 - \ell^2}}{2r} \middle| \frac{4r^2}{4r^2 - \ell^2} \right) \right], \quad (6.3)$$

where $E(*|*)$ is the elliptic integral of the second kind and $F(*|*)$ is the elliptic integral of the first kind.⁶ We know of no similar formula for finite cylinders. But for $\theta = 0$, that is, for two parallel cylinders of finite length s and with axes

⁵Another kind of overlap potential, but which is long-ranged, namely the Gay-Berne overlap potential [102], is often used in modeling the Van der Waals interactions between axial molecules such as in simulations of liquid-crystal mesogens.

⁶The integration was performed using Mathematica®.

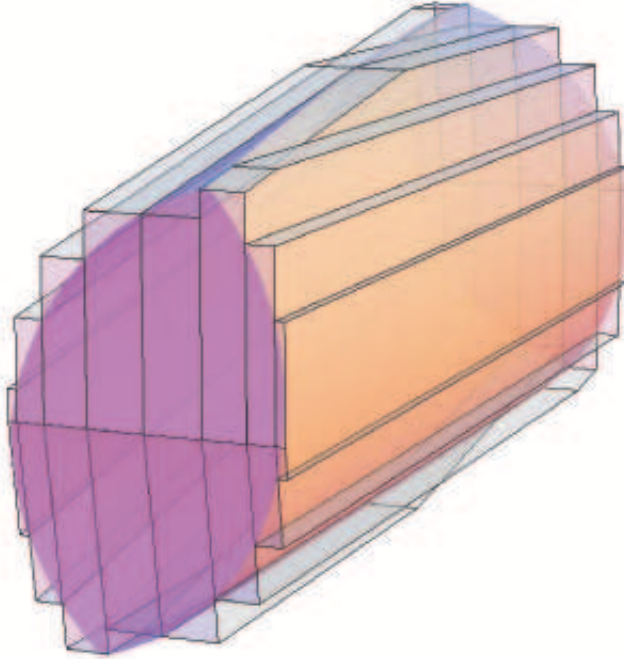


Figure 6.5: A stack of 8 prisms whose polygonal bases bound the overlap region between two finite non-parallel cylinders (not fully shown here for the sake of clarity). The total volume of these prisms approximates the volume of the overlap region it encloses.

a distance ℓ apart, the overlap volume is

$$V_{\text{OV}}(\ell, 0, r, s) = s \left(2r^2 \arccos \frac{\ell}{2r} - r\ell \sqrt{1 - \left(\frac{\ell}{2r} \right)^2} \right). \quad (6.4)$$

The volume $V_{\text{ov}_{ij}}$ of overlap between two arbitrarily oriented *finite* cylinders \mathcal{C}_i and \mathcal{C}_j can be quickly estimated numerically by the sum $V_{\text{ov}_{ij}}^{(n)}$ of the volumes of a parallel stack of n prisms constructed to bound the overlap region (see Figure 6.5), and whose polygonal cross-sections are perpendicular to the shortest line segment joining the extended axes of the two cylinders. The reader may recognize from the figure that the method mentioned above for approximating the overlap volume is actually a one-dimensional Lebesgue summation along the shortest line segment \mathcal{S} joining the two (extended) axes of the cylinders.

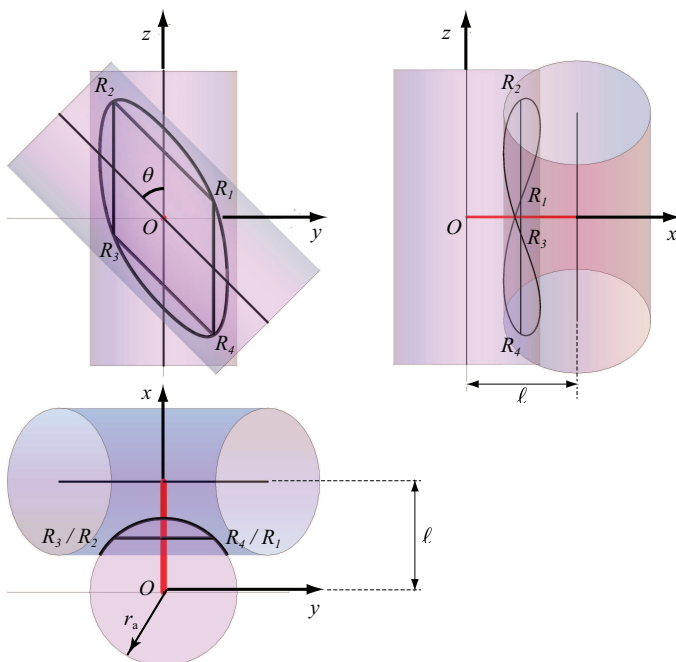


Figure 6.6: Three orthogonal views of the overlap region between two non-parallel cylinders of radius r_c : the border of the overlap region is formed by the edges of all parallelograms (for example $R_1R_2R_3R_4$) formed by the intersection of contours, or level sets $x = \text{constant}$ on the surfaces of both cylinders. The red line is the shortest line segment S joining the two (extended) axes of the cylinders. The length of S is ℓ .

Let us for the moment consider two intersecting non-parallel cylinders of infinite length. Then each of the prisms has a base Q_k in the shape of a parallelogram whose edges lie on the surfaces of both cylinders, but whose plane is perpendicular to S (see Figure 6.6). If S is along the x -axis, and the axis of C_i along the z -axis, while the axis of C_j lies in the plane $x = \ell$ (ℓ being the length of S), then the position vectors of the vertices R_{1k} , R_{2k} , R_{3k} , and R_{4k} of Q_k are given respectively by:

$$\begin{aligned} & (x_k, \quad y_1(x_k), \quad -y_1(x_k) \cot(\theta) - y_2(x_k) \csc(\theta)), \\ & (x_k, \quad y_1(x_k), \quad -y_1(x_k) \cot(\theta) + y_2(x_k) \csc(\theta)), \\ & (x_k, \quad -y_1(x_k), \quad y_1(x_k) \cot(\theta) + y_2(x_k) \csc(\theta)), \text{ and} \\ & (x_k, \quad -y_1(x_k), \quad y_1(x_k) \cot(\theta) - y_2(x_k) \csc(\theta)), \end{aligned}$$

where $0 \leq x_k \leq \ell$, $k = 0, 1, \dots, n$, $y_1(x) = \sqrt{r_c^2 - x^2}$, $y_2(x) = \sqrt{r_c^2 - (\ell - x)^2}$, and θ is the angle between the axes of the cylinders as seen when viewing them along S .

However, for finite cylinders, one needs to find the intersections of these parallelograms with the cylinders' planar caps. This leads, in general, to truncated parallelograms. C++ codes that implement these procedures and then go on to compute the areas of these truncated parallelograms and the volumes of their corresponding prisms, can be found in the supplementary material [65].

In the limit of n going to infinity, $V_{\text{ov}_{ij}}^{(n)}$ approaches $V_{\text{ov}_{ij}}$. Unfortunately, a large value of n will mean too much CPU time will be spent computing $V_{\text{ov}_{ij}}^{(n)}$. Luckily, a shortcut can be exploited here: because the radius r_c of the cylindrical region representing the attractive potential range is often only a little larger than the radius r of the hardcore spherocylindrical region, the axes of the cylinders never come very close together, and the overlap region thus remains thin. In such circumstances n can be chosen to be quite small. In which case, $V_{\text{ov}_{ij}} \approx \alpha_n V_{\text{ov}_{ij}}^{(n)}$, where α_n is a constant scaling factor that will need to be determined before the start of the simulation. Thus for example, when $r_c = 1.5r$, then $n = 4$ with $\alpha_4 = 0.86$ is enough to obtain values of the overlap volume close to $V_{\text{ov}_{ij}}$ for almost all positions and orientations of C_i and C_j , as evidenced by the plots of Figure 6.7.

Our choice of the attractive interaction potential and excluded volume interaction enables sliding of neighbouring TC molecules relative to each other with a negligible shear force. This picture may not be an entirely faithful representation, as in reality there also exist electrostatic bonds, direct hydrogen bonds, and hydrogen-bonded water-bridging molecules, between the atoms of neighbouring TC molecules [80]. Therefore, whenever any two TC molecules slide past each other along a certain distance, all these bonds would have to be first stretched, or if the sliding force is large enough, they would have to be broken and new ones formed in their place. Beuhler [27] has postulated that these effects would give rise to a resistive shear force between TC molecules that, for small shear forces, would be proportional to the length of the contact line between the molecules and would act uniformly along the entire contact line. But for large shear forces, they would lead to the propagation of slip pulses which is due to the localized breaking of intermolecular bonds, and which evolves in a manner akin to the propagation of cracks in bulk materials. Our intention in this work, however, is to assume that the effect of shear (due to these non-covalent cross-links) between nearest neighbouring TC molecules is negligible. So these additional contributions have been neglected. In the next section, however, we introduce freely-jointed covalent cross-links which prevent neighbouring TC molecules from sliding off completely past each other.

Furthermore, in the present work, despite the intrinsic chirality of the TC molecules, we do not study the effect of their chirality on collagen fibril mechanics. But we suggest that the simplest means to include an effective chiral interaction between TC molecules, without introducing any more degrees of freedom, is to add the following term to the interaction between any two

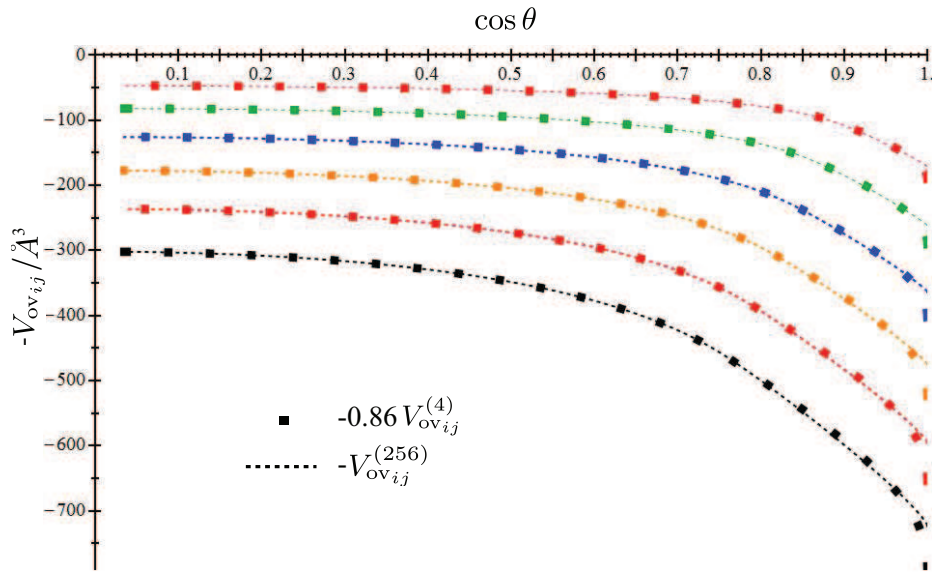


Figure 6.7: A plot of the negative of the overlap volume $V_{ov_{ij}}$ between two cylinders of radius $r_a = 0.7$ nm and height $h = 3.80952r_a$ versus $\cos \theta$, for $\ell/r_a = 1.42857, 1.5, 1.57143, 1.64286, 1.71429, 1.78571$ (counting upwards from the lowest curve). Here the shortest line segment S joining the cylinders' (extended) axes also joins their geometric centers. For this range of ℓ , $V_{ov_{ij}} \approx V_{ov_{ij}}^{(n)}$ for $n \geq 32$. It is evident from the plot that if $n = 4$ is chosen, then one need only multiply $V_{ov_{ij}}^{(4)}$ by the scale factor 0.86 to obtain a good estimate for the overlap volume for almost all values of θ and for all ℓ in the given range. Similar results (not shown here) also hold even when the ends of S are offset from the cylinders' geometrical centers.

bonds, \mathbf{t}_i and \mathbf{t}_j [103, 104, 105]:

$$\mathcal{U}(\mathbf{t}_i, \mathbf{t}_j) = u_C (\mathbf{t}_i \times \mathbf{t}_j \cdot \hat{\mathbf{r}}_{ij}) (\mathbf{t}_i \cdot \mathbf{t}_j), \quad (6.5)$$

which is allowed to act only when the achiral attractive overlap potential introduced previously (in Equation (6.2)) between the same two bonds is nonzero. Here $\hat{\mathbf{r}}_{ij}$ is the center-to-center displacement unit vector of bond \mathbf{t}_i relative to bond \mathbf{t}_j , and u_C is a chiral strength parameter whose (negative or positive) value can be adjusted to produce mutual twist between two TC molecules. This form of chiral interaction has been successfully used in simulating chiral liquid crystals to obtain cholesteric phases [103]. It has its origins in second-order perturbation theory of quantum mechanics for the coulombic interaction between two axial molecules. The total chiral interaction energy of the fibril would then be the sum of $\mathcal{U}(\mathbf{t}_i, \mathbf{t}_j)$ over all neighboring bond-pairs \mathbf{t}_i and \mathbf{t}_j (except pairs of nearest consecutive bonds that lie along the same TC molecule).

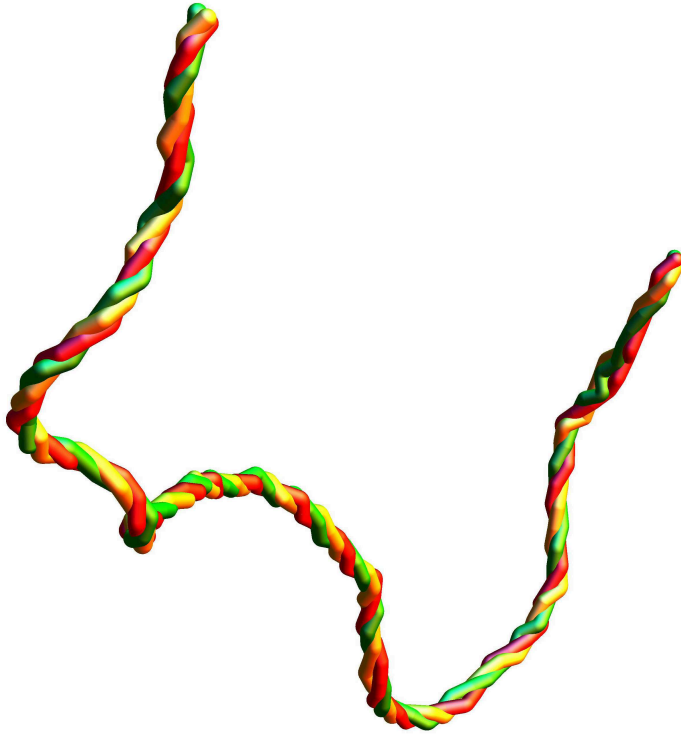


Figure 6.8: Qualitative demonstration of all the free energy contributions, except those of external forces. Bending, excluded volume, attractive, and chiral interactions in a Monte Carlo simulation of three polymers that initially started out as being parallel to each other produces an equilibrium state that looks like a triple-helical bundle.

As a qualitative demonstration of the effectiveness of all the different energies detailed so far (namely bending, hard-core, achiral attractive, and chiral interactions), in Figure 6.8 we show a Monte Carlo simulation snapshot three discrete worm-like chains, each with a 100 bonds, and which were initially arranged parallel to each other, but which later during the simulation settled into the triple-helical state shown. The figure is reminiscent of bundles of chiral polymers [106]. We hope to elaborate further on these findings in future work.

6.2.4 The External Work

The change in free energy due to an external force, or traction, \mathbf{f}_k acting on a selected mass-point P_k near the boundary of the fibril is taken to be the work done by this force during a displacement $\Delta\mathbf{r}_k$ of P_k . Thus, in the spirit of the

principle of virtual work, we construct the total work done by all such forces as

$$\mathcal{W} = - \sum_k \mathbf{f}_k \cdot \Delta \mathbf{r}_k. \quad (6.6)$$

The set of external forces and the mass-points upon which they act can be specified at the start of the simulation with the intent of producing a particular deformation profile, such as a bent or stretched profile. A similar expression can be constructed for external torques exerted on the fibril, which can be used to produce a twisted profile of the fibril.

6.2.5 Cross-linking: The Connectivity Graph

In a collagen fibril, a TC molecule may be covalently cross-linked to another TC molecule, which in turn is cross-linked to another, and so on. These are the so-called Schiff base cross-links [8]. Natural cross-linking is achieved by the TC molecules themselves: each of their ends possess short non-helical chain appendages (called the N- and C-terminal telopeptides) about 1% of the full length of a TC molecule, which bond covalently to specific sites on the helical regions of neighboring TC molecules. One end of the TC molecule, the C-terminus, provides one telopeptide for cross-linking. The other end of the TC molecule, the N-terminus, provides two telopeptides for cross-linking. Thus, there is a maximum number of natural cross-links any fibril might have. This aspect of cross-linking is unlike in some other biofilaments where cross-linking is achieved through foreign cross-linking agents (for example, α -actinin for filamentous actin [107]) which attach themselves to the biofilaments at some random sites along their contour, so that cross-linking can be controlled externally by adjusting the concentration of the cross-linking agents. Instead, for collagen, an enzyme, known as lysyl oxidase, may be used to induce cross-linking between TC molecules. Some cross-links start out as divalent (linking a pair of TC molecules) and then upon further maturation of the fibril react further with TC molecules in register from an adjacent fiber forming stable trivalent cross-links (linking a triple of TC molecules) and further increasing its mechanical strength.

The precise cross-linking sites on the helical region of the TC molecule are unknown. However, a number of different cross-linking sites have been implicated by researchers [25, 4]. The extent and manner of cross-linking can be fed as input into our simulation by means of a graph. We choose the following scheme, based on an analysis of the proximity of TC molecules within the crystal structure given in Ref. [4] (also shown in Figure 6.9): the sites along the collagen TC molecule where cross-linking are thought to occur are shown in Fig. 6.10. The numbers at the sites denote the distances (in units of $D = 67$ nm) of the sites from the left end 0 of the TC molecule. The arrows denote the “direction” of cross-linking. For example, the end 0 has two branches that can

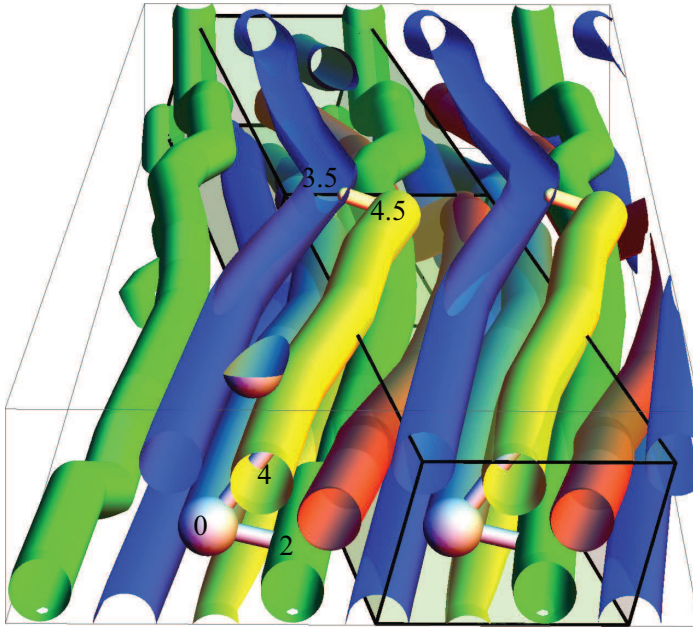


Figure 6.9: The triclinic crystallographic unit cell of the collagen fibril, due to Orgel *et al.* [4], embedded in a slab of crystalline collagen fibril containing specific sections of TC molecules here represented by the colored tubes. An entire fibril can be generated by periodically repeating this unit cell. The cross-links are here represented by the thin cylinders inter-linking the TC molecules. The cross-linking mechanism illustrated here is slightly different from that of Figure 6.10 since here 4.5 links 3.5 (instead of 0.5 in Figure 6.10).

attach to sites 2 and 4 on other TC molecules, while the end 4.5 can attach to site 0.5 on yet another TC molecule. Conversely, the sites 0.5, 2 and 4 on this TC molecule can receive attachments from the ends of other TC molecules (4.5, 0 and 0 respectively). Thus a collagen TC molecule may be linked to 6 other collagen TC molecules.

In this thesis, we modeled each interlinking telopeptide as a rigid link emanating from the end of a TC molecule and terminating at its respective cross-linking site on the neighboring TC molecule. During the simulation, each cross-link was treated as being freely-jointed with its interlinking TC molecules.

6.2.6 Preparing the Fibril's Initial State

Before the simulation, the initial fibril was constructed such that all TC molecules took up their respective positions within a perfectly crystalline

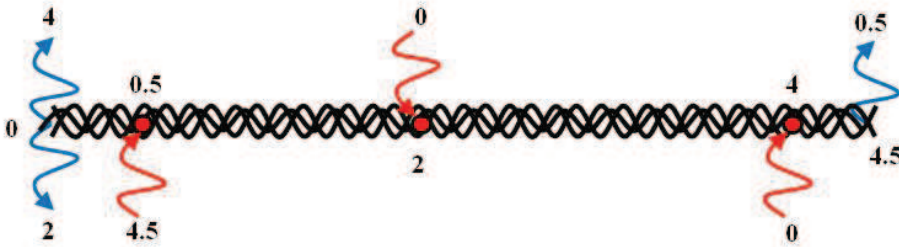


Figure 6.10: The precise cross-linking sites on the helical region of a TC molecule are unknown. Here we outline a possible cross-linking mechanism for the collagen TC molecule, based on an analysis of the proximity of TC molecules in the three-dimensional crystal structure of Ref. [4] also shown in Figure 6.9. The numbers at the sites denote the distances (in units of $D = 67$ nm) of the sites from the left end 0 of the TC molecule. The arrows denote the “direction” of cross-linking of the telopeptides. For example, the end 0 (the N-terminus) of the TC molecule has two branches that can link to sites 2 and 4 on neighbouring TC molecules, while the end 4.5 (the C-terminus) can link to site 0.5 on yet another TC molecule. Conversely, the sites 0.5, 2 and 4 on this TC molecule can receive links from the termini of other TC molecules (4.5, 0 and 0 respectively). Thus a collagen TC molecule may be linked to 6 other collagen TC molecules in a fully cross-linked fibril.

fibril⁷ along contours that threaded parallel arrays of equidistant two-dimensional hexagonal lattice planes (see Fig. 6.11), with inter-stack distances and hexagonal lattice parameter $a_H \approx 15$ nm determined from the crystal unit cell in Ref. [4] (see Figure 6.12). The entire fibril was constructed by generating, one by one, many identical copies of one TC molecule in the molecular configuration shown in Figure 6.12B. We began with a single TC molecule placed at a lattice site, and then kept adding (recursively) an identical copy at neighbouring lattice sites, always ensuring that each added copy was cross-linked with one or more already placed TC molecules, according to the cross-linking scheme outlined in Figure 6.10. We did this with the intention of making the entire fibril one fully percolated (connected) cluster before the start of the simulation⁸.

⁷X-ray diffraction images of the collagen fibril show a significant amount of diffuse scatter (see, for example, Figure 1.2) indicating that the fibril contains disordered regions. A disordered lateral arrangement of TC molecules [13, 108, 109, 16] within the fibril is thought to be the main cause of this diffuse scatter. In this work, only the starting configuration of the fibril is taken to be perfectly crystalline. Then, during the simulation itself, this structure is allowed to thermally relax to a less ordered state.

⁸In this thesis, we placed cross-links between TC molecules wherever admissible according to the prescribed cross-linking scheme. However, for investigations of the effect of the extent of cross-linking on the mechanics of the fibril, one might instead opt to eliminate each cross-link with

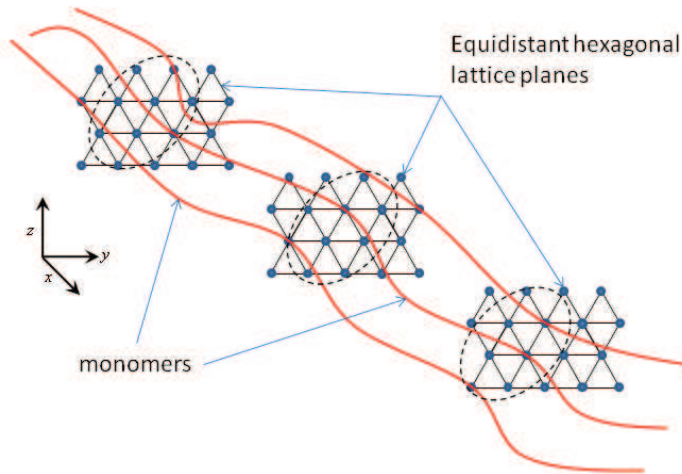


Figure 6.11: Constructing the initial state: collagen TC molecules thread a stack of hexagonal lattices planes. The exact positions of the sites they pass through are determined by Orgel *et al.*'s [4] crystallographic unit cell (see Figures 6.9 and 6.12). The hexagonal lattice parameter was accordingly determined to be $a_H \approx 15$ nm.

However, it is interesting to note that while we were constructing the fibril in the aforementioned manner, the TC molecules of the fibril filled up only half of the available lattice sites of the crystal structure. As can be seen in a cross-section of the fibril in a chosen lattice plane (see Fig. 6.13), the TC molecules (colored red) rather formed sparse isolated rows or clusters of cross-linked TC molecules leaving half the total number of available lattice positions empty. But since according to Orgel *et al.*'s unit cell specification [4] for a perfectly crystalline fibril, a TC molecule had to be located at every lattice position, this meant that the empty sites had to be filled up with a second cross-linked cluster of identical TC molecules (colored blue in Figure 6.13) interwoven with, but completely disconnected and displaced (by a determinate lattice vector) from the previous cluster. Therefore we grew a second percolated cluster of cross-linked TC molecules in order to fill up the sites left empty by the first growth process. The above finding strongly suggests that the cross-linking mechanism will have important implications for the elasticity of a fibril.

Furthermore, to obtain an approximately cylindrical fibril we ensured that all added TC molecules were completely enclosed in a fixed cylinder of pre-specified radius R and height H , and whose axis was oriented parallel to the end-to-end vector of the TC molecules and made to pass through one lattice

a prespecified probability p , so that p would be yet another parameter whose value reflects the extent of cross-linking in the fibril. For example, for $p = 0$ the fibril would be fully cross-linked, while for $p = 1$ the fibril would be completely uncross-linked. Once a cross-link has survived the elimination process, it remains active throughout the rest of the simulation.

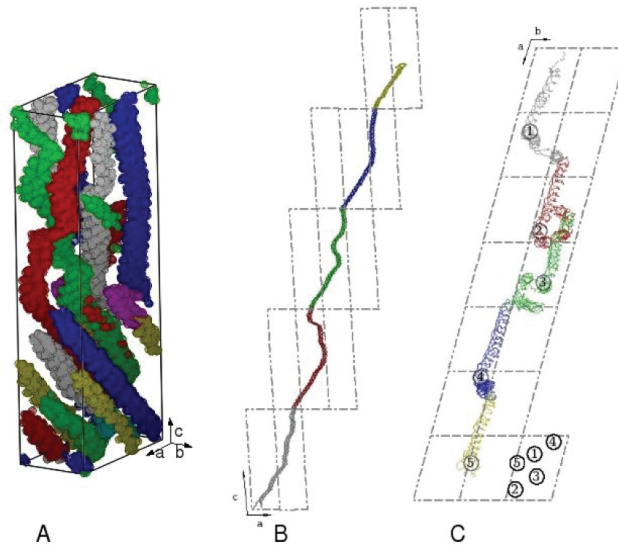


Figure 6.12: (Source: Orgel *et al.* [4]) Lateral positions of neighboring TC molecules and the molecular conformation of a single TC molecule. a , b and c are the unit lattice vectors. The c -axis has been compressed 5 times for (A) and (B). The collagen segments are labeled as follows: 1 gray; 2 red; 3, green; 4, blue; 5, yellow. Part of segment 1 is colored cyan (the N-terminus), and part of segment 5 is colored magenta (the C-terminus) to aid their identification in (A). (A) Alpha-helix carbons rendered as line spheres showing the conformation of the staggered collagen segments within a single unit cell. (B) Molecular path of a collagen molecule through successive unit cells in the a - c plane. (C) Molecular conformation of a collagen molecule in the a - b plane, looking down the c -axis (or roughly C- to N-terminus direction of the collagen molecule). The relative lateral positions of the molecule as it passes through $D = x.44$ are marked (where $x = 0, 1, 2, 3, 4$).

site. These values of R and H became the dimensions that the fibril finally assumed upon completion of the generation process, that is, when no more TC molecules could be added to the lattice that were wholly enclosed in the cylinder.

At this point, the reader may be wondering how we would deal with the problem of preserving possible entangled states of the cross-linked TC molecules during our simulation. Surprisingly, it turns out that in the case of collagen fibrils with the particular cross-linking mechanism chosen above, entanglement is a nonissue, since the structure of the crystal lattice, coupled with the graph structure of a fully cross-linked fibril does not create closed loops anywhere in this network, but rather results in the topology of two inter-digitated trees (representing the two disjoint clusters of cross-linked TC molecules). It is however possible that some other cross-linking mechanism

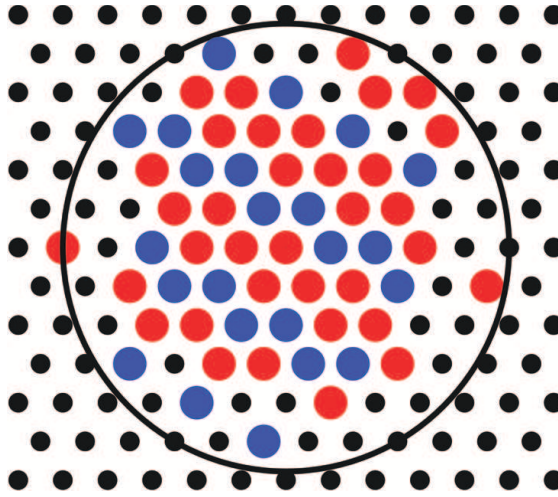


Figure 6.13: Lattice points (the black dots) within the drawn circular boundary of the fibril cross-section mark available positions through which a TC molecule might possibly pass (from beneath and out of the plane of the figure). The red dots mark the positions of TC molecules of a fibril that was generated beginning with a single TC molecule threading the lattice point in the center of the circle. Every one of these TC molecules is cross-linked to another to form a single percolated group. The cross-links (not shown) occur within, above, and below this lattice plane. Clearly almost half the number of lattice sites in this plane are empty. The blue dots mark the TC molecules of another percolated group that is generated beginning with a TC molecule threading a lattice site displaced one lattice unit to the right of the center of the circle. This group occupies those sites left empty by the red dots. These findings suggest that a fully cross-linked collagen fibril may consist of two inter-penetrating disjoint subsets of cross-linked TC molecules. The remaining empty lattice sites within and near the circular boundary exist because all the TC molecules that pass through them have contours that cross the cylindrical boundary of the fibril somewhere above or below this lattice plane.

(not explored here) will give rise to closed loops that may further result in permanently trapped entanglements of the TC molecules. In a non-kinetic MCMC simulation method such as ours, real-time dynamics are absent and thus all permissible processes, including even the slowest entangling or disentangling moves between loop-less chains, are assumed to have had enough time to have occurred.

6.3 The Monte Carlo Move Set \mathcal{M}

As mentioned in the introduction, we employ an off-lattice Markov Chain Monte Carlo simulation technique for our model in a constant temperature

ensemble. For this technique, the configurational state of our model fibril evolves according to Markov Chain dynamics governed by the master equation and detailed balance, rather than by Newton's laws of motion. Thus, even unphysical changes (moves, or transformations) of the current configuration of the model may be proposed. But detailed balance determines which proposed moves are eventually accepted, and thus permitted to change the configuration.

Three main constraints are to be enforced during the simulation: *(i)* preservation of the connectivity of the network structure of the fibril, *(ii)* preservation of the fixed-length bonds of the TC molecules and cross-links, and *(iii)* detailed balance.

For the latter requirement, we adhere to the recipe of the standard Metropolis algorithm, which prescribes that each proposed transformation of the system should possess an inverse transformation with the same proposal probability as that of the transformation itself, and furthermore that its probability of acceptance — the so-called acceptance ratio — should be correctly computed to eventually produce Boltzmann statistics. As pointed out, for instance by Maggs [62], in off-lattice systems such as ours, the infinitesimal configurational phase-space volume element in the vicinity of the current state is also transformed after any move, and hence we must not neglect to compute the Jacobian determinant of the transformation representing the move when determining the acceptance ratio. See Section 3.4 for a detailed explanation.

Suppose, during the simulation, the current state of our model at step s can be specified by the set $\{\mathbf{r}_0^{(s)}, \mathbf{r}_1^{(s)}, \dots, \mathbf{r}_N^{(s)}\}$ denoting the current positions of all the mass-points of the fibril, then for a proposal transformation $\mathbf{G}_\Delta : \{\mathbf{r}_0^{(s)}, \mathbf{r}_1^{(s)}, \dots, \mathbf{r}_N^{(s)}\} \rightarrow \{\mathbf{r}_0^{(s+1)}, \mathbf{r}_1^{(s+1)}, \dots, \mathbf{r}_N^{(s+1)}\}$ the Metropolis algorithm acceptance ratio is

$$\alpha_{(s) \rightarrow (s+1)} = e^{-\beta \Delta E(\mathbf{r}_k^{(s)})} \left\| \frac{\partial(\mathbf{r}_0^{(s+1)}, \dots, \mathbf{r}_N^{(s+1)})}{\partial(\mathbf{r}_0^{(s)}, \dots, \mathbf{r}_N^{(s)})} \right\|, \quad (6.7)$$

the last factor being the absolute value of the Jacobian determinant $|\det \mathcal{J}(\mathbf{G}_\Delta)|$ of the transformation, and $\Delta E(\mathbf{r}_k^{(s)}) = E(\mathbf{r}_{k+1}^{(s)}) - E(\mathbf{r}_k^{(s)})$ is the change in total energy of the fibril after the move.

The unique structure of our model fibril facilitates the use of a set of specialized types of moves, called the *move set* \mathcal{M} , from which the algorithm may randomly select a move as a proposal. Any desired probability distribution can be built over \mathcal{M} to increase the frequency of proposal of some move types over others (see for example Table 6.2 for the proposal probability distribution over the move set used in our simulations). In the following subsections we outline the types of proposal moves belonging to our move set.

6.3.1 Crank-Shaft $\mathcal{C}(\theta_c)$

The crank-shaft move type is popularly used in the simulation of single chains because of its simplicity and ease of computation. It works as follows: first randomly select a pair of mass-points belonging to the same TC molecule, then rotate that section of the TC molecule occurring between these two mass-points around the axis joining the two mass-points and through an angle θ_c whose value is randomly selected from a symmetric distribution over a given interval $[-\theta_{\max}, \theta_{\max}]$ (see Figure 4.2). The distribution of angles θ_c needs to be symmetric over the interval so as to ensure that the condition of reversibility stipulated by the Metropolis algorithm is obeyed. The Jacobian of such a transformation is unity.⁹

Care should be taken to ensure that the algorithm does not randomly select a pair of mass-points whose intervening chain fragment spans a cross-link, because then the subsequent crank-shaft rotation would destroy the cross-link, immediately compromising our model. Thus, crank-shaft rotations must occur only for those linear chain fragments occurring between cross-links. As a result, cross-links are never moved during a crank-shaft move.

6.3.2 TRACTRIX for Free Chains $\mathcal{T}_F(\delta)$

The foregoing discussion means that another type of move is required to displace also the cross-links, enabling them to fluctuate while simultaneously preserving the connectivity of the cross-linked system. Such a move would prove useful in an investigation of the importance of long-wavelength fluctuations to elasticity, which are mediated by cross-link fluctuations in a polymer network (such as, for example, in rubber [53]).

We refer the reader to Chapter 4, where a novel type of move called TRACTRIX was introduced for this very purpose. In the following couple of paragraphs, we summarize its essentials.

The fundamental variant $\mathcal{T}_F(\delta)$ of TRACTRIX, for a free linear chain, receives as input a random displacement vector δ that is used to displace one end (here coined the ‘driver node’) of a linear chain and drag the rest of the chain with it. For detailed balance to hold, δ is sampled from a point-symmetric distribution, that is, $P_{\text{gen}}(\delta)d\delta = P_{\text{gen}}(-\delta)d\delta$, where $P_{\text{gen}}(\delta)d\delta$ is the probability of generating δ .

None of the lengths of the bonds are changed by this process, but rather they are rotated and displaced causing the end-to-end vector of the chain also to change, albeit not by the given displacement, since the other end (the ‘tail’)

⁹Another variant of the crank-shaft move (not used in this thesis) involves three linear chains that terminate at one point. In this case, three mass-points are randomly selected (one on each chain). These three points define a plane about which those linear portions of the chains between the mass-points and the terminus can be reflected. Unlike TRACTRIX, such a move offers little control over where to place the mass-points.

of the chain is also displaced in the process. The movement of each bond is determined by a recursive application of the so called ‘discrete tractrix transformation’ [63], which is defined in Equations (4.4) and (4.5) of Section 4.4.

6.3.3 TRACTRIX for Anchored Chains $\mathcal{T}_A(\Delta)$

Another variant $\mathcal{T}_A(\Delta)$ of TRACTRIX, for an anchored chain, fixes one end, the ‘anchor’, of the linear chain in space while it displaces the other, the driver node, by the given random displacement Δ while the intervening bonds are collectively rotated and dragged to accommodate this change. Like δ , Δ must be sampled from a point-symmetric distribution for detailed balance to hold.

Again, none of the lengths of the bonds are changed by this process, but the end-to-end vector of the linear chain is changed by exactly Δ . Thus, when two or more linear chain fragments, each anchored at its own mass-point, all terminate at the same mass-point (this is a typical situation at a cross-link, or at a mass-point in the middle of a chain), then $\mathcal{T}_A(\Delta)$ may be applied to each fragment to displace that common terminus by Δ , while simultaneously fixing each anchor and deforming all the intervening fragments so as to accommodate the move (see Figure 4.7).

In practice, the implementation of $\mathcal{T}_A(\Delta)$ on a linear chain depends on the use of a numerical solver to solve for $\delta = \delta^*$ so that the action of $\mathcal{T}_F(\delta^*)$ on the linear chain under consideration will cause its end-to-end vector to be incremented by exactly Δ despite the fact that its tail is displaced in the process. But afterwards the entire chain is rigidly translated so that its tail coincides once more with its old position. The computation of the Jacobians resulting after this modification follow in the same manner to that described in the Section 4.6. In the supplementary information [65] accompanying this thesis we provide computer codes written in C++ that implement and apply this modification.

6.3.4 TRACTRIX for Fibrils $\mathcal{T}_{AB}(\mathcal{R})$

Now we introduce a generalization $\mathcal{T}_{AB}(\mathcal{R})$ of $\mathcal{T}_A(\Delta)$, which is particularly useful for simulating fibrils or bundles of polymers, and which does not require the chains to terminate at a common mass-point. Indeed, in a single simulation step, an entire assembly of distinct mass-points (called the driver nodes) that extends over a (not necessarily planar) cross-section of the bundle, may be simultaneously displaced by means of the rigid-body transformation \mathcal{R} . \mathcal{R} can be a rotation (through a small random angle around a random axis) or a small random translation. Immediately after these driver nodes are displaced, all the linear chain fragments connecting these driver nodes to their corresponding anchors must be deformed accordingly.

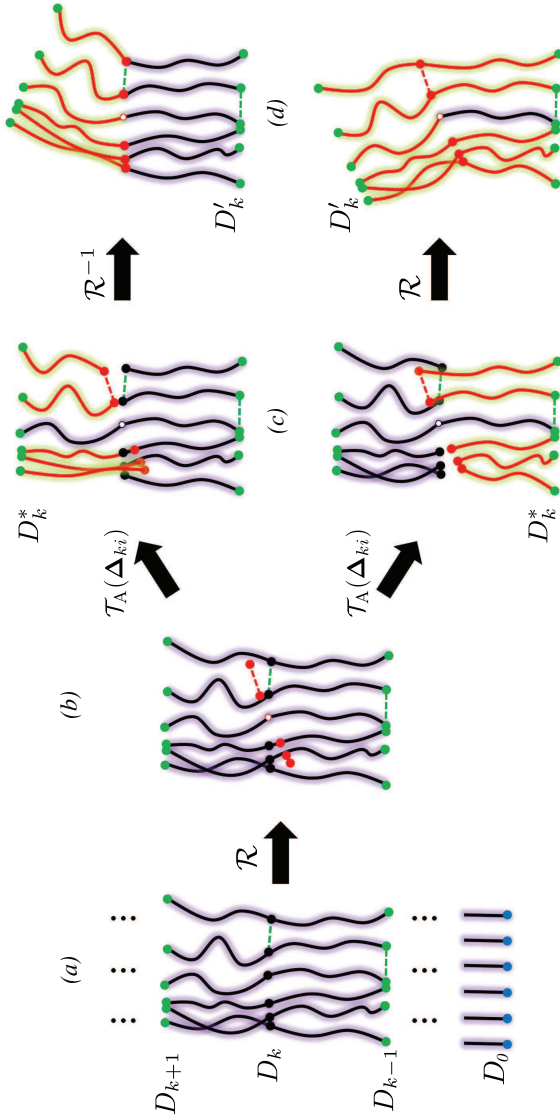


Figure 6.14: Transformation of the configuration of the fibril using TRACTRIX for fibrils [$\mathcal{T}_{AB}(\mathcal{R})$]. A section of the fibril is shown in (a). The fibril continues downwards to one end D_0 (denoted by the blue dots) which is fixed in space throughout the simulation. It also continues upwards to the other end (not shown) which is free. The black dots in the section represent the mass-points of a randomly chosen cross-section D_k (not necessarily planar) from the sequence $\{D_k\}$ of all cross-sections of the fibril. The green dots represent the mass-points in the nearest neighbouring warped cross-sections D_{k-1} and D_{k+1} . The dashed lines denote the possible inextensible cross-links between the mass-points of a cross-section. (b) A rigid-body rotation \mathcal{R} about a random axis which, in this case, happens to be perpendicular to the plane of the figure, and passing through the randomly chosen mass-point represented by the white dot, is applied to all the mass-points (now driver nodes) of D_k . The new positions of the driver nodes are represented by the red dots. (c) $\mathcal{T}_A(\Delta)$ is applied to the linear fragments connecting D_k to one of its neighbours D_k^* chosen at random. Thus the fibril is temporarily severed. If $D_k^* = D_{k-1}$, then the mass-points of D_{k-1} are anchored during this transformation. If rather $D_k^* = D_{k+1}$, then the mass-points of D_{k+1} are anchored during this transformation. (d) Because only the lower end of the fibril is fixed, either \mathcal{R} or \mathcal{R}^{-1} must be applied to the entire part of the fibril on the upper side of D_k in order to heal the rift in the fibril created in (c). See Subsection 6.3.4 for more details.

By restricting the transformation of the driver node assembly in one cross-section to rigid-body translations and rotations, the distances between any pair of driver nodes in that assembly is preserved. The preservation of the distances between driver nodes is a crucial requirement especially when there exist some fixed-length cross-links lying in the (warped) cross-section and bridging a few pairs of driver nodes.

Therefore, at the start of the simulation, all possible driver nodes and anchors in the fibril can be assigned as a sequence $\{D_k\}$ of a few designated cross-sections of the fibril, and in such a way that each cross-link in the fibril is located entirely within one of these cross-sections. The linear chain fragments bridging successive cross-sections in this sequence are then cross-link-free.

During the simulation, if at some random step s $\mathcal{T}_{AB}(\mathcal{R})$ is selected from the move set \mathcal{M} , then one cross-section D_k in the sequence may be selected at random, and then a random \mathcal{R} is applied to it.

If \mathcal{R} is a rigid-body translation through a displacement Δ , the new positions of each driver node P_i are then

$$\mathbf{r}_i^{(s+1)} = \mathbf{r}_i^{(s)} + \Delta. \quad (6.8)$$

Note that Δ must be sampled from a point-symmetric distribution for detailed balance to hold. If \mathcal{R} is a rigid-body rotation through a random angle ϕ around an axis along a random unit vector $\hat{\mathbf{u}}$ which passes through a randomly selected driver node P_c in D_k , then the new positions of each driver node P_i are

$$\mathbf{r}_i^{(s+1)} = \mathbf{r}_c^{(s)} + \mathcal{O}_{(\phi, \hat{\mathbf{u}})} \cdot (\mathbf{r}_i^{(s)} - \mathbf{r}_c^{(s)}). \quad (6.9)$$

where $\mathcal{O}_{(\phi, \hat{\mathbf{u}})}$ is a rotation matrix that rotates vectors through the angle ϕ around an axis along $\hat{\mathbf{u}}$ passing through the origin. Again, for the sake of detailed balance, ϕ must be sampled from a symmetric distribution over an interval $[-\phi_{\max}, \phi_{\max}]$, where ϕ_{\max} can be specified at the start of the simulation, while $\hat{\mathbf{u}}$ can be sampled from a uniform distribution over the surface of the unit sphere. In this way, the fibril is able to bend and twist in any direction. In general, each driver node P_i of D_k is given its own displacement Δ_{ki} .

Next, each of the linear fragments C_{ki}^* that connects the driver nodes of D_k to D_k^* (a random selection of one of D_k 's two neighboring cross-sections: D_{k-1} or D_{k+1}) is deformed by $\mathcal{T}_A(\Delta_{ki})$, which treats all the mass-points in D_k^* as anchors during this step. Alternatively, if some of the linear chain fragments C_{ki}^* have free ends in D_k^* , then $\mathcal{T}_F(\Delta_{ki})$ may instead be applied to deform these free linear chain fragments while $\mathcal{T}_A(\Delta_{ki})$ is applied to the other fragments. This process temporarily severs the fibril.

Finally, to restore the fibril, the linear chains C'_{ki} connecting D_k to the other neighbouring cross-section D'_k (the one which was not chosen during the latter random selection) can also each be deformed by $\mathcal{T}_A(\Delta_{ki})$ treating all the mass-points in D'_k as anchors (or optionally by $\mathcal{T}_F(\Delta_{ki})$ for those fragments with free ends in D'_k).

However, it may be that one end of the fibril is fixed while the other end is free throughout the simulation. Then we may exploit this situation so that, instead of the final step above, the entire part of the fibril on that side of D_k opposite the fixed end of the fibril, may be appropriately transformed by \mathcal{R} or \mathcal{R}^{-1} depending, respectively, on whether D_k^* is on the same side of the fixed end or not, so as to heal the rift in the fibril previously created by the transformation of the linear fragments C_{ki}^* (see Figure 6.14).

Finally, recalling that for all these moves detailed balance must be obeyed, we proceed to compute their corresponding Jacobians. But in order not to overburden the main text, we postpone the computation of these Jacobians until Appendix 6.A.

The power of TRACTRIX lies in its ability to keep all bond lengths and cross-link lengths of the fibril constant while exploring configuration phase space. Throughout our simulations, only $\approx 0.04\%$ of all attempted TRACTRIX moves failed due to the numerical solver's inability to find a configuration to fit the proposed end displacements. The value of f (from Equation (4.5)) used for the TRACTRIX moves was set to 2 as this value yielded the least failure rate. The maximum number of bonds in a linear chain taking part in any TRACTRIX move type was set to 15.

A computer program was written in C++ using Intel[®] MKL libraries to evaluate the Jacobian determinants, GNU Scientific Library for its nonlinear equation solvers, and FreePOOMA, a high-performance C++ library implementing arrays and vectors. The program was compiled with Intel[®] C++ Compiler and each program instance could run on eight CPU's simultaneously. Simulation speed was found to be roughly 250 000 MCMC moves per hour.

6.4 Results

The dimensions of the fibril we simulated, and other relevant parameters are listed in Table 6.1. Figures 6.15-6.23 show the results of our simulations.

Recall from Section 6.2.5 that before the simulation, the fibril was generated within a cylinder of specified radius and height. This cylinder's dimensions were eventually assumed by the fibril itself¹⁰. As a consequence of the staggered arrangement of the TC molecules within the crystal and the restriction we imposed that all added TC molecules must be wholly enclosed in this cylinder, the number of TC molecules per cross-sectional area near the ends was significantly less than that near the mid-section of the fibril. Therefore, anticipating that the flexural rigidity of the fibril near its ends would consequently be reduced relative to the flexural rigidity near its mid-section, we designed the grafted end of the fibril to include all parts of those TC molecules

¹⁰The diameter of the fibril that we simulated (15 nm) is slightly less than the smallest collagen fibril diameter (20 nm) observed experimentally in Ref [112].

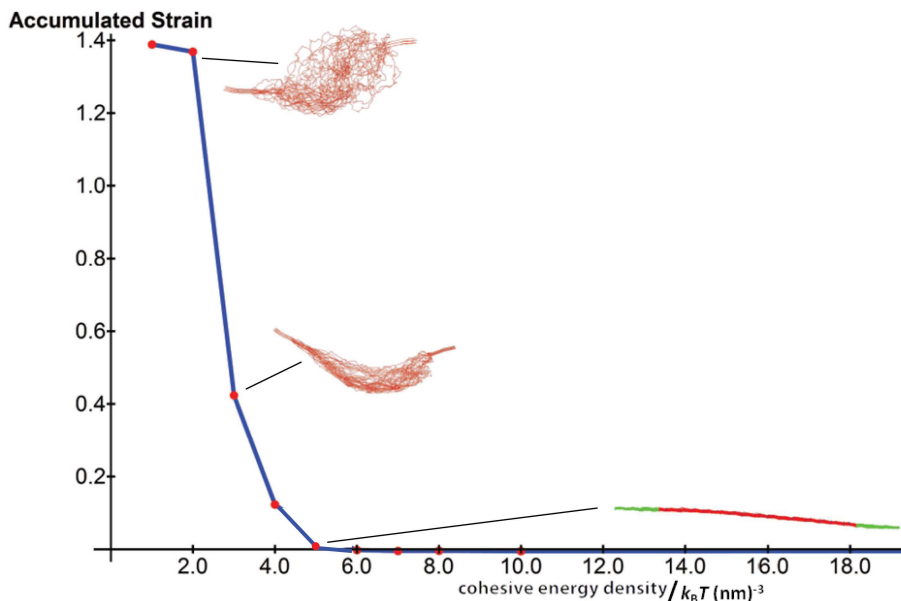


Figure 6.15: Plot of the average accumulated strain $\langle \bar{\epsilon} \rangle$ (a measure of the deviation from perfect fibril crystallinity [defined in Section 6.4]) versus the cohesive energy density v_A . The insets are snapshots of the thermally relaxed fibril for the labeled values of v_A which qualitatively illustrate the meaning of $\langle \bar{\epsilon} \rangle$ — as v_A decreases $\langle \bar{\epsilon} \rangle$ increases and the fibril becomes more like a disordered isotropic network blob. Note the sharp transition near $v_A = 5k_B T \text{ nm}^{-3}$. This value of $v_A \approx 5k_B T \text{ nm}^{-3}$ was eventually the one chosen for subsequent simulations of bending experiments because it yielded approximately no deviation from perfect crystallinity ($\langle \bar{\epsilon} \rangle \approx 0$). Recalling that our attractive overlap potential [Equation (6.2)] mimics an Asakura-Oosawa depletion interaction potential [110], $v_A = 5k_B T \text{ nm}^{-3}$ may be interpreted as the minimum ‘pressure’, exerted by the depleting particles of an implicit solvent, required to prevent a high aspect-ratio fibril from falling apart. Note also that during all simulations, both fibril ends were ‘frozen’ (see Section 6.4 for an explanation) and, in addition, one of them was grafted (held fixed) in space.

extending from one extreme end to a cross-section located $4.5 \times 67 \text{ nm}$ away where the fibril was just as dense as near its middle and therefore able to offer the maximum resistance to bending stresses. These portions of the TC molecules at the grafted end were kept ‘frozen’ throughout the simulation, that is, they were not allowed to relax. Similarly, the other end of the fibril (of similar length $4.5 \times 67 \text{ nm}$) was kept frozen. The only difference being that transverse loads were applied at a point of the fibril just before that frozen end in order to



Figure 6.16: Simulation snapshot. Side view of the relaxed unloaded crystalline fibril obtained after the simulation. The wavy profile displayed is in fact right-handed writhing of the bundle as also evidenced by the end view of this same fibril state displayed in Figure 6.17. Note that the profile of the fibril before the start of the simulation was perfectly straight. The portions of the fibril near its ends (those colored green) where not allowed to thermally relax. Each portion is of length 4.5×67 nm along the fibril. The left end is the grafted end.

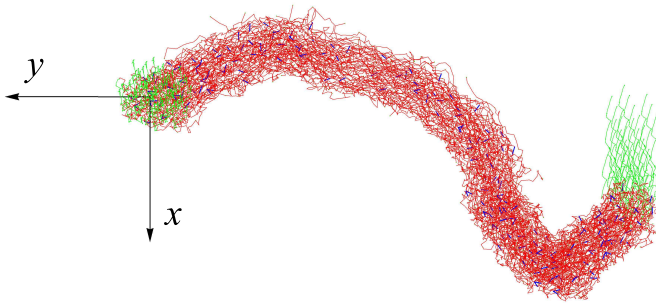


Figure 6.17: Simulation snapshot of the same fibril as in Figure 6.16. End view of the relaxed unloaded crystalline fibril displaying its right-handed writhe. Note that the axis of this writhing fibril is not oriented along the z -axis. The portions of the fibril near its ends (those colored green) where not allowed to thermally relax. Each portion is of length $4.5D$ along the fibril. The left end is the grafted end.

produce bending of the main stem of the fibril (that is, the part of the fibril between both frozen ends). The frozen fibril ends are often shown colored green, for example in Figures 6.15-6.17. To further justify our decision to freeze the fibril's ends we mention that in an actual laboratory pulling experiment, one fibril end is glued to some fixed substrate and the other to a force probe, such as an AFM cantilever tip (see, for example, Refs. [113, 114]). Thus both of them take little part in the deformation of the fibril itself while it is being stretched.

The first few simulations of the fibril were performed with zero load but with cohesive energy density v_A set to various chosen values starting from zero in order to determine the least value necessary to maintain the starting dimensions of the fibril throughout the simulation. As expected, for very small values of v_A the fibril degenerated into a random network blob despite the fact that

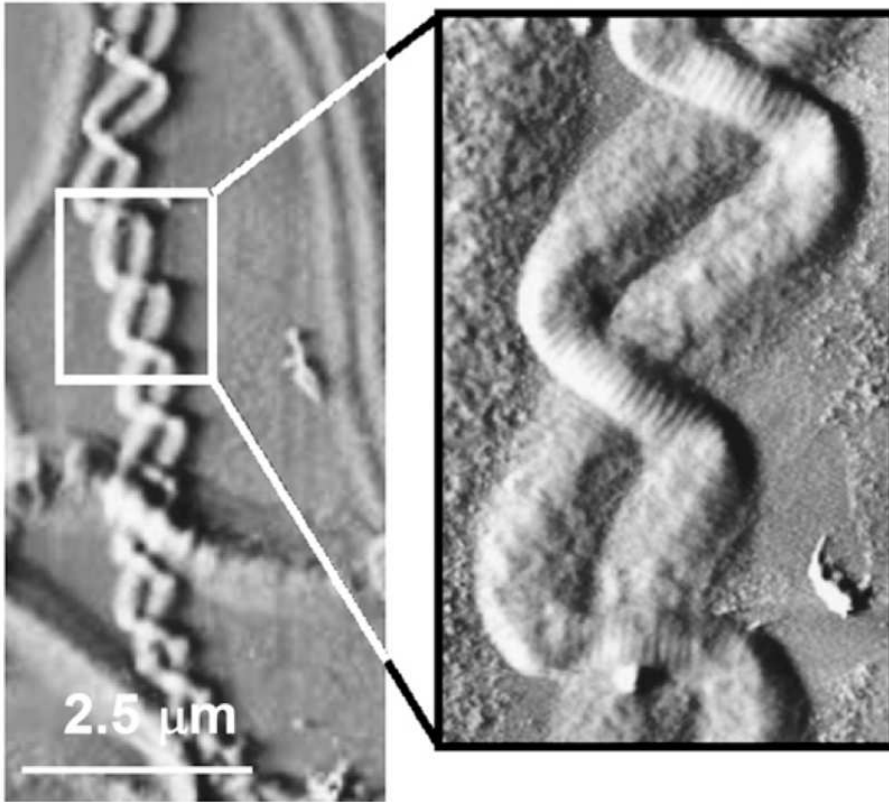


Figure 6.18: An AFM micrograph from Ref. [111] clearly displaying the helical conformation of collagen fibrils: contact mode AFM error signal image of digital tendon collagen fibrils (scale bar, $2.5 \mu\text{m}$) (higher magnification, inset).

it remained fully cross-linked, while for larger values a stable slender fibril was achieved (see Figure 6.15).

To gain a quantitative measure of how far from its perfectly crystalline state the fibril evolved, we introduced a new quantity, $\langle \bar{\epsilon} \rangle$, called the average accumulated strain which is described as follows: at the beginning of each simulation, when the fibril was in its perfectly crystalline state, imaginary bonds were designated between every pair of nearest-neighbouring lattice points within each cross-section of the fibril. This was achieved using a standard Delaunay triangulation routine [72]. Then the lengths of these imaginary bonds were tracked throughout the simulation, and $\langle \bar{\epsilon} \rangle$ was computed as the sample mean of:

$$\bar{\epsilon} \equiv \frac{\text{Sum of imaginary bond lengths in deformed state}}{\text{Sum of imaginary bond lengths in perfectly crystalline state}} - 1. \quad (6.10)$$

This meant that values of $\langle \bar{e} \rangle \leq 0$ obtained at the end of the simulations indicated that a slender cylindrical fibril was achieved, while values of $\langle \bar{e} \rangle > 0$ indicated that an unstable fibrillar blob had developed.

Figure 6.15 shows the results of these simulations, which were intended to search for a suitable value of v_A . Notice the rather sharp transition in the value of \bar{e} as v_A changes near $v_A = 5k_B T \text{ nm}^{-3}$ (for which $\bar{e} \approx 0$). This is the value we chose and used for subsequent bending experiments.

The order of magnitude of $v_A = 5k_B T \text{ nm}^{-3}$ could be tentatively rationalized if we considered two straight and parallel TC molecules lying side by side and at a distance d_T apart. If $d_T < 2r_c$, where r_c is the radius of the cylindrical attractive potential surrounding the bonds of each TC molecule, then, by Equations (6.2) and (6.4), the binding energy between the TC molecules is $E_b = -v_A \ell_c \left(2r_c^2 \arccos \frac{d_T}{2r_c} - d_T r_c \sqrt{1 - \left(\frac{d_T}{2r_c} \right)^2} \right)$, where ℓ_c is the length of the TC molecules. Bending fluctuations of the TC molecules will therefore need enough thermal energy to overcome this binding energy and drive the molecules completely apart. Supposing one TC molecule remains fixed while the other is allowed to fluctuate, we may invoke the equipartition theorem to estimate how much thermal energy Q is required for complete unbinding, thus multiplying $k_B T/2$ by the number of independent degrees of freedom of the fluctuating TC molecule. A WLC of persistence length ℓ_p may be considered to be equivalent to a FJC of the same contour length but with bond length $2\ell_p$. Since our model TC molecules had $\ell_p = 8 \text{ nm}$ and $\ell_c \approx 300 \text{ nm}$ (see Table 6.1), the number N of bonds of the equivalent FJC is $300 \text{ nm}/(2 \times 8 \text{ nm}) \approx 19$. The number of independent degrees of freedom of a FJC with N bonds is $2N + 3$ (that is, the total number of translational degrees of freedom, which is 3 times the number of vertices, minus the number of fixed length constraints of each bond). Hence $Q = (2N + 3)k_B T/2$, which must be greater than or equal to $|E_b|$ expressed above in terms of d_T . For this to be true, we solve for d_T and obtain the condition $d_T \leq 13.96 \text{ nm}$. The upper limit 13.9 nm of the distance d_T between TC molecules compares well with the hexagonal lattice parameter of the fibril crystal structure, $a_H \approx 15 \text{ nm}$ (see Figure 6.11).

With the value of v_A now determined, we subsequently performed simulations with zero applied transverse force. Snapshots of the resulting fibril configuration are shown in Figures 6.16 and 6.17. In these snapshots, the fibrils appear to have developed an effective right-handed writhe. We discuss this unexpected result in the next section.

Values of relevant parameters used for the moves of the MCMC simulation, and the typical acceptance rates obtained are listed in Table 6.2. The lowest acceptance rates are due to the tight confinement of the TC molecules in the narrow space occupied the fibril. Therefore many moves led to overlap between the TC molecules and their subsequent rejection. For fibrils with low cohesive energy density, for which swollen random networks form (see Fig-

ure 6.15), these acceptance rates are typically much higher and close to 70%.

In this study, only fibrils subjected to transverse bending forces were simulated. It is not difficult to use the same model to study other deformation modes such as stretching and twisting. For stretching, one need only direct the force along the z -axis, while for twisting, one needs to apply a torque instead of a force while optionally constraining the movement of the fibril tip along the z -axis. Figures 6.20, 6.22, and 6.21 show respectively the values, as the simulation ran, of the x , y , and z coordinates of the point B near the end of the fibril where the transverse force of magnitude F was applied to bend the fibril. The other end A was grafted at the origin (see Figure 6.19). The corresponding values for the total sum of bending energies of the individual TC molecules of the fibril are shown in Figure 6.23.

Parameter	Value
Fibril Diameter	≈ 15.00 nm
Fibril Length	≈ 1.6272 μm
Number of WLCs	219
Maximum Number of WLCs per Cross-section	58
Number of Bonds per WLC	113
Bond Length	8.0/3 nm
WLC Contour Length ℓ_c	301.333 nm
WLC Persistence Length ℓ_p	8.0 nm
Bond Radius r	0.5 nm
Cohesive Distance r_c	0.7 nm
Cohesive Energy Density v_A	$\approx 5k_B T \text{ nm}^{-3}$

Table 6.1: Table of parameters of the simulated fibril. Each TC molecule was represented as a discrete WLC.

6.5 Discussion

We now collect and interpret the central findings from our mechanical experiment on the collagen fibril.

6.5.1 Fibrillar Young's Modulus

Values of the Young's modulus of the fibril for the various bending forces considered are shown in Table 6.3. These values were obtained by using a least-squares method to fit the bent profile of a Timoshenko beam of the same dimensions and isotropic medium subjected to the same bending forces as the fibril. Values obtained are within the range of measured laboratory values of Young's moduli reported in the literature for hydrated reconstituted collagen

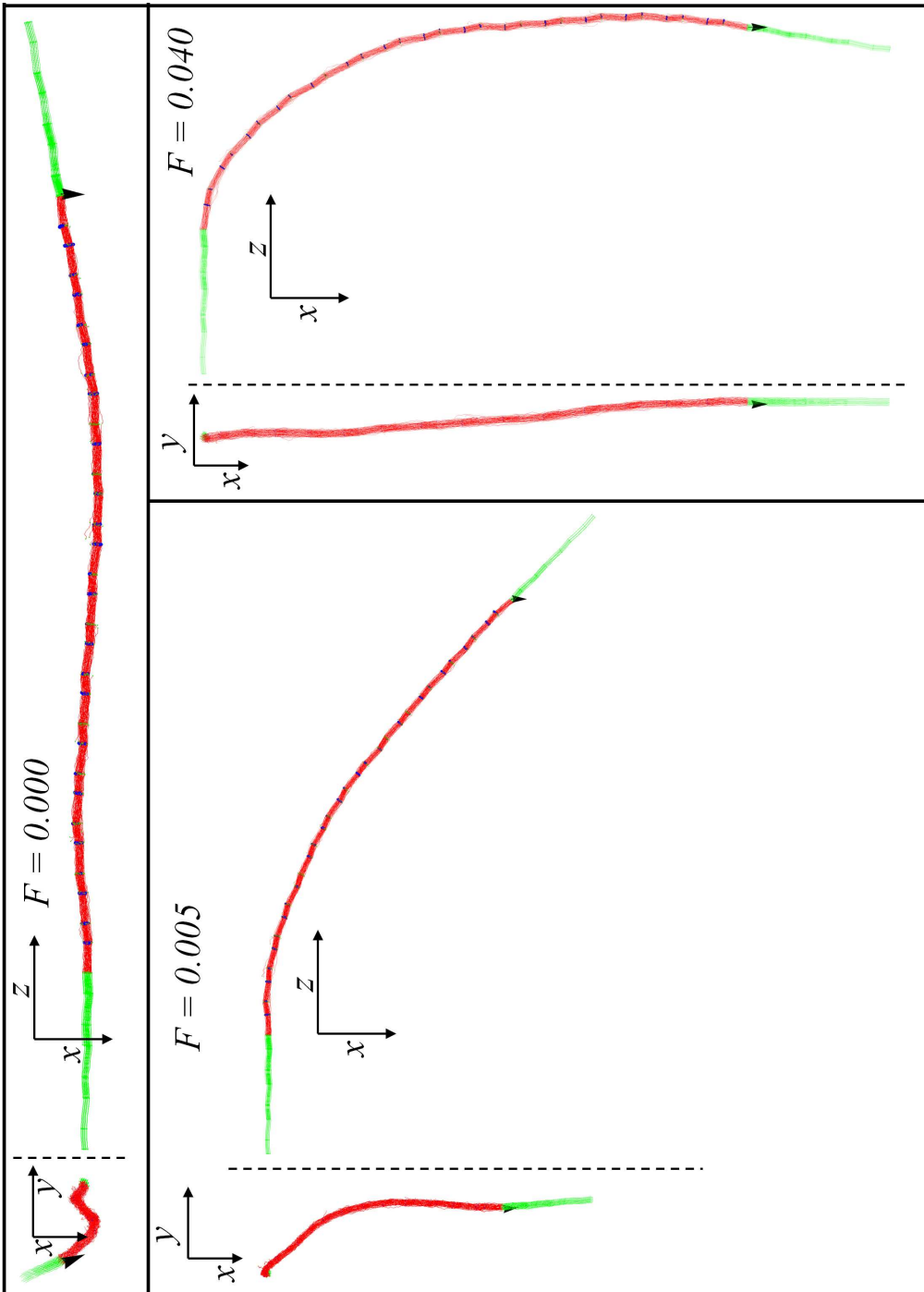


Figure 6.19: Simulation results. Snapshots of our 3D model fibril (note the different viewing directions denoted by the axes) subjected to various bending forces of magnitude F in units of $k_B T \text{\AA}^{-1}$.

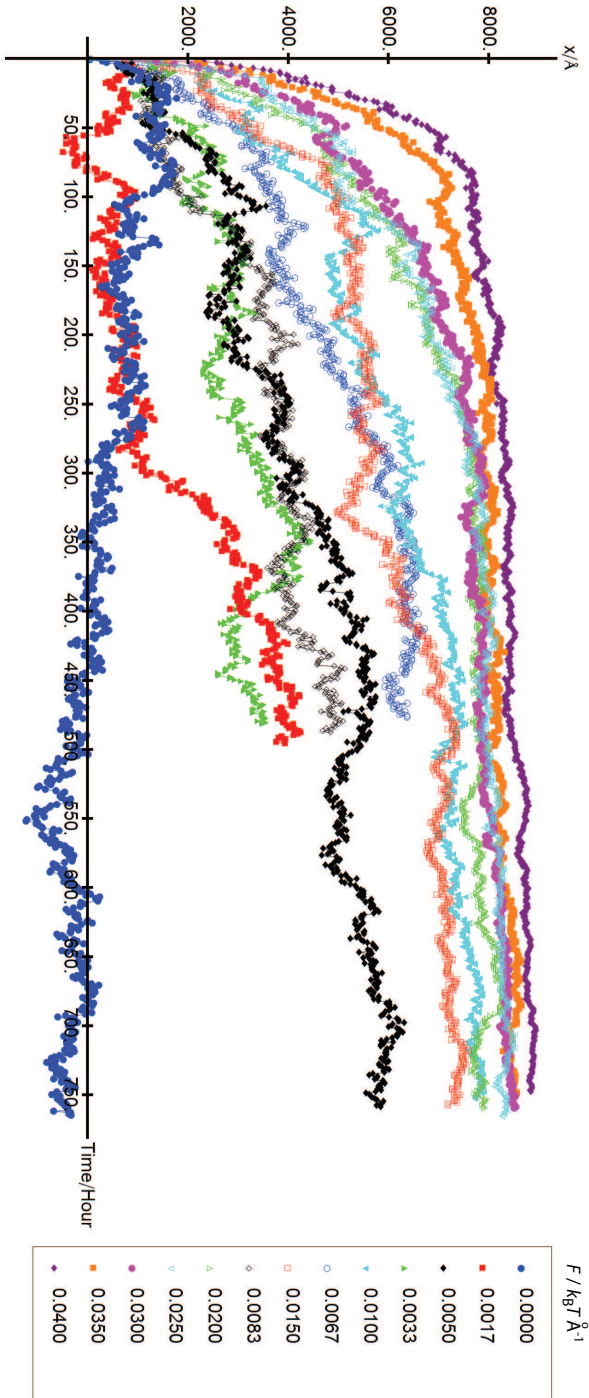


Figure 6.20: Simulation results. Trajectory of the x -coordinate of point at the frozen end B of a $1\ \mu\text{m}$ -long fibril initially aligned along the positive z -axis, with the other end A was fixed at the origin, and for various magnitudes of a transverse force F acting at B and directed in the x -direction. Consecutive data points are separated by 250 000 MCMC moves.

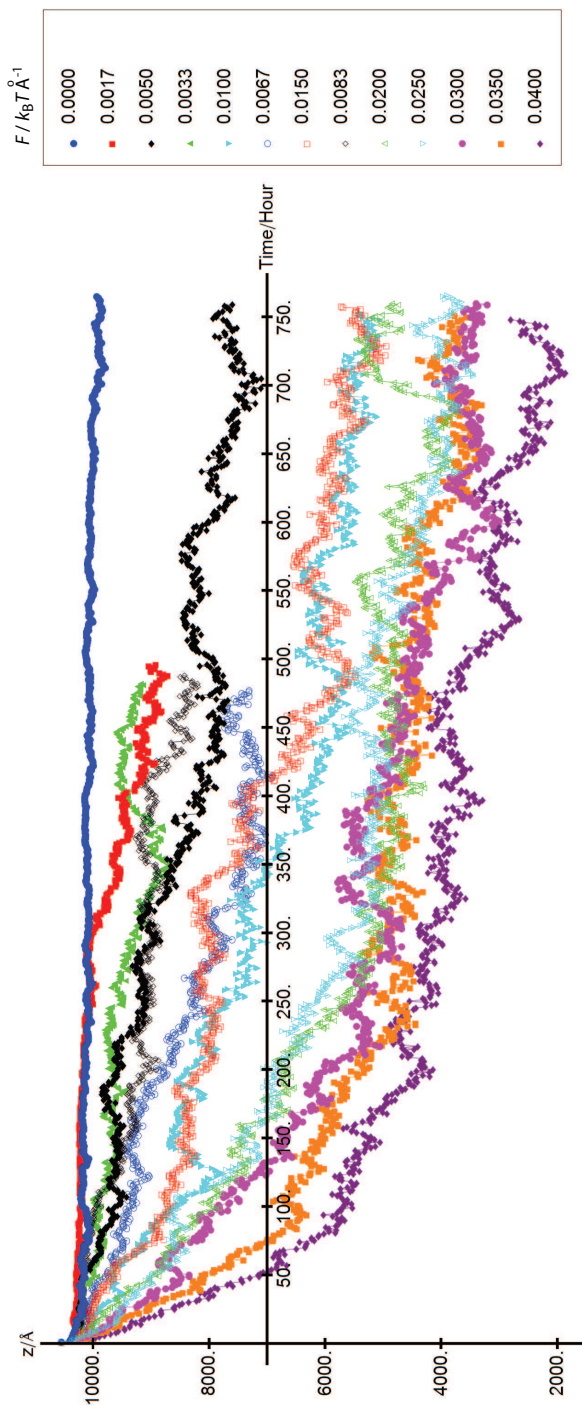


Figure 6.21: Simulation results. Trajectory of the z -coordinate of point at the tip B of a $1\ \mu\text{m}$ -long fibril initially aligned along the positive z -axis, with the other tip A is fixed at the origin, and for various magnitudes of a transverse force F acting at B and directed in the x -direction. Consecutive data points are separated by 250 000 MCMC moves.

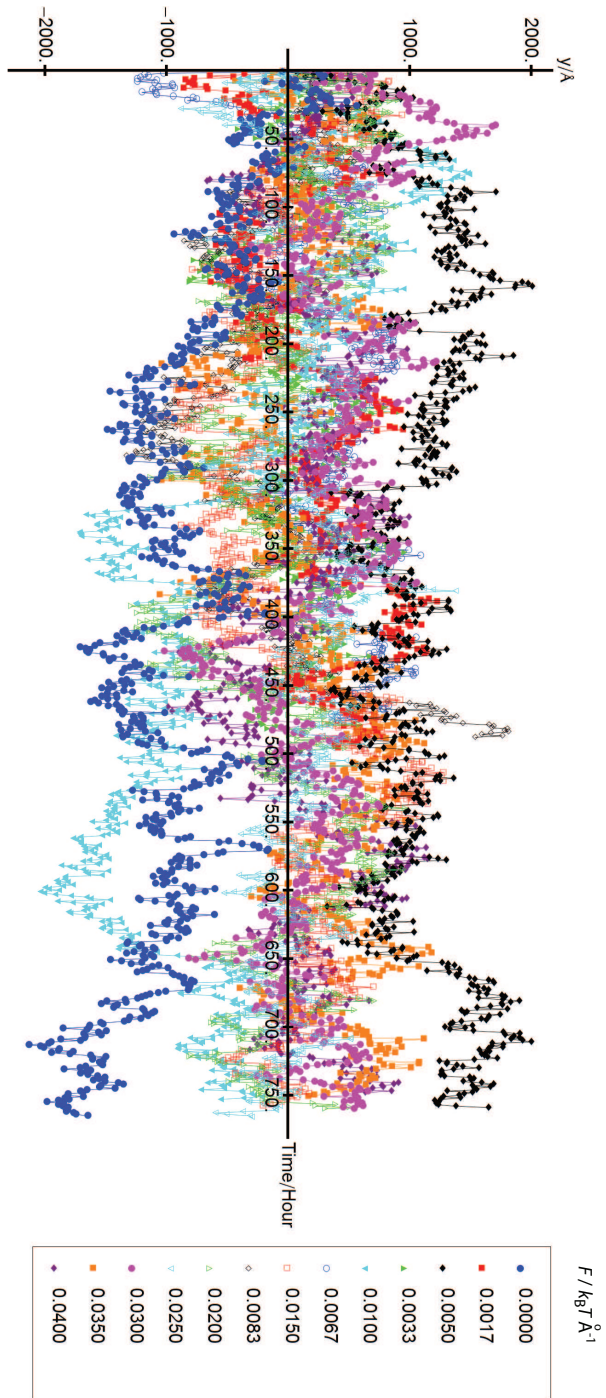


Figure 6.22: Simulation results. Trajectory of the y -coordinate of point at the tip B of a $1\ \mu\text{m}$ -long fibril aligned along the positive z -axis, with the other tip A fixed at the origin, and for various magnitudes of a transverse force F acting at B and directed in the x -direction. Consecutive data points are separated by 250 000 MCMC moves.

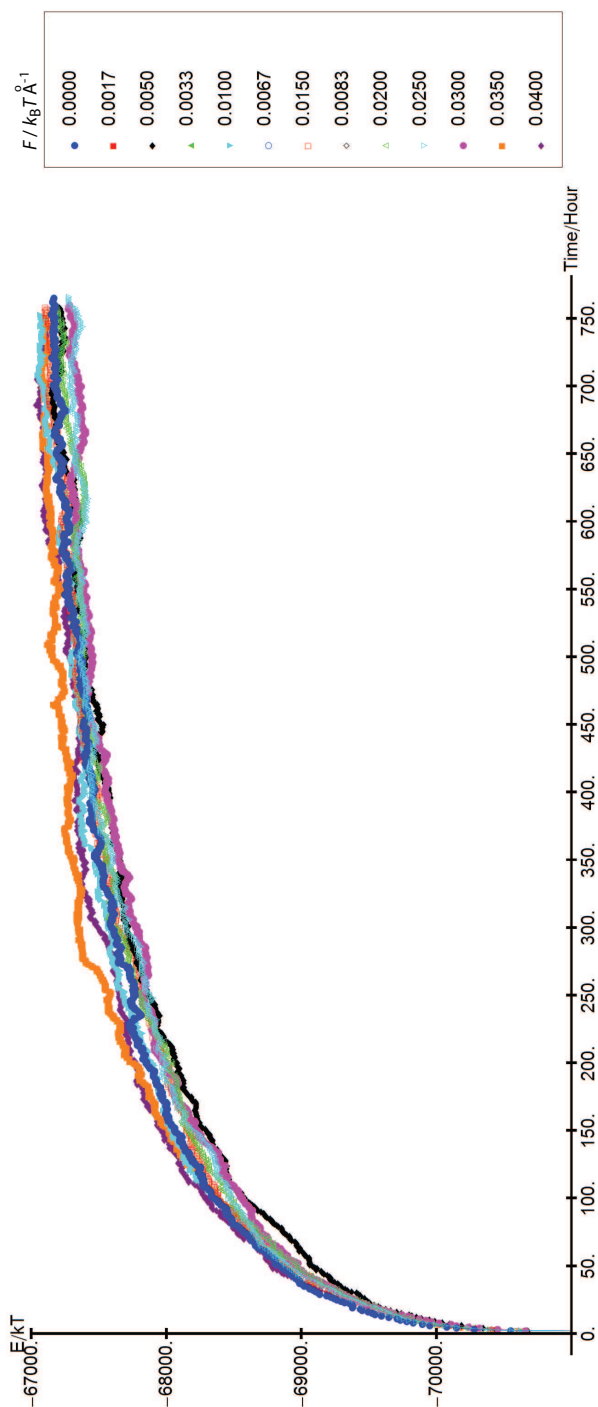


Figure 6.23: Simulation results. Evolution of the sum of bending energies of all 219 TC molecules, each with 113 bonds (see Equation (6.1)) in the fibril initially aligned along the positive z -axis, with one end A fixed at the origin, and the other subjected to various magnitudes of a transverse force F directed in the x -direction. Consecutive data points are separated by 250 000 MCMC moves. These results show that the effect of our applied transverse forces F on the bending energies of the TC molecules themselves appear to be slight, even if it leads to a large deformation of the fibril.

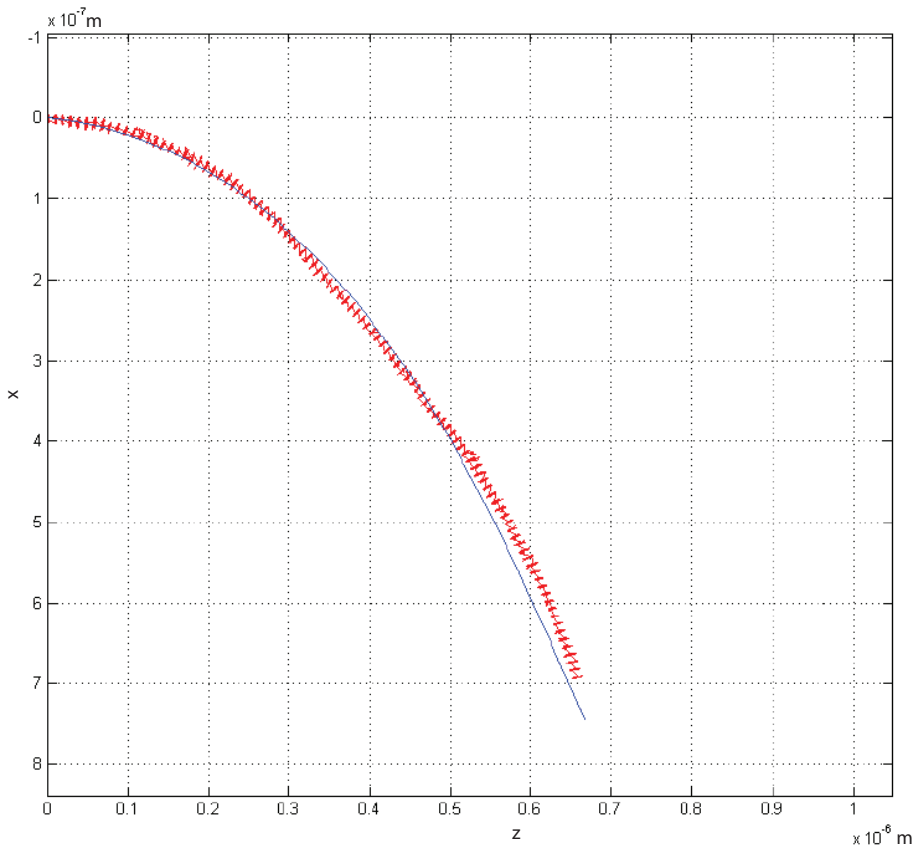


Figure 6.24: The elastic constants of the fibril are estimated by means of a least-squares fit of a similar sized Timoshenko beam of circular cross-section bent in the same way by the force F as for the fibril. In this figure, the red points are projections onto the xz -plane of selected points of the fibril. The smooth blue curve is the numerical solution to the Timoshenko beam differential equations given in Section 2.10. The Young's modulus E and shear modulus G , which parameterize these differential equations, were varied using the MATLAB[®] minimization routine `lsqcurvefit` so that their numerical solution might fit, in a least-squares sense, to the red points of the simulated fibril. Some results are given in Table 6.3. Unfortunately, this procedure is not very sensitive values of the shear modulus within a very large range: 10^{-5} MPa to 10^{-2} MPa.

MCMC Move Type	Distribution	Proposal Probability	Typical Acceptance Rate ¹
Crankshaft Rotation Angle	Uniform; Range: [-45° , 45°]	10.00%	85%
Driver Node Displacement	Spherical; Radius: 1 Å	12.50%	40%
Rigid Cross-section Rotation Angle	Uniform; Range: [-0.5° , 0.5°]	50.00%	7%
Rigid Cross-section Displacement	Spherical; Radius: 1 Å	0.50%	1%
Rigid Cross-link Rotation Angle	Uniform; Range: [-0.5° , 0.5°]	1.00%	24%
Rigid Cross-link Displacement	Spherical; Radius: 1 Å	1.00%	27%
Cross-link Drag Displacement ²	Spherical; Radius: 0.5 Å	25.00%	94%

Table 6.2: Table of relevant parameters and acceptance rates for the MCMC move types.

^aThis applies TRACTRIX to a randomly chosen cross-link, effectively pulling on it and dragging the chains to which it is linked.

^bThese rates are specific to the fibril in Table 6.1, and are defined as the percentage of proposed moves that were accepted. For $v_A \ll 5k_B T \text{ nm}^{-3}$ acceptance rates can be much higher (close to 70%) since then the TC molecules have more free space to move about without rejection.

fibrils [113, 115]. However, we also note that there have also been reports of measurements of Young's moduli as high as a few GPa for dried native fibrils [113, 116, 117, 81]. Thus our simulations' modulus values are towards the lower end of the experimentally observed stiffnesses for collagen fibrils.

The shear moduli, which should also have been obtainable from the Timoshenko beam analysis we employed have been omitted from Table 6.3 since our fitting procedure was largely insensitive to the value of the shear modulus - this may be a result of the fact that the fibril is actually not sheared very much in the tip loaded configuration in our simulations. However, our values of the shear modulus ranged from 10^{-5} MPa to 10^{-2} MPa.

Also since the fibril itself fluctuates, taking on different conformations about an average bent profile, it was difficult to obtain satisfactory Timoshenko beam fits to any single fibril snapshot. Furthermore, none of the (ensemble) average bent profiles themselves were confined to a single plane either, as it is for a Timoshenko beam. Therefore the fits were made to the projection of the profile snapshots on the $x - z$ plane. These issues reveal some

force /pN	E /MPa
0.21400	48.3 ± 0.1
0.42800	43.1 ± 0.1
0.64200	68.2 ± 0.1
0.85600	46.5 ± 0.1

Table 6.3: Table of elasticity constant estimates for various bending forces of the simulated fibril. These estimates were found by a least squares fit of the bent profiles of the fibril by those of a Timoshenko beam of the same dimensions subjected to the same forces. Further simulations would need to be performed to ascertain the relationship of the fibril's Young's modulus with applied force.

essential shortcomings of the conventional Timoshenko beam - indeed, we conclude that it is not a satisfactory model, as it is unable to capture the full mechanics of the collagen fibril.

6.5.2 Writhing and Residual Entropic Effects

With the exception of atomistic models [88, 81], almost all existing models of bundles of polymers and collagen fibrils assume negligible fluctuations or no entropic contributions to fibril elasticity by taking a variational approach. It is our contention that the thermal fluctuations of the constituent TC molecules and the long-wavelength fluctuations of the entire fibril are also important, contributing to elasticity, at least for small strains and for small diameters of the fibril. This behaviour is apparent from the simulation snapshots of Figure 6.19, which show that the unloaded fibril can fluctuate between various wavy conformations [and also sometimes goes into a helical conformation (Figure 6.17) and 6.16]. Also the undulations in the fibril are straightened out to an extent depending on the magnitude of the bending force (see for example, Figure 6.20). Figures 6.19 show that the magnitude of undulations of the fibril axis are increasingly reduced as it is subjected to larger transverse tip loads. In this sense, there are effective modes in the fibril that resemble the simple bending modes in semi-flexible chains which are responsible, for instance, for the entropic elastic response of actin and single tropocollagen chains. Even in this fairly large supramolecular structure, collective long-wavelength modes arise which remain subject to thermal fluctuations and continue to contribute to the low-strain response.

Our findings, however, do not imply that the entire fibril behaves effectively as a worm-like chain or a semi-flexible chain both of which have no internal structure [113]. Rather our simulations also indicate that the cross-linked arrangement alone of the TC molecules within the fibril may induce an intrinsic curvature, twist or writhe within the fibril, even though the constituent model TC molecules themselves contain no such intrinsic features. Recall that we

modeled the TC molecules as homogeneous discrete worm-like chains. This phenomenon hints at a possible design principle of Nature, that by means of special arrangements of simple building blocks, new properties can emerge in the larger scale structures made from these building blocks that are not necessarily intrinsic to the building blocks themselves. This, indeed, is what was already borne out by the simple architectures consisting of three WLC's we considered in Chapter 5. In contrast, recently a macroscale writhing effect in bundles of polymers, originating from the helicity of the constituent polymers, has been proposed [118]. Intrinsic curvature is apparent in our model from the snapshots of Figure 6.19 where even though the fibril is bent, it is considerably skewed to one side transverse to the bending force, and the one-sidedness of this conformation persisted throughout the simulation. This observation of intrinsic curvature appears also to be consistent with AFM images of fibrils [111] obtained in the laboratory. We note however the possibility that in most AFM slides the fibrils under observation are necessarily forced onto a flat plane so that their intrinsic curvature is lost and may go undetected. The crystal structure specified by Orgel *et al.* [4] which was determined by synchrotron X-ray analysis of rat-tail collagen *in situ*, and that we used to generate the initial state of the fibril already has a chiral character to its arrangement. The twist stored in this crystal structure could be the source of the intrinsic curvature and twist of the fibril. However, we note that our model for tropocollagen could be incomplete due to the fact that we used an achiral model for the TC molecules which themselves could be intrinsically chiral.

6.5.3 Possible Additional Contributions to Fibril Mechanics

Due to the smooth continuous cylindrical geometry of the interaction potentials used for our model TC molecules, the shear resistance in the fibril, which is the force that nearest neighbouring TC molecules feel when they slide past one another, is small, being proportional to the rate of change in overlap potential with change in relative position of the TC molecules. The only things keeping the TC molecules from sliding off past each other are the rigid, but freely-jointed cross-links. In reality, shear resistance is a result of the discrete intermolecular bonds between the TC molecules that break and reform when TC molecules slide past one another. Thus, to first order, the shear force must be proportional to the length of contact line between two nearest neighbouring TC molecules. Using this picture, Buehler [27] has proposed a model of collagen fibrils that takes these considerations into account, postulating two regimes of intermolecular shear: first, a homogeneous shear regime, in which the shear force is proportional to the contact length between parallel neighbouring fibrils, and acts uniformly along the entire contact line, and second, a slip-pulse propagation regime which is due to the nucleated breaking of intermolecular bonds, and which evolves in a manner akin to the propagation of cracks in bulk materials. In future work we will consider homogeneous in-

termolecular shear, for which it would be more advantageous to use spherical overlap potentials located at various fixed positions along the contour of each TC molecule. Or perhaps another way such shear forces could be built into each TC molecule would be through a predetermined sequence of dipoles situated along the contour of the TC molecule, which coarse-grains the zwitterionic arrangement of amino-acids along the TC molecule, and therefore introduces some heterogeneity into the TC molecule. Studies of such charge clusters along the contour of TC molecules have been undertaken and are thought to lead to the staggered arrangement of the TC molecules with respect to each other [94, 119]. Note also that dipoles are thought to be the source of the observed piezoelectricity of collagen fibrils [5].

Understanding how bending occurs in fibrils is important for the biological functions of cells, such as fibroblasts and chondrocytes which have been observed to bend and pull on fibrils [120]. The results of our bending experiments in the simulations indicate that our model fibril is very compliant to transverse forces, that is, it takes forces of very little magnitude to bend it, despite the fact that it is fully cross-linked. This may point to some significant departures of actual values of molecular parameters from the ones we have been using. A likely culprit is the persistence length ℓ_p of the TC molecule: we have been using a nominal value of $\ell_p = 8$ nm (see Figure 6.2) which is on the lower end of the range of reported measured values (14.1 ± 7.6 nm [7]). In future work, we will investigate the changes in bending modulus with changes in persistence length of tropocollagen.

6.5.4 Molecular Crimp and Length Storage

One advantage that computer simulations offer is a higher resolution of the conformations of the TC molecules within the fibril which would otherwise be difficult to observe in the laboratory. We find that upon thermal relaxation and owing to their great flexibility, the individual confined TC molecules adopt short-wavelength crimped conformations superimposed on a nearly full-length end-to-end distance conformation (see Figure 6.25). We surmise that they are able to afford this crimped conformation, first of all, due to the ambient temperature, and secondly, by compensating for the increase in bending energy with a lowering of the total fibril energy by sticking closer to (or aligning with) their neighbours. This molecular crimping (as opposed to the macroscopic crimp of entire collagen fibers) is unlikely to show up in X-ray scattering images, but may nonetheless play a role in the low-strain mechanical response. As such, they could be responsible for some of the softness of our fibrils.

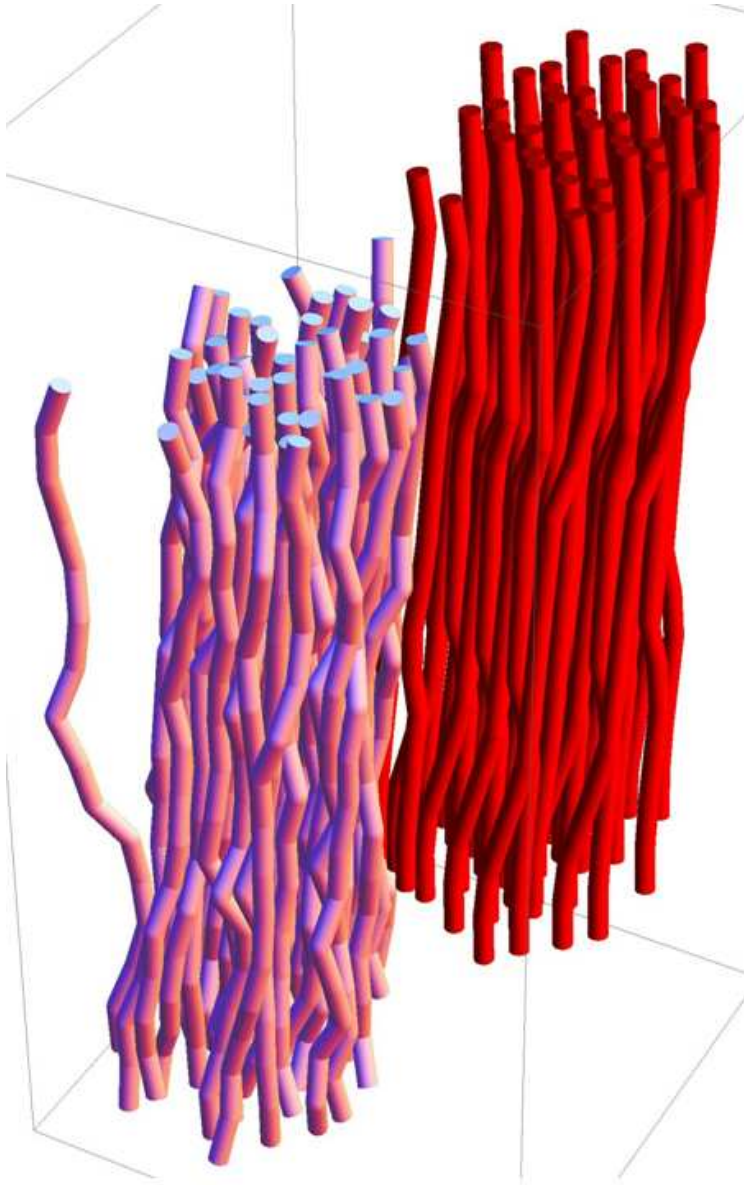


Figure 6.25: A section of the simulated collagen fibril before (*right*) and after (*left*) thermal relaxation. Upon thermal relaxation, and owing to their great flexibility, the individual confined TC molecules adopt short-wavelength crimped conformations superimposed on a nearly full-length end-to-end distance conformation.

6.5.5 Appropriateness of Timoshenko Framework

As we have suggested, the Timoshenko beam model is neither complete nor sufficient to represent the full mechanical analysis of the fibril. We suggest that a good analytical model for collagen must account for the intrinsic curvature and twist of the fibril, anisotropy and the possible coupling between stretching, twisting, and bending. It must also treat fluctuations of its constituent TC molecules. This, to our knowledge, has not been achieved or attempted and therefore, the appropriate continuum model to represent collagen does not yet exist. However, with these simulations, we now nonetheless have access to its full response. Existing theories of polymers that take some of these features into account are the double-stranded DNA models [121] and the special Cosserat elasticity models [122, 111], and these we suggest are promising starting points for an effective model of the collagen fibril.

6.6 Summary and Outlook

In this chapter, we have described a MCMC computational framework that enables various mechanical experiments to be performed on a mesoscopic model of collagen fibrils. While we have achieved what we set out to do, yet, at the same time we realize that our quest for a full understanding of the mechanics of collagen fibrils has only just begun. So far our focus has only been on bending collagen fibrils. Further (numerical) mechanical experiments and structural investigations will need to be performed on the collagen fibril in order to establish the essential aspects of its mechanical behaviour.

Simulations of the collagen fibril were necessitated by the current lack of an existing analytical model for collagen fibrils that captures all the relevant mechanical aspects of the fibril. This need for simulation has been only further reinforced by our own inability to fit the mechanical behaviour derived from the simulation of our model fibril with the Timoshenko beam model, which features only bending, shear, and axial stretching moduli. Our results suggest that a good coarse-grained model for the collagen fibril must also include helicity and transverse anisotropy. It is likely that more fit parameters will yield better fits, but this work is not about minimal models, it is about a faithful model.

TRACTRIX, the methodology set out here, is designed with collagen in mind. But it is, in fact, much more widely applicable. In particular, with self-avoidance and topological constraint algorithms to bolster it, it promises to be even more powerful as a simulation technique whenever polymers are involved. Several groups, recognizing the far-reaching possibilities of the moves that TRACTRIX provides, have already expressed their interest in it, and we look forward to seeing to what other uses it will be put in the future.

6.A Jacobian Calculations

Here we outline the technicalities involved in the computation of the Jacobian determinant $\det \mathcal{J}_{AB}$ for $\mathcal{T}_{AB}(\mathcal{R})$.

Owing to the nonlinearity of the $\mathcal{T}_A(\Delta)$ -based transformations, a simple closed-form expression for their Jacobian determinants is hard to obtain. We therefore choose to determine the elements of the corresponding Jacobian matrices and then compute their determinants numerically, using for example a fast *LU*-decomposition routine. However, in the case of $\mathcal{T}_{AB}(\mathcal{R})$ a few simplifying shortcuts can be exploited to minimize the total number of evaluations.

First of all, we recognize that in d -dimensions the Jacobian matrix \mathcal{J}_{AB} can be written down as block matrix, each block being a $d \times d$ matrix. The square block located at the i -th block row and j -th block column of \mathcal{J}_{AB} is the matrix $\frac{\partial \mathbf{r}_i^{(s+1)}}{\partial \mathbf{r}_j^{(s)}}$, where $\mathbf{r}_j^{(s)}$ is the position of the j -th mass-point in the current state s of the system, and $\mathbf{r}_i^{(s+1)}$ is the position of the i -th mass-point in the newly proposed state $s + 1$ of the system.

Next, we note that the number of block rows (or block columns) of \mathcal{J}_{AB} need only be as large as the number of mass-points in the system that are actually moved during the simulation step, since the stationary mass-points only contribute an overall factor of unity to the Jacobian determinant.

Furthermore, knowing that the absolute value of the determinant of a matrix does not change when any two of its rows (or columns) are interchanged, we may always rearrange the rows and columns of \mathcal{J}_{AB} so that its first few rows and columns correspond only with the displaced driver nodes of $\mathcal{T}_{AB}(\mathcal{R})$.

Recalling the transformation steps of $\mathcal{T}_{AB}(\mathcal{R})$ from Subsection 6.3.4, we find that the new position of each displaced driver node is completely independent of all the other mass-points in the system. This independence assigns a zero to each matrix component in these first few rows and columns, except for the $d \times d$ blocks along the diagonal of a sub-matrix at the top-left corner of \mathcal{J}_{AB} . Each block on the diagonal is equal to $\mathcal{O}_{(\theta, \hat{\mathbf{u}})}$ if \mathcal{R} is a rigid-body rotation [see Equation (6.9)], or equal to the d -dimensional identity matrix $\mathbf{1}_d$ if \mathcal{R} is a translation [see Equation (6.8)]. Consequently, this entire sub-matrix contributes a trivial factor of unity to $\det \mathcal{J}_{AB}$ since $\det \mathcal{O}_{(\theta, \hat{\mathbf{u}})} = \det \mathbf{1}_d = 1$.

The above argument applies not only to the displaced driver nodes but also to any other mass-point in the system whose position is transformed by the direct application of \mathcal{R} .

Now, with the driver nodes accounted for, \mathcal{J}_{AB} can be reduced in size so that its rows and columns now correspond only with the positions of those mass-points belonging to the $\mathcal{T}_A(\Delta)$ -deformed linear chain fragments connected to the driver nodes. Again, as far as $\mathcal{T}_{AB}(\mathcal{R})$ is concerned, the new position of any mass-point belonging to a given linear fragment is completely independent of any mass-point on any other chain in the system. Therefore,

the rows and columns of this reduced Jacobian matrix may once again be rearranged in order to group together all block rows and block columns corresponding to the same linear fragment. This process leads to yet another block-diagonal matrix with the size of each square block on the diagonal being d times one less than the number of mass-points (recall that each linear fragment had one driver node which has already been accounted for above) on its corresponding linear fragment. The determinant $\det \mathcal{J}_{AB}$ is therefore finally reduced to the product:

$$\det \mathcal{J}_{AB} = \prod_{\mathcal{A}} \det \mathcal{J}_{\mathcal{A}} \prod_{\mathcal{F}} \det \mathcal{J}_{\mathcal{F}}, \quad (6.11)$$

where the first product is of all Jacobian determinants $\mathcal{J}_{\mathcal{A}}$ of the transformations $\mathcal{T}_{\mathcal{A}}(\Delta)$ on all anchored linear chain fragments \mathcal{A} and the second product is of all Jacobian determinants $\mathcal{J}_{\mathcal{F}}$ of the transformations $\mathcal{T}_{\mathcal{F}}(\delta)$ on all free linear chain fragments \mathcal{F} (see subsection 6.3.4).

The computation of the Jacobian determinant $\det \mathcal{J}_{\mathcal{A}}$ of $\mathcal{T}_{\mathcal{A}}(\Delta)$ has already been outlined in Chapter 4 while that of $\det \mathcal{J}_{\mathcal{F}}$ is given below.

Now the Jacobian determinant $\det \mathcal{J}_{\mathcal{F}}$ (for the TRACTRIX transformation for a free chain) is relatively easy to find: for as far as $\mathcal{T}_{\mathcal{F}}(\delta)$ is concerned, the new position $\mathbf{r}_i^{(s+1)}$ of any mass-point P_i on the linear chain fragment is determined only by the positions of all mass-points along the chain between P_i and the driver node P_0 inclusive (see Chapter 4):

$$\begin{aligned} \mathbf{r}_0^{(s+1)} &= \mathbf{r}_0^{(s)} + \delta, \\ \mathbf{r}_i^{(s+1)} &= \chi_{\text{T}}(\mathbf{r}_i^{(s)}, \mathbf{r}_{i-1}^{(s)}, \mathbf{r}'_{i-1}^{(s)} - \mathbf{r}_{i-1}^{(s)}, f), \end{aligned} \quad (6.12)$$

where here the index i runs over the mass-points from 1 to N_f , and N_f is the total number of bonds of the linear chain. The function χ_{T} is the discrete tractrix transformation defined by

$$\chi_{\text{T}}(\mathbf{r}_i^{(s)}, \mathbf{r}_{i-1}^{(s)}, \delta_{i-1}, f) \equiv \mathbf{p}_i + 2\mathbf{w}_i \frac{\mathbf{t}_i \cdot \mathbf{w}_i}{\mathbf{w}_i \cdot \mathbf{w}_i} \quad (6.13)$$

where $\mathbf{p}_i = \mathbf{r}_{i-1}^{(s+1)} - \mathbf{t}_i$ and $\mathbf{w}_i = f\mathbf{r}_i^{(s)} + (1-f)\mathbf{r}_{i-1}^{(s)} - \mathbf{r}_{i-1}^{(s+1)}$ ¹¹. This gives rise to a lower d -block-triangular Jacobian matrix if the d -block rows and d -block columns are arranged in the same order in which their corresponding mass-points appear along the linear chain, beginning with the mass-point nearest the driver node, and going from top to bottom (for the rows), and from left to right (for the columns).

¹¹The free parameter f featured in these equations is one whose value may be chosen before the start of the simulation and thereafter held constant. Qualitatively, f controls the amount of translation, as opposed to rotation, that each bond undergoes during the action of $\mathcal{T}_{\mathcal{F}}(\delta)$: the higher its value, the less each bond rotates and the more the chain is merely rigidly translated. Thus, by adjusting the value of f to match the stiffness of the linear chain under consideration one can, in principle, improve acceptance rates of the simulation.

Then $\det \mathcal{J}_F$ is simply the product of determinants of the d -block matrices along the diagonal:

$$\det \mathcal{J}_F = \prod_{i=1}^{N_f} \left\| \frac{\partial \mathbf{r}_i^{(s+1)}}{\partial \mathbf{r}_i^{(s)}} \right\| \quad (6.14)$$

where again the index i runs over all mass-points of the free linear chain (excluding that of the driver node P_0 which has already been accounted for above, and which otherwise would have contributed a trivial factor of unity to the determinant).

For further details, we refer the reader to the C++ codes implementing the above formulae. These codes are provided as supplementary material and can be found at Ref. [65].

CHAPTER 7

CONCLUSIONS AND OUTLOOK

The central question we wanted to address at the beginning of this thesis was whether we may understand the mechanical response of collagen in a manner that respects and exploits its multiple length-scales. In this chapter we briefly highlight the successes we made towards achieving this goal, and also suggest new directions for further research.

7.1 Conclusions

In this thesis, we reviewed (in Chapter 2) the salient theoretical aspects of the statistical mechanics and continuum mechanics of biopolymeric materials that were relevant to our cause: namely, the multiscale modeling of the mechanics of collagenous tissue.

We also reviewed Markov Chain Monte Carlo methods (Chapter 3) and successfully developed a new Markov Chain Monte Carlo technique, namely TRACTRIX, for simulating the mechanics of cross-linked networks of polymers, particularly networks of freely-jointed chains or discrete worm-like chains (Chapter 4). This method is able to preserve, throughout the simulation, the network's topology (with or without closed loops), while at the same time preserving the fixed contour length requirements and local inextensibility constraints of the linear chain fragments that make up the network. Thus one is able to fully exploit the softest modes of deformation (that is, the bending modes of the constituent linear chains of the network), which are most susceptible to thermal agitation and therefore most relevant for the low strain mechanics of these networks, without ever having to stretch the individual bonds that should remain rigid during the deformation.

TRACTRIX was validated through particular tests we conducted: we simulated various freely-jointed chain architectures whose properties could be predicted theoretically (Chapter 5). The results of these simulations were in exact agreement with their theoretical predictions. Furthermore, for single stiff worm-like chains we found close agreement of the end-to-end distance probability distribution (obtained through simulation) with its theoretical estimates (Chapter 5) evaluated using the semi-flexible chain model [32].

Results of other simulations of bundles of a few discrete worm-like chains hinted at a design principle underlying the cross-linked macromolecular structures found in nature: that nature may create supramolecular filaments of tunable effective stiffness by using only two kinds of molecules at its disposal: long identical chain molecules and short cross-linking proteins applied in varying concentrations.

Finally, in accordance with our central goal, we also used TRACTRIX to simulate a cross-linked collagen fibril, which is a special case of an anisotropic network of polymers. This simulation demonstrated the unique capability of TRACTRIX to effect moves that deform several polymers at once in a controlled way. In this particular case, polymers spanning the entire cross-section of the fibril could be deformed enabling the efficient transversal of phase space.

In order to do this simulation, we developed a mesoscopic computational model for the collagen fibril which took into account a recently proposed [4] crystalline structure governing the arrangement of tropocollagen molecules within the fibril. The tropocollagen molecules were themselves represented as discrete worm-like chains with nominal values for its dimensions and persistence length, all of which were taken from experimental measurements (see

Table 6.1). Furthermore, the bonds of the tropocollagen molecules were endowed with a hardcore interaction potential to prevent any two tropocollagen molecules from occupying the same region of space, and with an attractive overlap potential which aided in maintaining the alignment of neighbouring tropocollagen (TC) molecules with each other, thus effectively maintaining a high aspect ratio collagen fibril. By performing numerical experiments that mimicked the bending of the fibril and comparing the resulting bent profile with that of a tip-loaded cantilever of the same dimensions, we were able to obtain estimates of the bending modulus of the collagen fibril.

7.2 Outlook

Our research sets the stage for further investigation into the origins of the mechanics of collagen fibrils. In this section, we therefore suggest possible new directions for further research. Along the way, we also outline some of the limitations of TRACTRIX that may need to be examined and overcome.

7.2.1 Limitations and Suggestions for TRACTRIX (Chapter 4)

- We showed, in Chapter 4, that despite its advantages TRACTRIX, by itself, is unable to maintain the ambient isotopy of three-dimensional cross-linked networks which possess closed loops. This means that any entanglements between closed loops, that ought to remain permanently trapped within a network, can become ‘undone’ during the simulation of the network by TRACTRIX. This unphysical feature can be prevented by making use of a suitable topological invariant to determine whether a MCMC move violates ambient isotopy or not. Though we suggested an algorithm that uses the Gauss Linking Number as the topological invariant, we admit that its use only partially solves this problem. Therefore further research is required to identify or construct a universal topological invariant that can be efficiently computed to fully address this problem.¹
- Another obvious limitation of TRACTRIX is that, having been designed as a MCMC method, simulations that employ it are unable to provide any dynamic information at all. Nevertheless, because TRACTRIX moves are somewhat similar to truly physical moves (for example, the dragging of a polymer), it is plausible that TRACTRIX could be calibrated against real time so that TRACTRIX could then be used as input for Kinetic

¹This problem has been submitted to certain members of the Mathematics Department at the Eindhoven University of Technology, who have shown serious interest in the problem, resulting in a research proposal aimed at solving this very problem.

Monte Carlo algorithms that utilize this time calibration to provide time rate information. This could turn out to be a viable alternative to MD simulations of polymeric networks, and enable, for example, the study of fibril deformation with loading rate and the measurement of the viscoelastic properties of the fibril. MCMC time-calibrations have been performed for some other types of moves often used in simulations of point particle systems [50, 123].

- TRACTRIX is in essence a constraint algorithm, hence it is not designed to efficiently avoid overlap between the different bonds of polymers. Indeed we saw in Chapter 6 that when excluded volume interactions are enforced, very low acceptance rates for TRACTRIX moves are obtained, which led to long simulation times in order to obtain good statistics. This undesirable feature is a consequence of the dense structure of TC molecules within the fibril which increases the likelihood for overlap with other TC molecules whenever any TC molecule is deformed.

We expect that by combining TRACTRIX with other specialized moves, such as the Fixed-Ends Configurational-Bias moves or Recoil-Growth algorithm [50], one might be able to improve these acceptance rates, since these other moves are designed (exploiting the so-called super-detailed balance principle) to more efficiently avoid overlap.

- TRACTRIX may provide an advantage over existing free-energy minimization methods [124] for computing the mechanical response of polymeric networks (such as random isotropic networks) to applied stress. This is because the full network architecture is retained in the simulation along with the conformations of the linear chains interlinking the cross-link positions, hence no additional model need be introduced to describe the free-energy of the network. Moreover, since cross-links are also allowed to fluctuate about their average positions, the effects of both non-affinity and cross-link fluctuations to the elasticity of the network can be explored.

7.2.2 Collagen Fibril (Chapter 6)

- The values of the Young's modulus of the collagen fibril obtained from our simulation were of the order of a few 10 MPa. These values are in qualitative agreement with those lying at the lower end of the range of measured experimental values of Young's moduli reported in the literature for reconstituted collagen fibrils [113, 115]. The question therefore arises as to what can be done in order to reach the values of Young's

modulus that lie at the higher end of the spectrum. Possible directions include:

1. increasing the bending modulus κ of the TC molecules (see Section 6.2.1),
 2. tuning the radius r_c or the cohesive energy density of the attractive overlap potential (see Section 6.2.3),
 3. tuning the radius r of the hardcore potential (see Section 6.2.2) to decrease the spacing between the TC molecules within the fibril,
 4. modifying the interaction potential between TC molecules so as to produce a shear force proportional to the contact lengths between neighbouring TC molecules, in a manner similar to the continuum model of Buehler [27]. This may be done by using spherical overlap potentials centered at various fixed positions along the contour of each TC molecule. This procedure will invariably introduce an additional length scale — the average contour distance between these attractive spherical centers — through which neighbouring TC molecules will have to slide to overcome the energetic barriers imposed by these potentials.
- Since the building blocks of tropocollagen molecules are amino acids, which are dipolar or develop a partial charge separation when dissolved in aqueous solution, one way to introduce shear forces between neighbouring tropocollagen molecules without having to introduce additional degrees of freedom, would be to assign to each tropocollagen molecule a predetermined sequence of dipole moments directed along the bonds of the TC molecule, which coarse-grains the zwitterionic arrangement of amino-acids along the TC molecule, and therefore introduces some heterogeneity into the TC molecule. Various dipolar sequences have been proposed for tropocollagen [94, 119] which could serve as a starting point for such an investigation. Such a study could at the same time prove very useful in determining the resulting pyroelectric and piezoelectric properties of collagen fibrils [5].
 - So far our tests have mimicked only the bending deformations of the fibril. Further tests that mimic the stretching of the fibril will need to be performed in order to produce force-extension curves for comparison with those obtained experimentally [114]. This would serve as a means of further validating our computational model.

- It is now easy to extend the current model to study the twisting response of collagen fibrils. All that is required is to apply a torque instead of a force. For these studies it will be instructive to also endow the tropocollagen molecules with a chiral interaction potential reflecting their intrinsic chirality which originates from their helical structure. Recently, theoretical models of bundles of chiral or achiral polymers [106, 118] have been proposed. These models could serve as a means of comparison and validation for our computational model.
- A significant amount of backbone (or axial) fluctuations of the fibril were observed during the simulation. This is most likely due to the small diameter we chose for the fibril. It would be instructive to determine how quickly these fluctuations are suppressed with the increase in diameter of the fibril. However, the issue of lower acceptance rates will be a drawback to this investigation unless it is somehow addressed as suggested in the last bulleted item of the previous subsection.

BIBLIOGRAPHY

- [1] P. M. Chaikin and T. C. Lubensky, *Principles of Condensed Matter Physics*, reprint ed. (Cambridge University Press, Cambridge, United Kingdom, 2000).
- [2] E. Strauss, *Studien über die Albuminoide mit besonderer Berücksichtigung des Spongins und der Keratine* (Karl Winters Universitäts-Buchhandlung, Heidelberg, 1904).
- [3] J. Harris and A. Reiber, *Micron* **38**, 513 (2007).
- [4] J. P. R. O. Orgel, T. C. Irving, A. Miller, and T. J. Wess, *Proceedings of the National Academy of Sciences* **103**, 9001 (2006).
- [5] M. Minary-Jolandan and M.-F. Yu, *Nanotechnology* **20**, 085706 (2009).
- [6] H. K. Ravi, F. Simona, J. Hulliger, and M. Cascella, *The Journal of Physical Chemistry B* **116**, 1901 (2012).
- [7] Y.-L. Sun, Z.-P. Luo, A. Fertala, and K.-N. An, *Biochemical and Biophysical Research Communications* **295**, 382 (2002).
- [8] P. Fratzl, *Collagen : Structure and Mechanics* (Springer US, Berlin, 2008).
- [9] M. D. Shoulders and R. T. Raines, *Annual Review of Biochemistry* **78**, 929 (2009).
- [10] K. E. Kadler, Y. Hojima, and D. J. Prockop, *Journal of Biological Chemistry* **262**, 15696 (1987).
- [11] D. Brazel, I. Oberbäumer, H. Dieringer, W. Babel, R. W. Glanville, R. Deutzmann, and K. Kühn, *European Journal of Biochemistry* **168**, 529 (1987).
- [12] J. A. Ramshaw, N. K. Shah, and B. Brodsky, *Journal of Structural Biology* **122**, 86 (1998).
- [13] D. Hulmes, T. Wess, D. Prockop, and P. Fratzl, *Biophysical Journal* **68**, 1661 (1995).

- [14] H. Suhonen, M. Fernández, R. Serimaa, and P. Suortti, *Physics in Medicine and Biology* **50**, 5401 (2005).
- [15] L. Bozec and M. Horton, *Biophysical Journal* **88**, 4223 (2005).
- [16] J. Doucet, F. Briki, A. Gourrier, C. Pichon, L. Gumez, S. Bensamoun, and J.-F. Sadoc, *Journal of Structural Biology* **173**, 197 (2011).
- [17] J. Charvolin and J.-F. Sadoc, *Biophysical Reviews and Letters* **6**, 13 (2011).
- [18] D. E. Rivett, W. C. W., L. M. Belkin, R. J. A. M., and W. J. F. K., in *The Lennox Legacy* (CSIRO Publishing, Collingwood, Australia, 1996), p. 65.
- [19] K. Okuyama, H. P. Bächinger, K. Mizuno, S. Boudko, J. Engel, R. Berisio, and L. Vitagliano, *Acta Crystallographica Section D* **65**, 1007 (2009).
- [20] P. Xu, E. Kable, C. J. R. Sheppard, and G. Cox, *Chinese Optics Letters* **8**, 213 (2010).
- [21] M. Raspanti, V. Ottani, and A. Ruggeri, *International Journal of Biological Macromolecules* **11**, 367 (1989).
- [22] N. S. Murthy, *Biopolymers* **23**, 1261 (1984).
- [23] F. O. Schmitt, *Rev Mod Phys* **31**, 349 (1959).
- [24] K. Altgelt, A. J. Hodge, and F. O. Schmitt, *Proceedings of the National Academy of Sciences of the United States of America* **47**, 1914 (1961).
- [25] D. R. Eyre and J.-J. Wu, in *Collagen*, Vol. 247 of *Topics in Current Chemistry*, edited by J. Brinckmann, H. Notbohm, and P. K. Müller (Springer, Berlin / Heidelberg, 2005), pp. 207–229.
- [26] M. Raspanti, A. Alessandrini, V. Ottani, and A. Ruggeri, *Journal of Structural Biology* **119**, 118 (1997).
- [27] M. J. Buehler, *Proceedings of the National Academy of Sciences of the United States of America* **103**, 12285 (2006).
- [28] Y. Tang, R. Ballarini, M. J. Buehler, and S. J. Eppell, *Journal of The Royal Society Interface* **7**, 839 (2010).
- [29] R. G. Larson, *Molecular Physics: An International Journal at the Interface Between Chemistry and Physics* **102**, 341 (2004).
- [30] O. Kratky and G. Porod, *Recueil des Travaux Chimiques des Pays-Bas* **68**, 1106 (1949).
- [31] J. F. Marko and E. D. Siggia, *Macromolecules* **28**, 8759 (1995).

- [32] J. Wilhelm and E. Frey, *Physical Review Letters* **77**, 2581 (1996).
- [33] C. Storm and P. C. Nelson, *Physical Review E* **67**, 051906 (2003).
- [34] C. Storm, J. J. Pastore, F. C. MacKintosh, T. C. Lubensky, and P. A. Janmey, *Nature* **435**, 191 (2005).
- [35] E. M. Huisman, C. Storm, and G. T. Barkema, *Physical Review E* **78**, 051801 (2008).
- [36] B. A. DiDonna and T. C. Lubensky, *Physical Review E* **72**, 066619 (2005).
- [37] C. Heussinger, B. Schaefer, and E. Frey, *Physical Review E* **76**, 031906 (2007).
- [38] J. Liu, G. H. Koenderink, K. E. Kasza, F. C. MacKintosh, and D. A. Weitz, *Physical Review Letters* **98**, 198304 (2007).
- [39] J. M. Gere and S. P. Timoshenko, *Mechanics of Materials*, 4th edition ed. (PWS Publishing Company, Boston, USA, 1997).
- [40] E. Reissner, *Zeitschrift für Angewandte Mathematik und Physik* **23**, 795 (1972).
- [41] I. Tetsuo, *Computers & Structures* **34**, 239 (1990).
- [42] J. R. Hutchinson, *Journal of Applied Mechanics* **68**, 87 (2001).
- [43] H. Irschik and J. Gerstmayr, *Mathematical and Computer Modelling of Dynamical Systems* **17**, 19 (2011).
- [44] T. Kaneko, *Journal of Physics D: Applied Physics* **8**, 1927 (1975).
- [45] J.J. and Jensen, *Journal of Sound and Vibration* **87**, 621 (1983).
- [46] L. F. Shampine, M. W. Reichelt, and J. Kierzenka, (published online: http://www.mathworks.com/bvp_tutorial) (2002).
- [47] S. Nosé, *The Journal of Chemical Physics* **81**, 511 (1984).
- [48] W. G. Hoover, *Physical Review A* **31**, 1695 (1985).
- [49] M. Parrinello and A. Rahman, *Physical Review Letters* **45**, 1196 (1980).
- [50] D. Frenkel and B. Smit, *Understanding molecular simulation* (Academic Press, Inc., Orlando, Florida, USA, 2001).
- [51] M. E. J. Newman and G. T. Barkema, *Monte Carlo Methods in Statistical Physics* (Oxford University Press, USA, Oxford, United Kingdom, 1999).
- [52] P. Attard, *Physical Review E* **80**, 041126 (2009).

- [53] X. Xing, P. M. Goldbart, and L. Radzihovsky, *Physical Review Letters* **98**, 075502 (2007).
- [54] S. Meyn and R. Tweedie, *Markov chains and stochastic stability, Communications and control engineering* (Cambridge University Press, Cambridge, United Kingdom, 2009).
- [55] M. Doi and S. Edwards, *The theory of polymer dynamics* (Oxford University Press, Oxford, United Kingdom, 1988).
- [56] J.-P. Ryckaert, G. Ciccotti, and H. J. C. Berendsen, *Journal of Computational Physics* **23**, 327 (1977).
- [57] H. C. Andersen, *Journal of Computational Physics* **52**, 24 (1983).
- [58] C. McBride, M. R. Wilson, and J. A. K. Howard, *Molecular Physics* **93**, 955 (1998).
- [59] L. R. Dodd, T. D. Boone, and D. N. Theodorou, *Molecular Physics* **78**, 961 (1993).
- [60] V. G. Mavrantzas, in *Handbook of Materials Modeling*, edited by S. Yip (Springer Netherlands, Dordrecht, 2005), section 9.4, pp. 2583–2597.
- [61] E. Leontidis, J. de Pablo, M. Laso, and U. Suter, *Atomistic Modeling of Physical Properties* **116**, 283 (1994).
- [62] A. C. Maggs, *Physical Review Letters* **97**, 197802 (2006).
- [63] T. Hoffmann, in *Consortium “Math for industry”. First forum, Tokyo, Japan, September 16-17, 2008*. (Fukuoka:, Kyushu University, Faculty of Mathematics, 2008), pp. 45–51.
- [64] T. Hoffmann, in *Discrete Differential Geometry, Oberwolfach Seminars*, edited by A. I. Bobenko, P. Schröder, J. M. Sullivan, and G. M. Ziegler (Birkhauser Verlag AG, Basel/Switzerland, 2008), Vol. 38, pp. 95–115.
- [65] (soon to be published online) .
- [66] L. H. Kauffman, in *On knots* (Princeton University Press, Princeton, New Jersey, 1987), p. 9.
- [67] L. H. Kauffman, *Transactions of the American Mathematical Society* **311**, pp. 697 (1989).
- [68] E. J. J. van Rensburg and S. G. Whittington, *Journal of Physics A: Mathematical and General* **24**, 5553 (1991).
- [69] E. Orlandini and S. G. Whittington, *Reviews of Modern Physics* **79**, 611 (2007).

- [70] M. Lang, W. Michalke, and S. Kreitmeier, *Journal of Computational Physics* **185**, 549 (2003).
- [71] H. Brunn, *Zeitschrift für Mathematik und Physik* **37**, 106 (1892).
- [72] M. de Berg, M. van Kreveld, M. Overmars, and O. Schwarzkopf, *Computational Geometry: Algorithms and Applications*, 2nd ed. (Springer-Verlag, Berlin, Heidelberg, 2000), p. 367.
- [73] R. L. Jernigan and P. J. Flory, *The Journal of Chemical Physics* **50**, 4185 (1969).
- [74] L. R. G. Treloar, *Transactions of the Faraday Society* **42**, 77 (1946).
- [75] N. Becker, A. Rosa, and R. Everaers, *The European Physical Journal E: Soft Matter and Biological Physics* **32**, 53 (2010).
- [76] C. Heussinger, M. Bathe, and E. Frey, *Physical Review Letters* **99**, 048101 (2007).
- [77] M. J. Buehler and S. Y. Wong, *Biophysical Journal* **93**, 37 (2007).
- [78] D. W. L. Hukins, *Journal of Theoretical Biology* **71**, 661 (1978).
- [79] S. Leikin, D. C. Rau, and V. A. Parsegian, *Nature Structural & Molecular Biology* **2**, 205 (1995).
- [80] I. Streeter and N. H. de Leeuw, *Soft Matter* **7**, 3373 (2011).
- [81] A. Gautieri, S. Vesentini, A. Redaelli, and M. J. Buehler, *Nano Letters* **11**, 757 (2011).
- [82] H. Park and R. Lakes, *Journal of Biomechanics* **19**, 385 (1986).
- [83] T. Odijk, *Macromolecules* **16**, 1340 (1983).
- [84] W. Folkhard, E. Mosler, W. Geercken, E. Knörzer, H. Nemetschek-Gansler, T. Nemetschek, and M. Koch, *International Journal of Biological Macromolecules* **9**, 169 (1987).
- [85] N. Sasaki and S. Odajima, *Journal of Biomechanics* **29**, 1131 (1996).
- [86] J. Skolnick and M. Fixman, *Macromolecules* **10**, 944 (1977).
- [87] T. Odijk, *Journal of Polymer Science: Polymer Physics Edition* **15**, 477 (1977).
- [88] D. L. Bodian, R. J. Radmer, S. Holbert, and T. E. Klein, *Pacific Symposium on Biocomputing* **16**, 193 (2011).

- [89] G. Cameron, D. Cairns, and T. Wess, *Journal of Molecular Biology* **372**, 1097 (2007).
- [90] R. L. C. Vink and T. Schilling, *Phys. Rev. E* **71**, 051716 (2005).
- [91] C. Vega and S. Lago, *Computers and Chemistry* **18**, 55 (1994).
- [92] D. L. Beveridge and G. W. Schnuelle, *The Journal of Physical Chemistry* **79**, 2562 (1975).
- [93] D. J. Hulmes, A. Miller, D. A. Parry, K. A. Piez, and J. Woodhead-Galloway, *Journal of Molecular Biology* **79**, 137 (1973).
- [94] B. L. Trus and K. A. Piez, *Journal of Molecular Biology* **108**, 705 (1976).
- [95] E. Suárez, N. Díaz, and D. Suárez, *The Journal of Physical Chemistry B* **112**, 15248 (2008).
- [96] E. Suárez, N. Díaz, and D. Suárez, *Journal of Chemical Theory and Computation* **5**, 1667 (2009).
- [97] S. Asakura and F. Oosawa, *Journal of Polymer Science* **33**, 183 (1958).
- [98] D. Marenduzzo, K. Finan, and P. R. Cook, *Journal of Cell Biology* **175**, 681 (2006).
- [99] K. Richter, M. Nessling, and P. Lichter, *Biochimica et Biophysica Acta (BBA) - Molecular Cell Research* **1783**, 2100 (2008).
- [100] Y. Snir and R. D. Kamien, *Science* **307**, 1067 (2005).
- [101] D. Chandler, *Nature* **417**, 491 (2002).
- [102] J. G. Gay and B. J. Berne, *The Journal of Chemical Physics* **74**, 3316 (1981).
- [103] R. Memmer and F. Janssen, *Journal of the Chemical Society, Faraday Transactions* **94**, 267 (1998).
- [104] B. W. van der Meer, G. Vertogen, A. J. Dekker, and J. G. J. Ypma, *Journal of Chemical Physics* **65**, 3935 (1976).
- [105] S. A. Issaenko, A. B. Harris, and T. C. Lubensky, *Phys. Rev. E* **60**, 578 (1999).
- [106] G. M. Grason and R. F. Bruinsma, *Physical Review Letters* **99**, 098101 (2007).
- [107] O. Pelletier, E. Pokidysheva, L. S. Hirst, N. Bouxsein, Y. Li, and C. R. Safinya, *Phys. Rev. Lett.* **91**, 148102 (2003).
- [108] S. Perumal, O. Antipova, and J. P. R. O. Orgel, *Proceedings of the National Academy of Sciences* **105**, 2824 (2008).

- [109] S. G. Gevorkian, A. E. Allahverdyan, D. S. Gevorgyan, and C.-K. Hu, *Europhysics Letters* **95**, 23001 (2011).
- [110] H. N. W. Lekkerkerker and R. Tuinier, in *Colloids and the Depletion Interaction* (Springer, Heidelberg/Germany, 2011), Chap. 2, p. 62.
- [111] L. Bozec, G. van der Heijden, and M. Horton, *Biophysical Journal* **92**, 70 (2007).
- [112] D. L. Christiansen, E. K. Huang, and F. H. Silver, *Matrix Biology* **19**, 409 (2000).
- [113] J. S. Graham, A. N. Vomund, C. L. Phillips, and M. Grandbois, *Experimental Cell Research* **299**, 335 (2004).
- [114] J. A. J. van der Rijt, K. O. van der Werf, M. L. Bennink, P. J. Dijkstra, and J. Feijen, *Macromolecular Bioscience* **6**, 697 (2006).
- [115] C. A. Grant, D. J. Brockwell, S. E. Radford, and N. H. Thomson, *Biophysical Journal* **97**, 2985 (2009).
- [116] L. Yang, K. O. van der Werf, B. F. Koopman, V. Subramaniam, M. L. Bennink, P. J. Dijkstra, and J. Feijen, *Journal of Biomedical Materials Research Part A* **82A**, 160 (2007).
- [117] L. Yang, K. O. van der Werf, C. F. Fitié, M. L. Bennink, P. J. Dijkstra, and J. Feijen, *Biophysical Journal* **94**, 2204 (2008).
- [118] C. Heussinger and G. M. Grason, *The Journal of Chemical Physics* **135**, 035104 (2011).
- [119] N. Kuznetsova and S. Leikin, *Journal of Biological Chemistry* **274**, 36083 (1999).
- [120] G. Lee and R. Loeser, *Experimental Cell Research* **248**, 294 (1999), cited By (since 1996) 33.
- [121] M. Smith and T. Healey, *International Journal of Non-Linear Mechanics* **43**, 1020 (2008).
- [122] T. J. Healey, *Mathematics and Mechanics of Solids* **7**, 405 (2002).
- [123] C. C. Battaile and D. J. Srolovitz, *Annual Review of Materials Research* **32**, 297 (2002).
- [124] D. A. Head, A. J. Levine, and F. C. MacKintosh, *Phys. Rev. E* **68**, 061907 (2003).

SUMMARY

Multiscale Structure and Mechanics of Collagen

While we are 70% water, in a very real sense collagen is the stuff we are made of. It is the most abundant protein in multicellular organisms, such as ourselves, making up roughly 25% of our total protein content. If you have ever wondered how the human body holds together all its different parts in shape, here is your answer: it is largely due to collagen. Collagen is the main ingredient of so called connective tissue which serves to hold the various parts of the body together. In fact, without collagen we would quite literally fall apart. Some genetic diseases, such as Osteogenesis Imperfecta (brittle bone disease) and Ehlers Danlos syndrome (characterized by abnormally stretchy skin and loose joints), are known to be the result of defective collagen.

One can see why it is necessary to achieve a good understanding of how the strength or mechanical properties of collagen come about, and how it contributes to the state of well-being of an individual. This is essentially the aim of my research.

Despite its relative abundance and about a century of research by many scientists, many features of collagen remain not fully understood. For example, it has been difficult to ascertain the precise structure of collagenous tissue. Nevertheless, a lot of progress has been made during the past couple of decades. Understanding the internal structure of collagen is important since we expect its strength to largely depend on its structure. The tools that physicists use to figure out the structure of biological tissue include advanced microscopes, such as the Atomic Force Microscope and the Electron Microscope, and X-ray diffraction analysis, in which one tries to determine the collagen structure at very small length scales (a billionth of a meter) by observing the fringe patterns made when an X-ray beam is scattered by the atoms that make up collagen (see Figure 1.2). These studies have revealed that there are 28 different types of collagens. The types are numbered with roman numerals I - XXVIII.

In my work I have focused on the most common form of collagen, namely Type I collagen, which occurs mostly in scar tissue, bone and tendon. Tissue made from Type I collagen is made up of atoms that are arranged in such a way that a clear hierarchical structure emerges. This hierarchical organization

is illustrated in Figure 1.1. The hierarchy can be described as follows: approximately 10-20 atoms are grouped together to form amino acids (there are 21 types of amino acids which, incidentally, nature also uses to encode our genetic information). About a 1000 amino acids of mainly two types, Glycine and Proline, are strung together in a special repeating sequence to form polymers, or strands, called alpha helices (which, as the name implies, are shaped like helices, the shape of a spring) which are left-handed. Every three alpha helices associate with one another in a braided conformation that is a right-handed triple-helix called tropocollagen (see Figure 1.1 for an image)². This is the basic building unit of collagen tissue. Certain cells of our bodies, called fibroblasts, are responsible for manufacturing tropocollagen molecules. Inside the body, after a fibroblast makes a tropocollagen molecule, it extrudes the molecule and aids in laying the tropocollagen molecule among other already existing tropocollagen molecules in order to form a long fine bundle known as a fibril. This process can also occur outside the body in the laboratory, unaided by fibroblasts but merely driven by thermal agitation at a particular range of temperatures. This is an example of a process known as self-assembly. The arrangement of tropocollagen molecules within a fibril is 'staggered', somewhat similar to the arrangement of bricks in a brick wall.

In the body, many fibrils occur lying side by side and bundled together to form fibers which are then cross-linked to form part of the connective tissue. Special proteins, known as glycosaminoglycans (GAGs) are responsible for binding the fibrils together. For fibrils self-assembled outside the body and in the absence of GAGs, fibers do not form, but rather a network of fibrils with a well-defined diameter emerges.

While the sequence of atoms that constitute collagen alpha-helices is precisely known, the precise arrangement of tropocollagen molecules within a fibril is difficult to ascertain by experimental means. This is because tropocollagen is a very light and flexible polymer, hence it is constantly changing its bent conformation in response to the erratic bombardment of fast moving atoms of the surrounding medium. This happens even within the closely packed environment of a fibril. Indeed, as the temperature of the surrounding medium increases, the atoms move even faster causing the tropocollagen molecule to wriggle even more. The consequence of this behaviour is that the molecule's resistance to a stretching force increases with increasing temperature, just as for a rubber band when it is heated for example.³ Therefore the apparent randomness of the tropocollagen molecule's wriggling form and motion affects the strength of collagenous tissue at its various levels within its hierarchical organization. In order to quantify this behaviour, special mathematical, or computational models, representing tropocollagen need to be proposed.

²In contrast, DNA which is the polymer responsible for encoding our genetic information is a double helix.

³Contrast this with a metal filament which offers less resistance to stretching when it is heated.

Quantum Physics gives a precise mathematical description of the physical laws that govern how moving atoms interact with each other. One might think that the precise knowledge of all these atoms and how exactly they interact with each other should straightforwardly lead to the explanation and prediction of all possible phenomena in Nature. This may be true, in principle. However since all these interactions have been expressed in terms of mathematical theories and equations whose solutions can be difficult to compute, especially when such large numbers of atoms are simultaneously involved, physicists propose simplistic models called ‘coarse-grained models’ that are easier to manage computationally and that are assumed to encapsulate the essential properties of groups of these atoms. They go on to show by simulations of these models that the phenomena exhibited by these models do not necessarily have to depend on the internal details of the atoms they represent (nor on their interactions).

In this thesis, we developed a coarse-grained model of the tropocollagen molecule that captures the essential features of tropocollagen. These features include its flexibility, its volume, and its tendency to stick to other tropocollagen molecules that come near it. We then generated an entire collagen fibril using many copies of this simplistic model of the tropocollagen molecule and attaching (or cross-linking) them to each other at specific points on the molecules. Then we simulated the entire cross-linked assembly of tropocollagen molecules on a computer at a particular temperature and then attempted to estimate the strength the fibril.

In our coarse-grained model, each tropocollagen molecule was transformed into a chain of about 100 identical rigid sticks (called bonds) but ball-jointed at their ends to one another in a linear sequence (see Figure 7.1). The ease with which the joints could rotate depended on a single quantity known as the bending stiffness of tropocollagen, which has been measured by experiments in the laboratory. This model is called the ‘discrete worm-like chain’.

Because in reality the tropocollagen molecule is constantly wriggling, it is difficult to follow precisely its full motion in time, even on a computer. So we rather chose a statistical treatment. This is where statistical physics and Monte Carlo methods become very useful. Simply put, Monte Carlo methods repeatedly generate sets of random numbers and use them to propose different configurations of the tropocollagen monomers every time. This is somewhat like throwing dice to obtain different numbers every time they are thrown. However, the Monte Carlo method that is employed should take care not to change the lengths of the bonds of the simplistic model, also it must never destroy any of the cross-links in the system.

Prior to this work it has not been possible satisfy all these constraints during the simulation of an arbitrarily cross-linked assembly of coarse-grained polymers. In this thesis, however, we invented a Monte Carlo method that overcomes these issues. We named the method ‘TRACTRIX’, because it is based on

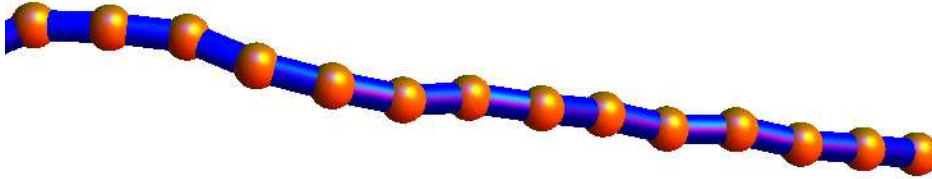


Figure 7.1: The discrete worm-like chain model is essentially a ‘stick-and-ball-joint’ chain. In this thesis, the model was used to represent the tropocollagen molecule for use in computer simulations. All the sticks (here colored blue) are of fixed length. The ease of rotating these sticks with respect to their neighbours depends on the stiffness of the ball-joints, which is related to the bending stiffness of the tropocollagen molecule.

the construction of a special curve which in mathematics is called a tractrix. The tractrix is the answer to the following question: “Given two points linked by a rigid joint, if one point moves along a given curve, how does the other point move?” (See Figure 4.3 for an example of how a tractrix looks like.) The details of this method are described in Chapter 4.

In Chapter 5, we demonstrated that TRACTRIX works, that is, it is accurate and trustworthy, because it reproduced expected results for certain model polymer networks for which we already knew the exact answers.

TRACTRIX was then used to simulate our model of the collagen fibril, and we were thus able to estimate the strength of the collagen fibril. Other interesting results were also established, such as the shape that the fibril finally settled into, and also the average conformation of its constituent tropocollagen molecules. Our model and simulations set the stage for further investigation into the mechanics and other properties of collagen fibrils.

Also this exciting new method TRACTRIX promises to be useful in simulating many different types of biological networks, not only collagen.

PUBLICATIONS

Articles

1. Amuasi, H.E. and Storm, C., Mechanics of Biopolymer Materials: Single Chains and Bulk Properties, *Multiscale Materials Modeling Conference Proceedings MMM2010*, **637-646** (2010).
2. Amuasi, H.E. and Storm, C., Off-Lattice Monte Carlo Simulation of Supramolecular Polymer Architectures, *Physical Review Letters*, **105**, 248105 (2010).
3. Amuasi, H.E. and Storm, C., Dealing with Fixed-Length Constraints in Monte Carlo Simulations of Polymer Networks, (*soon to be submitted*).
4. Amuasi, H.E., Storm, C. and Frenkel, D., Effective Mechanics of Collagen Fibrils, (*soon to be submitted*).

Animation

Amuasi, H.E., Storm, C., Ngo, N. and Pieterse, K., *Collagen: The fabric of life*, ICMS Animation Studio, published online: <http://www.youtube.com/watch?v=uXdOSUnCKtk>, QR Code:



CURRICULUM VITAE

Henry Emmanuel Amuasi was born on April 15, 1976 in Sekondi, Ghana. His pre-university education was undertaken in Ghana at the Presbyterian Boys' Senior Secondary School, Legon, Accra where he graduated in 1993.

He went on to study physics at the Kwame Nkrumah University of Science and Technology, where he graduated in 1999 with first class honors with a dissertation on shortest-path methods in networks under the supervision of Prof. P. Agyei. He then began working as a computer software developer at Beltway Systems for the next three years.

In 2003 he attended The African Institute for Mathematical Sciences, Cape Town, South Africa to study mathematics and physics and graduated with first class honours with a diploma. His dissertation was on the mathematics of holography.

He went on to undertake a master's degree in physics at Stellenbosch University, South Africa under the supervision of Prof. Kristian Müller-Nedebock where he obtained his master's degree (cum laude) with a thesis entitled 'Fluctuations In A Melt Of Flexible Polymers With Bond-Directed Dipolar Monomers'.

In February 2008 he began PhD research in theoretical biophysics, within the Theory of Polymers and Soft Matter Group, and under the daily supervision of Dr. Cornelis Storm in the Applied Physics Department, Eindhoven University of Technology, Eindhoven, The Netherlands. The most important results of his research during this time have been included in this thesis.

Also during this time of research Henry spent three months, from March to June 2011, at the University of Cambridge, collaborating with Professor Daan Frenkel, head of the Theoretical and Computational Chemistry Group, Department of Chemistry.

Henry has also attended, presented posters, and given talks at various national and international conferences including Physics@FOM-Veldhoven Conference, Veldhoven, The Netherlands, January 2011, Cambridge-Edinburgh Meeting 2011, Department of Chemistry, University of Cambridge, Cambridge, UK, April 2011, and 'Soft Matter Far From Equilibrium' Gordon Research Conference, New Hampshire, USA, August 2011 (Poster).

ACKNOWLEDGMENTS

No good work is crafted in complete isolation from others. This adage is no less true of my work. Indeed, I am indebted to many persons who have contributed directly and indirectly to the success of this thesis. So I would like to take this opportunity to thank them.

I wish, first and foremost, to praise and thank the Almighty God Our Heavenly Father through Jesus Christ my Lord, with Whom lie all the treasures of wisdom and knowledge, and Who offers the fullness of His love, grace and mercy to everyone. In answer to prayer I have received His care, help and guidance throughout this time of research. May my highest praises and blessings be Yours always.

Secondly, I thank my dear wife Christine for surrounding me with her love and sharing a comfortable home that I could always return to. I cannot thank you enough for the gift that you are to me. I'm also deeply appreciative of my dear brothers and sisters of the Trinity Church Eindhoven, especially Pastors Francis and Barbara Noordanus, for their wisdom, fellowship and prayers during this time of research.

I thank my parents Prof. Dr. John Humphrey Amuasi and Mrs. Joyce Adwoa Amuasi, and my siblings, John (and his wife Ama), Ebenezer, Grace, and Mercy for their unwavering faith, prayers, love and support throughout my life. I'll always cherish what you have so kindly given me to make me what I am today. I thank no less my wife's parents – drs. Ton and Teuny Veen – and her family, whose friendship and generosity have been a warm encouragement to me. I include my good friend, Yaw Boakye Lawrence, for his unwavering support and moral advice.

My supervisor, Dr. Cornelis Storm (Eindhoven University of Technology), has been extremely helpful in offering his academic experience, guidance and encouragement throughout this research in many different ways. Collaboration with him has proven invaluable in producing some of the most important mathematical results of this thesis, particularly the TRACTRIX method in Chapter 4. I also thank him for his tremendous help during the writing up of this thesis.

I am very grateful to project leader and experimental physicist prof. dr. Gijsje Koenderink (Universiteit Amsterdam/FOM Institute AMOLF,

The Netherlands) for a critical reading of this thesis and whose insight and experience with reconstituted collagen tissue mechanics and self-assembly has been most instrumental in the development of the mechanical and modeling of the collagen fibril described in Chapter 6.

I am also thankful to project member and colleague Martin De Wild (FOM Institute AMOLF, The Netherlands) for introducing me to the laboratory tools and techniques (such as Atomic Force Microscopy and Electron Beam Microscopy) which he uses to study collagen self-assembly. Such an education was important in shaping the ideas that led to the computational modeling of the collagen fibril.

The advice of theoretical and computational physicist prof. dr. Gerard Barkema (Universiteit Leiden/Universiteit Utrecht, The Netherlands) enabled me to establish a deep understanding of Markov Chain Monte Carlo methods and its implementation by C++ programming. This inspired and helped pave the way towards the invention of a novel Monte Carlo method TRACTRIX described in Chapter 4. I thank him too for a critical reading of this manuscript.

A special thanks goes to prof. dr. Daan Frenkel (University of Cambridge, UK) who kindly invited me for a three-month collaboration with his group at the University of Cambridge, and who gave crucial theoretical and computational physics advice for the modeling and simulation of the collagen fibril which can be found in Chapter 6.

I also thank my promoter and head of the Theory of Polymers and Soft Matter Group (TPS), prof. dr. M. A. J. Michels, for a critical reading of this thesis manuscript as well as his personal advice and guidance regarding my future scientific career. Being part of your team has helped obtain the scientific training as well as spark within me a deep interest in theoretical physics research which I deem to be important for the continuance of my scientific career.

A special thanks goes to senior colleague prof. dr. ir. Paul van der Schoot, for a critical reading of this thesis manuscript. I have had the privilege of attending his insightful lectures in soft matter physics, which were instrumental in establishing my interest in the subject. Moreover, I deeply appreciate your friendly and generous reception of everyone, including myself, for any kind of discussion.

I thank the members of the Institute for Complex Molecular Systems (ICMS) Animation Studio, Koen Pieterse and Nie Ngo, for creating a beautiful animation that has served to succinctly illustrate the hierarchical structure of collagen. Some of the stills of this animation were used in the design of the cover of the thesis booklet.

Many thanks go to TPS secretary, W.A.M. (Helmi) van Lieshout, for taking care of numerous administrative issues related to my research and travel expenses. Thank you, Helmi, for being so patient and helpful. You are much appreciated for going out of your way to make our office a lively one.

Finally, I wish to thank all my other colleagues of the TPS: Adrian and Dmytro (both of whom I once shared an office with), Elizaveta, Hamed,

Wouter, Francisco, Ewa, Andrea, Peter, Sanders, Ronald, Saber, Jeroen, Murat, Abhinav, Leon, Alexey and Chrysostomos. Thank you for making our working environment a warm and conducive place for research. I feel very privileged to have worked with all of you.

